

**MinEx CRC Limited**

26 Dick Perry Avenue, Kensington, WA, 6151  
PO Box 1130, Bentley, WA, 6102, Australia  
admin@minexcrc.com.au



**MinEx CRC provides financial support to the value of \$1K to promote Honours and Masters by Coursework projects that are aligned with the mission of MinEx CRC and to encourage young researchers toward a career in mineral exploration research. Projects are not restricted to MinEx CRC Participants and Affiliates.**

**Please note that the content of this thesis has not been subjected to peer-review and subsequent corrections.**



Australian Government  
Department of Industry,  
Science and Resources

**Cooperative Research  
Centres Program**

# Constraining the hidden Delamerian margin: A geochemical and geochronological analysis of an arc undercover

Thesis submitted in accordance with the requirements of the University of  
Adelaide for an Honours Degree in Geology

Matthew Robert Barnett

November 2024



THE UNIVERSITY  
*of* ADELAIDE

## **TITLE**

Constraining the hidden Delamerian margin: A geochemical and geochronological analysis of an arc undercover.

## **RUNNING TITLE**

Constraining the hidden Delamerian margin

## **ABSTRACT**

The Cambro-Ordovician Delamerian Orogen of southeastern Australia preserves the final stages of Gondwana amalgamation and the initiation of a west-dipping subduction system that formed the palaeo-Pacific Ocean. The Loch Lilly-Kars Belt (LLKB), located south of Broken Hill, is the central portion of the Delamerian Orogen, though is buried under Cenozoic cover of the Murray Darling Basin. As a result of this, the rocks of the LLKB are understudied and poorly constrained despite potential for mineral endowment.

To better understand the formation and evolution of the LLKB, samples were collected from six diamond drill holes drilled in 2023 by Geoscience Australia and MinExCRC, as part of the National Drilling Initiative. Geochronological constraints on low-grade metamorphism, alteration, and magmatism were obtained using in-situ LA-ICP-MS Rb–Sr and U–Pb age mapping of altered igneous suites and cross-cutting calcite veins. A depositional window of sedimentary samples within the section was also deduced using Rb–Sr and U–Pb spot analyses of deep-water shales and carbonate beds, respectively. Geochemical analysis of igneous samples was undertaken in the form of solution ICP-MS, obtaining major and trace element data along with TIMS analysis of Sm–Nd isotopes to further understand the tectonic setting of the Delamerian and the geochemical nature of the intrusive samples within these sections.

Results show that the LLKB was an active margin of the Delamerian Orogen and contains age and geochemical equivalent intrusions to those in the Stavely Arc and Koonenberry Belt in adjacent sections of the arc. Furthermore, our study also records evidence for a second episode of igneous activity *ca.* 500–470 Ma of back-arc affinity with an eastward migration. Data indicates episodic hydrothermal activity in the region continued until at least 250 Ma after the conclusion of the Delamerian Orogeny, likely associated with tectonic fluctuations at the subduction margin. This periodic tectonism may be linked to the wider evolution of the collisional margin as the subduction zone rolled back eastwards.

## **KEYWORDS**

Delamerian Orogen; subduction; geochemistry; elemental mapping; alteration; volcanic arc; Tasmanides; greenfields; orogeny.

## TABLE OF CONTENTS

Title.....	i
Running title .....	i
Abstract.....	i
Keywords.....	i
List of Figures and Tables .....	5
Introduction .....	8
Geological Background .....	11
The Tasmanides.....	11
The Delamerian Orogen .....	11
The Loch Lilly-Kars Belt .....	13
Delamerian mineralisation and its link to subduction .....	14
Methods .....	15
Sample collection and preparation .....	15
Petrography.....	16
Scanning Electron Microscopy.....	17
Solution ICP-MS .....	17
Thermal Ionisation Mass Spectrometry (TIMS) .....	17
LA-ICP-MS .....	18
In-situ Rubidium–Strontium and trace element analysis .....	18
Laser spot analysis.....	18
Raster mapping analysis .....	19
In-situ Uranium–Lead and trace element carbonate mapping analysis.....	21
Observations and Results.....	23
General sample overview .....	23
Sedimentary Rocks .....	23
Igneous Samples .....	24
Petrography.....	25
SEM .....	28
MLA/BSE Maps .....	28
Sample LK12-173.....	28
Sample MP02-556 .....	29
Sample MP03-548 .....	30
Geochemistry.....	31



Solution ICP-MS .....	31
LK12 olivine basalt dykes .....	32
MP2 and MP3 granites/granodiorites .....	33
Sm–Nd Tims analysis of Igneous samples.....	35
Geochronology .....	37
Rb–Sr ages of spot analysed shales and intrusions.....	37
LA-ICP-MS Rb–Sr ages of raster analysed alteration textures.....	40
Sample MP03-493 .....	40
Sample LK-172.....	43
Sample MP02-583 .....	45
LA-ICP-MS U–Pb ages of raster analysed carbonate beds and veins .....	48
Discussion.....	48
The rift, drift and end of a passive margin on the Tasman Line.....	48
Back-arc sedimentation in the LLKB .....	49
An arc in the Loch Lilly-Kars Belt.....	51
From arc to back-arc.....	55
The mafic olivine basalt dykes of LLKB .....	57
Post active margin events in the Loch Lilly-Kars Belt.....	59
Conclusions .....	61
Acknowledgments .....	62
References .....	63
Appendix 1: Table of samples and equivalent hole and depth .....	69
Appendix 2: Sample photos and description .....	70
Appendix 3: Detailed thin section descriptions of igneous samples from LLKB .....	81
Appendix 3A: LK12A .....	81
Appendix 3B: LK12B.....	81
Appendix 3C: MP2A .....	82
Appendix 3D: MP2B .....	83
Appendix 3E: MP3A .....	84
Appendix 3F:MP3B.....	85
Appendix 4: Elemental dwell times for LA-ICP-MS Rb–Sr spot and elemental mapping analysis .....	86
Appendix 5: Elemental dwell times for LA-ICP-MS U–Pb elemental mapping analysis .....	87
Appendix 6: Elemental composition maps from Iolite4 for sample MP03-493.....	88
Appendix 7: Elemental composition maps from Iolite4 for sample LK-172.....	89

Appendix 8: Elemental composition maps from Iolite4 for sample MP02-583.....	90
Appendix 9: Sample MP02556.....	91
Appendix 10: Sample LK12-173.....	94
Appendix 11: MP03-546 .....	97
Appendix 12: Sample MP02-579 .....	100
Appendix 13: Parameters for data acquisition of Rb–Sr shale & illite LA-ICP-MS spot analysis. ....	103
Appendix 14: Solution ICP-MS geochemical data.....	104
Appendix 15: Raw Data from Rb–Sr LA-ICP-MS spot analysis of shales and intrusions .....	106
Appendix 16: Solution ICP-MS method .....	122
Appendix 17: Method for whole-rock digestion used in TIMS preparation .....	122

## LIST OF FIGURES AND TABLES

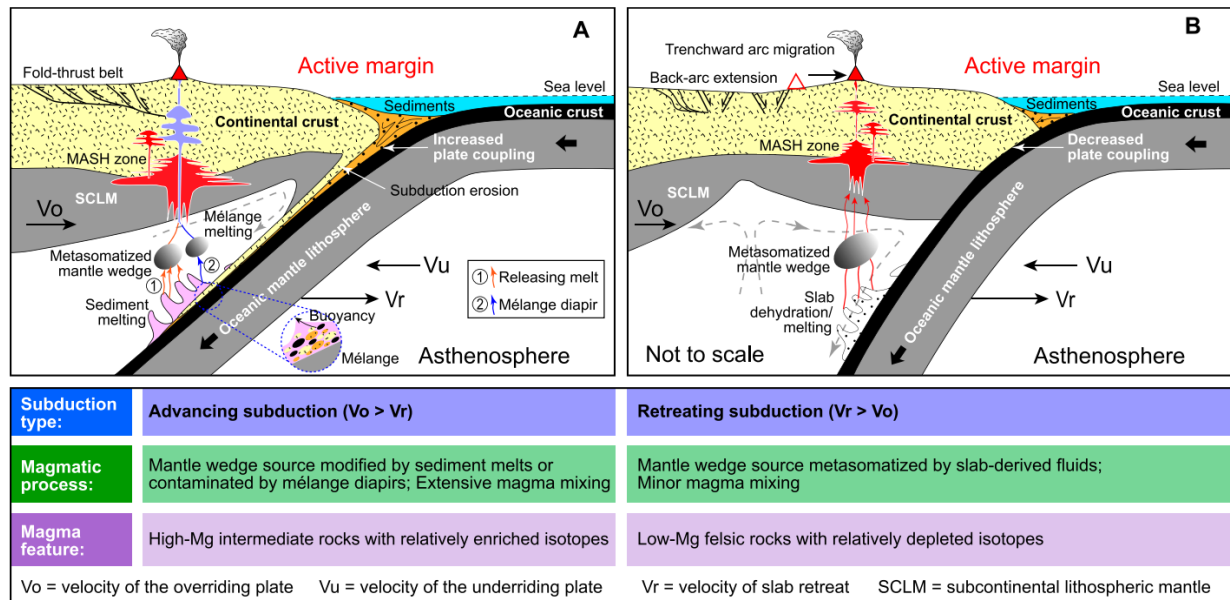
Figure 1: Schematic diagram showing subduction zone types and corresponding structure and deformation records in the upper plate (modified after Cawood et al., 2009; Straub et al., 2020; Chapman et al., 2021). After An et al., (2024). MASH—melting, assimilation, storage, homogenization. ....	9
Figure 2: Location map of the Terra Australis Orogen and it's position relative to Australia's position within the Gondwanan continent in the Cambrian Period. Cratonic Australia, Antarctica, Africa and India are labelled. The hypothesised location of the Stavely Arc and Loch Lilly-Kars Belt (LLKB) are labelled. After Johnson et al. (2016). ....	12
Figure 3: Total magnetic intensity map of south-eastern Australia obtained through SARIG and The Geological Survey of New South Wales. The Delamerian Orogen is highlighted as the grey region (LEFT) however it is known as the Tyennan Orogen (Cayley, 2011; Gray et al., 2024) in Tasmania. The drilling region is highlighted in the red box. The Loch Lilly-Kars Belt, Tarrara-Menindee Trough and Lake Wintlow Belt regions are noted. Drill hole locations and ID's plotted are based on GPS co-ordinates from Geoscience Australia. Known mineral prospects, their type and location have been taken from Hong et al. 2024 .....	14
Figure 4: Thin section photos taken of igneous samples from LLKB captured in both PPL and XPL (labelled top left corner). Main minerals labelled in white boxes. Abbreviations: Oli = Olivine; Qtz = quartz; Plag = plagioclase; Carb = carbonate; Ox = pyrite; Musc = muscovite; Chl = chlorite; Epi = epidote; Vug = hole; Hbl = hornblende; Ti = Titanite; Zr = Zircon. Colour of sample name correlates to equivalent geochemical analysis sample. ....	27
Figure 5: Back scatter electron map (middle), mineral liberation analyser (MLA) map (right) and mineral legend (left) of thin section sample LK12-173 and geochemical equivalent LK12B. Mineral Mode percentages of MLA mapping of major minerals found in Table 6.....	28
Figure 6: Back scatter electron map (top), mineral liberation analyser (MLA) map (bottom) and mineral legend (left) of thin section sample MP02-556 and geochemical equivalent MP2A. Mineral mode percentages of MLA mapping of major minerals found in Table 6.....	29
Figure 7: Back scatter electron map (top), mineral liberation analyser (MLA) map (bottom) and mineral legend (left) of thin section sample MP03-548 and geochemical equivalent MP3B. Mineral mode percentages of MLA mapping of major minerals found in Table 6. ....	30
Figure 8: TOP- Spiderplot of trace element concentrations of igneous samples from LLKB normalised to primitive mantle values (Sun & McDonough, 1995). BOTTOM- Spiderplot of REE element concentration in igneous samples from LLKB normalised to C1 chondrite values (Anders & Grevesse, 1989). Both are plotted on a log scale.....	34
Figure 9: Scatterplot showing the obtained $\epsilon\text{Nd}$ (T) values from TIMS analysis of Sm & Nd isotopes (Y-axis) against time (Ga) (X-axis) of samples obtained using TIMS Sm–Nd analysis. Red star depicts mean Kanmantoo $\epsilon\text{Nd}$ (T) from Foden et al. (2020). Depleted mantle evolution line, Chondritic Uniform reservoir (CHUR) line and Australian shale $\epsilon\text{Nd}$ (T) evolution values from Rollinson & Pease (2021) plotted. After Rollinson & Pease (2021).....	36

Figure 10: Isochrons from analysed intrusion samples with ages and initial $^{87}\text{Sr}/^{86}\text{Sr}$ values along with associated propagated $2\sigma$ errors and mean square weighted deviation (MSWD). Sample name equates to drill hole and depth in hole. Age uncertainty is quoted as total age uncertainty. ....	38
Figure 11: Isochrons from analysed shale samples with ages, initial $^{87}\text{Sr}/^{86}\text{Sr}$ values along with associated errors and mean square weighted deviation (MSWD). The uncoloured circles indicate removed analysis points. Sample name equates to drill hole and depth in hole. Age uncertainty is quoted as total age uncertainty. ....	39
Figure 12: A) Sample MP03-493 mounted in epoxy with the red box depicting the mapped region; B) The three distinct pixel maps for phases (Li-rich, Rb-rich & Carb rich) present in sample MP03-493 (red regions) overlain on $^{39}\text{K}$ concentration map (left) and $^{39}\text{K}$ scale (right); C) The three distinct phases in B compiled into one ternary diagram showing their respective spatial relationships to each other. ....	40
Figure 13: (TOP) Isochrons for phase MP03-493-Li (Left) and MP03-493-Rb (Right) with ages and $^{87}\text{Sr}/^{86}\text{Sr}_{(i)}$ along with associated $2\sigma$ errors and mean square weighted deviation (MSWD). (BOTTOM) ternary map of the pixel regions which each isochron was analysed from. Each isoplot is colour coded to its colour in the ternary map.....	42
Figure 14: A) Sample LK-172 mounted in epoxy with the red box depicting the mapped region; B) Two distinct pixel maps for phases (Si-rich & Rb-rich) present in sample LK-172 (red regions) overlain on $^{29}\text{Si}$ concentration map (left) and $^{29}\text{Si}$ scale (right); C) The two distinct phases in B compiled into one ternary diagram showing their respective spatial relationships to each other. ....	43
Figure 15: (LEFT) Isochrons for phase LK-172-Rb (top) and LK-172-Si (bottom) with ages and initial $^{87}\text{Sr}/^{86}\text{Sr}$ along with associated $2\sigma$ errors and mean square weighted deviation (MSWD). (RIGHT) ternary map of their pixel regions that each isochron was analysed from. Each isoplot is colour coded to its colour in the ternary map.....	44
Figure 16: A) Sample MP02-583 mounted in epoxy with the red box depicting the mapped region; B) Three distinct pixel maps for phases (Fe-Mg rich veins, Na-rich phase and K-Al Rich phase) present in sample MP02-583 (red regions) overlain on $^{56}\text{Fe}$ concentration map (left) and $^{56}\text{Fe}$ scale (right); C) The three distinct phases in B compiled into one ternary diagram showing their respective spatial relationships to each other. ....	45
Figure 17: Isochrons for phase MP02-583-Fe (top left), MP02-583-Na (top right) and MP02-583-K (bottom right) with ages and initial $^{87}\text{Sr}/^{86}\text{Sr}$ along with associated $2\sigma$ errors ( $2\sigma$ quoted) and mean square weighted deviation (MSWD) and (bottom left) ternary map of their pixel regions which each isochron was analysed from. Each isoplot is colour coded to its colour in the ternary map. ....	46
Figure 18: An overview of the evolution of the LLKB region from; (A) the initiation of rifting in Rodinia and (B) subsequent drift from Laurentia to form Gondwana to (C) the deposition of sediments associated with the passive margin prior to subduction initiation (Pualco Tillite and Braemer Ironstone Formation) on the margin. Left image is overhead view and right is a cartoon cross-section from W through E along purple line. The green star represents the westernmost point of the LLKB. ....	49
Figure 19: A cartoon cross-section of back-arc sedimentation of the Torrawangee and Dinggali Formations in the back-arc behind the Lake Wintlow Belt during extension in the LLKB. The red linear shapes in the left image depict the initial Lake Wintlow belt location and its evolution from 505 Ma to 470 Ma. The left image is an overhead view	

and right is a cartoon cross-section from W through E along the purple line. The green star represents the westernmost point of the LLKB. ....	51
Figure 20: An overview of the LLKB region during the formation of the Lake Wintlow Belt arc and its placement on top of the Torrawangee and Dinggali Formations after subduction of the proto-Pacific Ocean initiated along the Gondwanan eastern margin. The left image is an overhead view and the right is a cartoon cross-section from W through E along purple line. The green star represents the westernmost point of the LLKB.....	53
Figure 21: LEFT- Scatterplot of $\epsilon\text{Nd}_{(T)}$ vs $^{147}\text{Sm}/^{144}\text{Nd}$ of igneous samples analysed in this project (red circles) along with S-type granites, Cambrian mafic volcanics and Kanmantoo sedimentary rocks from The Delamerian Orogen (Foden et al., 2020) along with evolution lines of these samples based on specific assimilation fractional crystallisation (AFC) values. RIGHT- Spiderplot depicting the change in concentration of trace elements in igneous samples found in the AFB (Foden et al., 2020) compared to N-MORB values depending on the percentage of assimilated Kanmantoo sedimentary rocks in the melt and their equivalent $\epsilon\text{Nd}$ (t) values. After Foden et al. (2020). ....	54
Figure 22: Linework of solid geology map of Loch Lilly-Kars and Lake Wintlow Belts, New South Wales. The drillholes used in this project are highlighted as pink dots. Background is a coloured semi-transparent Bouger gravity anomaly grid (Lane et al., 2019) above greyscale 0.5 vertical derivative of aeromagnetic data reduced to the pole (Poudjom Djomani et al., 2019). Blue line is seismic line 96AGS_BH1B from Korsch et al. (2006). After (Clark et al., 2024).....	57
Figure 23: Time space plot showing the Rb–Sr ages and associated errors of analysed samples in this project sorted by their drill-hole location. Holes are plotted from most northwest (left) to most southeast (right). The estimated timing of orogenic events during Tasmanide formation have been taken from Foden et al. 2020 and plotted as coloured bars.....	59

## INTRODUCTION

Orogenesis is the process of mountain building, often occurring in compressional tectonic regimes (Sengör, 2000; Johnson & Harley, 2012). One compressional tectonic process leading to orogen formation is subduction, the process by which negatively buoyant oceanic crust sinks into the mantle at an active plate margin. The compression focused at the subduction trench is controlled by the degree of plate coupling experienced by the upper plate to the lower plate (Lister et al., 2009). This force is larger with increased buoyancy of the subducting oceanic lithosphere, influenced by its varying morphology such as ribbon microcontinents getting wedged in the trench, or a decrease in the slab-pull force as the slab breaks on descent (An et al., 2024). Due to these fluctuations, the system exhibits periods of extension when plate coupling is low and compression when high (An et al., 2024). It is when plate coupling is high that orogenesis occurs. This process, known as subduction orogenesis, leaves a characteristic signature on the upper plate of a curvilinear ‘belt’ of igneous rocks of intermediate chemistry, with thrust and fold belts of back-arc sediments behind it (An et al., 2024) observable from geophysical datasets like magnetic intensity or density.



**Figure 1: Schematic diagram showing subduction zone types and corresponding structure and deformation records in the upper plate (modified after Cawood et al., 2009; Straub et al., 2020; Chapman et al., 2021). After An et al., (2024). MASH—melting, assimilation, storage, homogenization.**

This geophysical anomaly is caused by the subduction process, where the volatile-rich slab releases fluids into the mantle wedge approximately 100 km from the trench. The addition of volatiles here decreases the melting temperature of the mantle above the slab, leading to adiabatic melting of the mantle wedge and the formation of volcanos and igneous suites parallel to the subduction trench on the upper plate (Figure 1). This phenomenon is seen in present day regions such as the Andes. These ‘belts’ are important to society for their mineral potential. The process of volatile input, caused by subduction, into the mantle below these volcanoes and subsequent crustal assimilation (Huston et al., 2015) is crucial to the formation of porphyry mineral systems (Sillitoe, 2010) exploited for copper and zinc.

This paper focuses on the Delamerian Orogeny, located east of the Gawler Craton in central Australia. It formed as the paleo-Pacific Ocean subducted beneath Gondwana in the final stages of its assembly from 515–490 Ma (Moresi et al., 2014; Foden et al.,

2006; 2020). The volcanic arc associated with this orogen is hypothesised to consist of the Stavely Arc, located in western Victoria and the Koonenberry Belt in New South Wales, which contain several porphyry systems (Huston et al., 2015; Hong et al., 2023), indicating the relevance of this paper to mineral exploration. However, due to burial under Murray-Darling Basin sedimentary cover, the ‘link’ between these two regions has not historically received the same exploration focus. Recent analysis has deduced that the belt of igneous rocks linking these regions continues undercover through the Loch-Lilly Kars Belt (LLKB) (Hong et al., 2023) in southwestern NSW, indicating significant regional greenfields mineral potential.

Using core samples drilled by Geoscience Australia (GA) as part of the MinEx Cooperative Research Centre’s (MinExCRC) National Drilling Initiative (NDI) (Mole et al., 2024) in the LLKB, this study aims to deduce the composition, age, and tectonic evolution of this early Cambrian subduction margin by; analysing the geochemistry of igneous suites, constraining the age of sedimentation and igneous suite emplacement events. Methods utilised involve in-situ  $^{87}\text{Rb}/^{86}\text{Sr}$  and trace element Laser Ablation Inductively Coupled Mass Spectrometry (LA-ICP-MS) analysis of shales and intrusives, along with the dating of hydrothermal activity and carbonate formation with U–Pb LA-ICP-MS carbonate dating. The geochemical and geochronological findings in this study may imply a genetic link to the Stavely Arc and Koonenberry Belt to the south and north respectively.



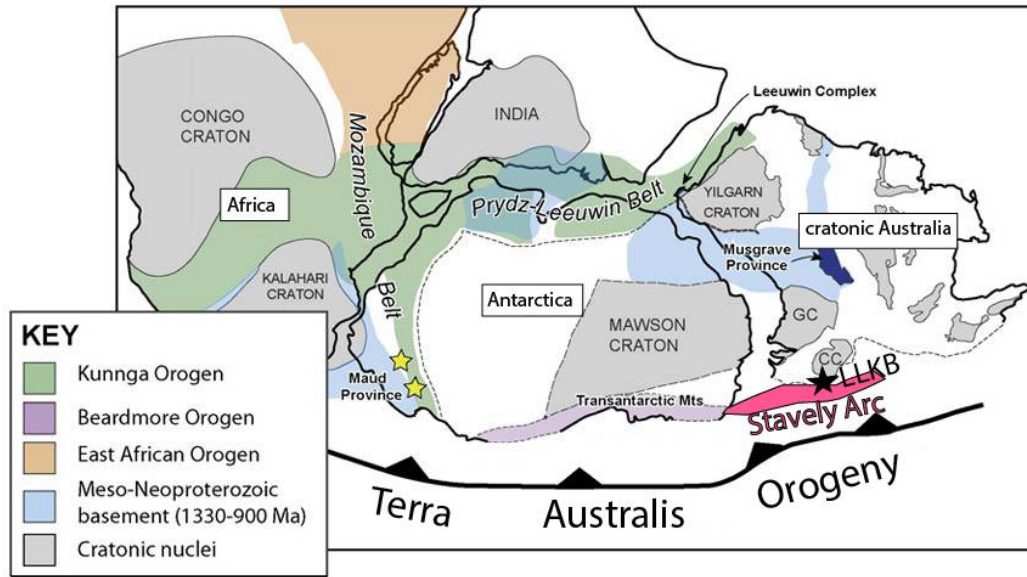
## **GEOLOGICAL BACKGROUND**

### **The Tasmanides**

The Tasmanides are a series of accretionary orogenic systems that form the eastern third of Australia, east of the Tasman Line (Foster & Gray, 2000), resulting from the initiation of west-dipping subduction of the palaeo-Pacific Ocean beneath the eastern margin of Gondwana. They formed *ca.* 515–230 Ma (Foden et al., 2020; Glen & Cooper, 2021; Greenfield et al., 2011; Gray & Foster, 2004) and are characterized by repetitive cycles of long periods of extension as the subduction zone rolled back and short pulses of compression as previously rifted microcontinents collided with the subduction trench. These compressional phases include the Delamerian (*ca.* 515–490 Ma), Benambran (*ca.* 460–425 Ma), Tabberabberan (*ca.* 390–380 Ma), Kanimblan (*ca.* 360–340 Ma) and Hunter Bowen (*ca.* 260–230 Ma) orogenies (Glen & Cooper, 2021; Foden et al., 2020; Shaanan et al., 2018).

### **The Delamerian Orogen**

The Delamerian Orogen formed during the final stages of Gondwanan assembly in the Cambrian (*ca.* 515–490 Ma) (Foden et al., 2020; 2006) and is interpreted to be the first orogenic cycle of the Tasmanide sequence. It makes up a small part of the system called the ‘Terra Australis Orogen’ (Cawood, 2005; Paulsen et al., 2023) (Figure 2) that ran along the southern Gondwanan margin from South Africa through Antarctica and Australia (Foden et al., 2020; Paulsen et al., 2023).



**Figure 2: Location map of the Terra Australis Orogen and its position relative to Australia's position within the Gondwanan continent in the Cambrian Period. Cratonic Australia, Antarctica, Africa and India are labelled. The hypothesised location of the Stavelly Arc and Loch Lilly-Kars Belt (LLKB) are labelled. After Johnson et al. (2016).**

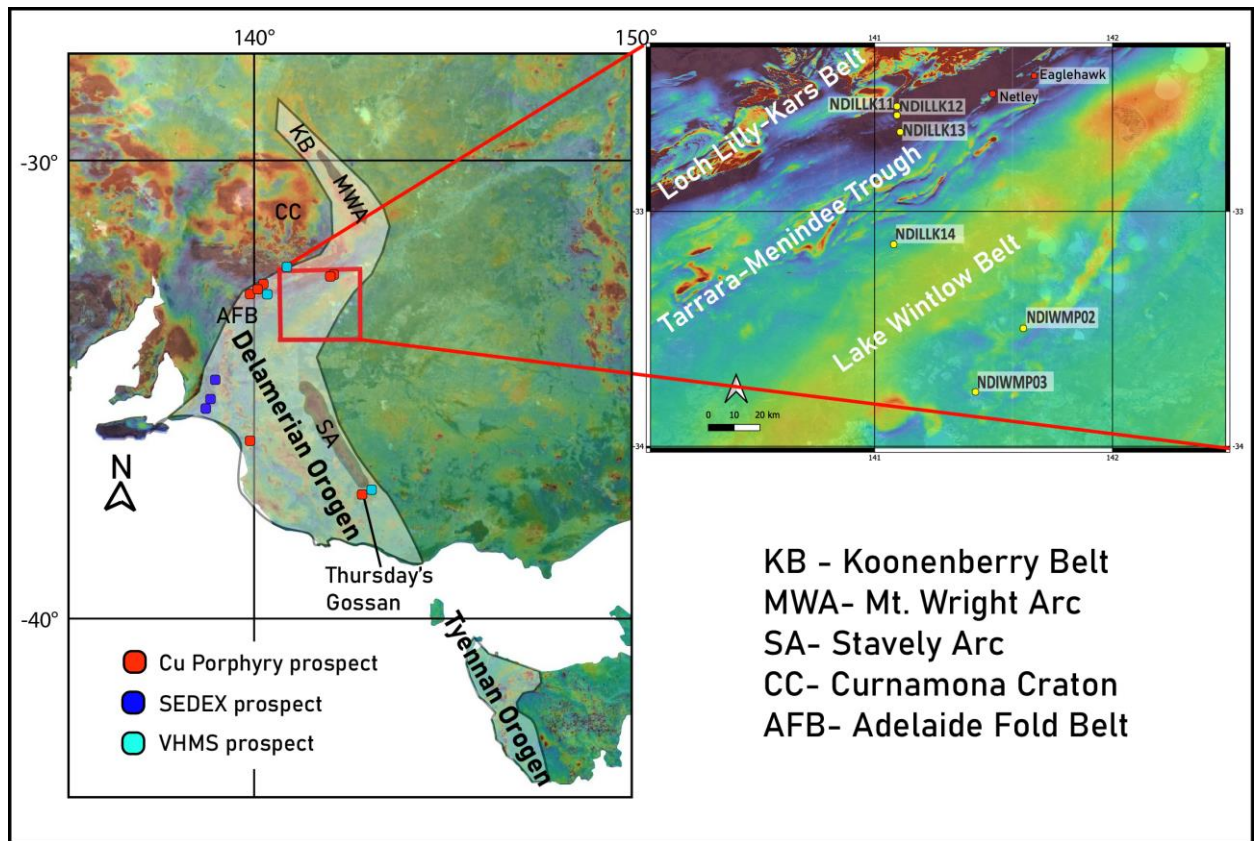
The orogen has been extensively studied due to its structural complexity and mineral endowment (Huston et al., 2015). Mineral deposits have been preserved due to the orogen's short-lived nature, as the collision of microcontinental blocks with the subduction zone caused the system to jump outboard to the Macquarie Arc in the Ordovician (Crawford et al., 2007), preserving the arc a further distance from the active plate margin. The orogen spans from Tasmania (where it is known as the Tyennan Orogen) (Cayley, 2011; Gray et al., 2024) north to western New South Wales (NSW) and consists of discontinuous 'belts' of high magnetic intensity interpreted as arc slices. These have been faulted, likely resulting from a series of collisions during Tasmanide formation (Abdullah & Rosenbaum, 2018; Bailey et al., 2018), including that of VanDieland, a rifted microcontinent that was discarded from the western edge of Laurentia as the proto-Pacific Ocean opened. This collision with the continental margin

of Gondwana is believed to have terminated the Delamerian Orogeny (Huston et al., 2015; Gray et al., 2024). Previous research has indicated that the Delamerian Orogen contained a continuous volcanic arc, presently sitting in the Stavely region of Victoria and the Koonenberry Belt region of NSW (Foden et al., 2020). This hypothesis is supported by the presence of igneous rocks with ages ranging from *ca.* 515 Ma to 500 Ma (Foden et al., 2020; Bailey et al., 2018; Johnson et al., 2016) of andesitic and dacitic composition in both the Stavely and Koonenberry regions. They are interpreted as subduction derived, due to their light rare earth element (LREE) enrichment and negative Eu anomalies (Lewis et al., 2015) and hosted within back-arc sediments derived from central Gondwana (Crawford et al., 2007), namely the Normanville and Kanmantoo groups in the Adelaide Fold Belt (AFB), the Nargoon and Glenthomson groups in the Stavely Zone and Ponto and Teltawongee groups in the Koonenberry Belt. However, proving its existence between the two, through the Loch Lilly-Kars Belt (LLKB), has proved difficult due to its burial under younger sedimentary cover.

### **The Loch Lilly-Kars Belt**

The LLKB covers an area of 40 km by 200 km, trending NE–SW adjacent the Curnamona Craton (Figure 3). The belt itself has no surface expression, covered by the Cenozoic sediments of the Murray-Darling Basin (Baatar et al., 2020). Until NDI drilling in 2023 by GA, all geological interpretation came from eight drill holes into the basement and airborne geophysical data (Baatar et al., 2020). These drillholes intersected undated tholeiitic metabasalts and dolerites (Baatar et al., 2020) formed on a rifting margin associated with the breakup of Rodinia, equivalent to the Mount Arrowsmith Volcanics in the Koonenberry Belt (Crawford et al., 1997), and intermediate and felsic igneous rocks dated in two pulses; (*ca.* 496 Ma) Cambrian and

(ca. 393 Ma) Devonian (Baatar et al., 2020). These later intrusions sit within the Lake Wintlow Belt (Figure 3). This belt is separated from the LLKB by the Tarrara-Menindee Trough (Clark et al., 2024) and the ages closely correlate with intermediate intrusions found in the Stavely Arc and Koonenberry Belt. The tectonic setting for these intrusions has not been a focus of previous research and this paper uses new samples to further understand the tectonic evolution of the LLKB during Tasmanide formation.



**Figure 3:** Total magnetic intensity map of south-eastern Australia obtained through SARIG and The Geological Survey of New South Wales. The Delamerian Orogen is highlighted as the grey region (LEFT) however it is known as the Tyennan Orogen (Cayley, 2011; Gray et al., 2024) in Tasmania. The drilling region is highlighted in the red box. The Loch Lilly-Kars Belt, Tarrara-Menindee Trough and Lake Wintlow Belt regions are noted. Drill hole locations and ID's plotted are based on GPS co-ordinates from Geoscience Australia. Known mineral prospects, their type and location have been taken from Hong et al. 2024

### Delamerian mineralisation and its link to subduction

The porphyry mineral systems found in the orogens of the Tasmanides, specifically in the Mt Stavely Volcanic zone and Macquarie Arc, are intrinsically linked to subduction.

Thursday's Gossan, a recently discovered Cu-porphyry deposit in Victoria adds to the growing number of deposits found within Delamerian sequences (Hong et al., 2024), showing the potential for further discoveries (Figure 3). Huston et al. (2015) suggested that the switching from 'advancing-type' to 'retreating-type' subduction is paramount in ore deposit formation. The compressional state of advancing subduction induces the constriction of magma pathways, trapping arc magmas at depth, facilitating continued fractionation and evolution towards higher metal concentrations (Chen et al., 2023). Subsequently, the switch to retreating subduction and coeval extension re-opens these pathways, allowing the buoyant metal-endowed magmas to infiltrate the upper crust and form porphyries (Huston et al., 2015). This hypothesis is supported by alteration textures associated with Tasmanide porphyry mineralisation commonly being dated to shortly after the end of an orogenic event (Hong et al. 2024).

## **METHODS**

### **Sample collection and preparation**

The samples analysed in this project were obtained during the NDI by MinExCRC. Specifically, from 'NDI Campaign 5: Delamerian Margins NSW NDI' from March to June 2023. The following holes were targeted for this study: NDILLK11, NDILLK12, NDILLK13, NDILLK14, NDIWMP02 and NDIWMP03 (GPS coordinates provided in Appendix 1). 22 samples were obtained for this project (Appendix 2). The targeted lithologies were shales, carbonates, granodiorites and cross-cutting dykes. The intention being to understand the age of deposition and volcanism, the nature of igneous rocks and their subsequent alteration.

## Petrography

Six samples were selected for thin section analysis based on structural relationships and mineralogy present in core samples. Samples were cut using the small diamond saw and sent to Thin Section Australia for mounting.

Detailed descriptions and photos of mineralogy were done using a Leica Petrographic Microscope (DS2700P) with a mounted camera and LASx software. Photos were taken in both PPL and XPL. Table 1 gives sample names and reason for analysis.

**Table 1: Sample name and geochemical equivalent and reasons for thin section analysis.**

<b>Sample Name</b>	<b>Geochemical equivalent</b>	<b>Reason for selection</b>
<b>LK12-172</b>	<b>LK12A</b>	Selected to determine the mineralogy of a very-fine grained dyke within drill-hole NDILLK12. This sample is taken away from any contacts with the host shale.
<b>LK12-173</b>	<b>LK12B</b>	Selected to analyse the alteration textures of the dyke in <b>LLK12-172</b> . It includes the preserved shale-dyke contact.
<b>MP02-556</b>	<b>MP2A</b>	Selected to determine the alteration type that dominates this sample, its associated textures and the mineralogy of breccia infill within the sample.
<b>MP02-628</b>	<b>MP2B</b>	Selected due to its fresh appearance. The only fresh sample from this hole with the rest of the samples looking similar to <b>MP02-556</b> .
<b>MP03-493</b>	<b>MP3A</b>	The freshest igneous sample in this project, it also contains quite a coarse assemblage of minerals, suggesting crystal texture and zonation textures of plagioclase should be evident.
<b>MP03-548</b>	<b>MP3B</b>	Comparison to see the mineralogical differences between an unaltered igneous sample ( <b>MP03-493</b> ) and this sample which has been altered by later hydrothermal fluids.

### **Scanning Electron Microscopy**

Three samples (LLK12-173, MP02-556 & MP03-548) prepared for thin section petrography were imaged using Hitachi SU3800 Scanning Electron Microscope (SEM), and automated mineralogy Mineral Liberation Analyses (MLA) after being carbon-coated. Backscatter electron maps were collected, assisting with petrography and understanding different mineral phases. LLK12-173, a shale-dyke contact, was targeted for its complexity, MP02-556, an alteration breccia, to deduce alteration type, and MP03-548, a fresh igneous sample, for modal mineral percentages.

### **Solution ICP-MS**

Six igneous samples were selected for whole-rock geochemical analysis. Sample pulps underwent whole-rock digestion using the Mawson Analytical Spectrometry Services (MASS) at the University of Adelaide, following the method outlined by Wade et al. (2005). A full description is available in Appendix 16.

A 1:1000 dilution was used for analysis of rare earth elements (REEs) and a 1:100000 dilution for major elements. These were analysed at Adelaide Microscopy using the solution ICP-MS Agilent 8900x QQQ-ICP-MS. Standard values for USGS G-2 and BHVO-1 (Flanagan, 1976) were within uncertainty of published values and are provided with raw data (Appendix 13).

### **Thermal Ionisation Mass Spectrometry (TIMS)**

Samples were prepared and analysed for Sm–Nd within MASS at the University of Adelaide. Samples were spiked with  $^{150}\text{Nd}/^{147}\text{Sm}$  solution and underwent whole-rock digestion (full description in Appendix 17). Sm–Nd isotopes were isolated using

column chromatography following the method outlined in Foden et al. (1995). Isotope ratios were measured using the Isotopx Phoenix Thermal Ionisation Mass Spectrometer. The international Nd standard JNdi-1 yielded  $^{143}\text{Nd}/^{144}\text{Nd}$  values of  $0.512107 \pm 0.000003$  (2 s.d.) within uncertainty of published values ( $0.512115 \pm 0.000007$ ) (Tanaka et al., 2000). Blanks showed negligible Nd and Sm.

## **LA-ICP-MS**

### **IN-SITU RUBIDIUM–STRONTIUM AND TRACE ELEMENT ANALYSIS**

#### **Laser spot analysis**

The method outlined by Subarkah et al. (2022), and Redaa et al. (2023) was followed. Samples were selected with the aim of constraining minimum depositional or intrusion ages. Shale samples with the lowest detrital input and igneous samples containing mica-rich phases were selected. Rock chips were cut using a diamond saw in the Mawson Building at the University of Adelaide, mounted in epoxy resin and polished to expose the sample. Analysis of samples was conducted at Adelaide Microscopy using LA-ICP-MS/MS with the RESolution 193nm excimer laser ablation system coupled with an Agilent 7900x ICP-MS system. The primary standards for calibration were MDC for crystal minerals and Mica-MG for shales following Glorie et al. (2024) and Subarkah et al. (2022), respectively. Secondary standards were Robins Folly muscovite and Entire Creek pegmatite (Table 3, references therein). Each sample was analysed with the parameters outlined in Appendix 13. Data were processed using LADR (Norris and Danyushevsky, 2018). Spots with unusual signals were filtered by analysing the laser signature on LADR with evidence for ablation of apatite or zircons removed for accuracy. The reasoning omitting individual points can be found in Appendix 15. A



secondary correction was applied with MDC accounting for matrix effects between analysing potassic minerals (i.e: feldspar, mica or clay) and a glass (Glorie et al., 2024). IsoplotR (Vermeesch, 2018) was used to calculate an isochron line and equivalent errors. The total age uncertainty was propagated by accounting for  $^{87}\text{Rb}$  decay constant uncertainty ( $0.000013972 \pm 4.5\text{e}^{-8}\text{Myr}^{-1}$ ) (Gorojovsky & Alard, 2020), analysed age uncertainty and reference material age uncertainty following Redaa et al. (2021).

### Raster mapping analysis

The method outlined by Subarkah et al. (2024) was followed but modified for Rb–Sr raster geochronology. Laser mapping was carried out with the parameters outlined in Table 2. Element dwell times are presented in Appendix 4. Samples exhibiting the most albitic or potassic alteration were targeted with the aim to obtain ages for both host rock and alteration textures in each chip.

**Table 2: Parameters for data acquisition of Rb–Sr alteration mapping LA-ICP-MS**

Sample ID	Date of session	Spot Size ( $\mu\text{m}$ )	# of rasters	Mapping Time (s)
LK12-172	31/05/2024	80	30	1887
LK12-173	31/05/2024	80	29	2021
MP02-493	31/05/2024	38	40	13990
MP02-556	31/05/2024	38	69	5507
MP02-579	27/06/2024	80	35	2376
MP02-583	27/06/2024	80	25	2322
MP03-546	31/05/2024	38	40	4067

Successive raster scans were programmed with no overlap between each line, ensuring a coherent region of analyses. The rasters targeted contacts between intrusion or alteration and host rock. The primary standard for calibration was MDC with secondary standards Ruby Mine muscovite and Robins Folly muscovite (Table 3, references therein). Each standard was analysed with 20 rasters of equivalent size to analysed samples (38, 80  $\mu\text{m}$ ). These were bracketed between samples. All analysed standards returned ages within error of published values (Table 3). NIST610 was used to correct instrument drift and quantify elemental concentrations and ratios. Data was processed using Iolite4 (Petrus et al., 2017; Paton et al., 2011) to create elemental concentration maps. The spatial relationship of elemental concentrations within these maps determined the separate alteration events for analysis and pixel selection was undertaken using the polygon or elemental concentration cut-offs tools, forming separate datasets for different phases within one sample. These pixel sets were pooled and subdivided into a set of Rb–Sr analytical points based on their  $^{39}\text{K}$  ratios, maximising ratio spread and producing an optimised isochron. Each analytical point was comprised of a minimum of 30 pixels. The secondary correction was applied with Excel using MDC to account for matrix effects between analysing potassic minerals and glass following Glorie et al. (2024). IsoplotR (Vermeesch, 2018) was used to calculate an isochron line and equivalent errors. The total age uncertainty was calculated using the same method as laser spot analysis above.

**Table 3: Standards used in Rb–Sr LA-ICP-MS analysis and their published ages and associated errors ( $2\sigma$  quoted).**

<b>Standard Name</b>	<b>Analysed Map Age (Ma)</b>	<b>Analysed Spot Age (Ma)</b>	<b>Ref. age (Ma)</b>	<b>Reference</b>
<b>MDC</b>	$511 \pm 3.9$	$491.9 \pm 6.2$	$519.4 \pm 6.5$	Reeda et al. 2021 Hogmalm et al. 2017
<b>Mica-MG nanopowder</b>	<b>NOT USED</b>	$488 \pm 5.9$	$519.4 \pm 6.5$	Glorie et al. 2024
<b>Ruby Mine muscovite</b>	$329 \pm 7.9$	<b>NOT USED</b>	$324 \pm 3$	Mortimer et al. 1987
<b>Robins Folly muscovite</b>	$338.7 \pm 5.6$	$330.6 \pm 2.1$	$332 \pm 2$	Mortimer et al. 1987
<b>Entire Creek pegmatite</b>	<b>NOT USED</b>	$320.5 \pm 3.4$	$312.1 \pm 5.1$	Glorie et al. 2024 Mortimer et al. 1987

#### IN-SITU URANIUM–LEAD AND TRACE ELEMENT CARBONATE MAPPING ANALYSIS

The method outlined by Drost et al. (2018) and Subarkah et al. (2024) was followed.

U–Pb isotopic analyses were acquired using the RESolution 193nm laser coupled with an Agilent 8900x ICP-MS/MS. Carbonate beds from drillholes NDILLK13 and NDILLK14 were selected to constrain the age of deposition. Carbonate veins were targeted to constrain deformation or alteration. Sample preparation followed the Rb–Sr raster mapping method above. Laser mapping was carried out with specific parameters presented in Table 4. Element dwell times are presented in Appendix 5. NIST610 was used to correct drift and quantify elements. A secondary correction was then applied using Excel based on the analysed versus published age of primary standard WC-1.

RA138, Mexican Tank and Duff Brown Tank were analysed as secondary standards (Table 5, references therein) to ensure the secondary correction from WC-1 was accurate.

**Table 4: Parameters for data acquisition of U–Pb carbonate mapping LA-ICP-MS analysis**

Sample ID	Date of session	Spot Size ( $\mu\text{m}$ )	# of rasters	Mapping Time (s)
LK12-186	1/08/2024	80	30	7050
LK12-173	1/08/2024	80	20	5020
LK12-173B	1/08/2024	80	41	5494
LK13-184	1/08/2024	80	51	6681
LK13-198	1/08/2024	80	36	5904
LK14-365	1/08/2024	80	31	6634
LK14-214	1/08/2024	80	31	6789
LK14-215	1/08/2024	80	26	6786
LK12-172U	1/08/2024	80	21	6153
P02-493	1/08/2024	80	31	7719
LK12-173U	1/08/2024	80	41	6888

**Table 5: Standards used in U–Pb LA-ICP-MS analysis, their analysed age, their published ages and associated errors ( $2\sigma$  quoted).**

Standard Name	Analysed Age +/- (Ma)	Ref. Age +/- (Ma)	Reference
WC1	$234.0 \pm 2.7$	$254.4 \pm 6.4$	Roberts et al. 2017
RA138	$324.9 \pm 2.8$	$321.99 \pm 0.65$	Guillong et al. 2024
Mexican Tank	$62 \pm 2$	$60.5 \pm 4.6$	Hill et al. 2016
Duff Brown Tank	$64.7 \pm 1.5$	$64.04 \pm 0.67$	Hill et al. 2016

Data were processed using Iolite4's U–Pb geochronology DRS (Petrus et al., 2017; Paton et al., 2011). Laser maps were smoothed using built-in box smoothing filters

including gaussian and median. Regions enriched in detrital proxy elements (Al, Si, Rb, Zr and Th) were used to select pixels for detrital carbonate in samples, while proxies for post-depositional alteration (Mn/Sr ratios, Fe and Y) determined regions of interest for carbonate veins. A minimum of 30 pixels comprised an analytical point. IsoplotR (Vermeesch, 2018) was used to calculate an isochron line.

## **OBSERVATIONS AND RESULTS**

### **General sample overview**

All drill cores have been logged by GA. The following paragraphs give an overview of the lithologies sampled in this study and their interpreted formation, with detailed petrography to follow.

### **SEDIMENTARY ROCKS**

The sedimentary rocks in this project overlie the passive margin sediments of the Pualco Tillite and Braemer Ironstone Formations (Mole et al., 2024). Fine grained laminated shales from hole NDILLK11 at depths of 369 m and 323 m and NDILLK12 between 172 m and 186 m were sampled. These are interpreted to form part of the Torrawangee Group, described by Clark et al. (2024) as the most texturally and compositionally mature sedimentary rocks in the LLKB. Recent Sensitive High Resolution Ion Microprobe (SHRIMP) U–Pb dating indicates a maximum depositional age of *ca.* 604 Ma making them comparable to other Cambrian to Neoproterozoic sedimentary rocks of the Delamerian Orogen such as the Wilpena Group (Heysen Supergroup) (Mole et al., 2024).

Samples from holes NDILLK13 taken from between 194 m and 215 m and NDILLK14 from 365 m to 379 m contain similar sedimentary packages to the Torrawangee Group shales of NDILLK11, however, they contain consistent sub-millimetre scale carbonate beds. These are part of the newly named middle Cambrian Danggali Formation and show similarities to the Ponto Group sedimentary rocks in the Koonenberry Belt (Clark et al., 2024), constrained to have been deposited between 585–515 Ma and are indicative of the formation of a deepening basin likely associated with the onset of subduction in the Koonenberry Belt (Johnson et al., 2016).

## IGNEOUS SAMPLES

Medium and fine-grained intermediate intrusions from NDIWMP02 and NDIWMP03 and ultra-fine grained mafic dykes present in NDILLK12 were sampled.

The fine-grained mafic dykes from drillhole NDILLK12 are presently unnamed by GA since their discovery in 2023 (Mole et al., 2024) but have been interpreted to have a maximum age of *ca.* 497 Ma from U–Pb SHRIMP analysis of zircons. They appear unique to the LLKB with no obvious links to other suites in the Delamerian from preliminary analysis (Mole et al., 2024).

Samples from drillholes NDIWMP02 and NDIWMP03 in the LWB range from granitic to granodioritic in composition based on their geochemistry but are currently unnamed (Mole et al., 2024). Recent U–Pb SHRIMP analysis of zircons suggest a formation age *ca.* 510–500 Ma (Mole et al., 2024). These ages align with Stavelly Arc suites but are younger than equivalent samples in the Koonenberry Belt.

Altered regions in the drill cores including dyke-shale contact halos and albitic hematite alteration of host rock were analysed with the purpose of constraining fluid flow ages and post formation tectonic processes in the LLKB. Sample images and equivalent sample names are available in Appendix 2

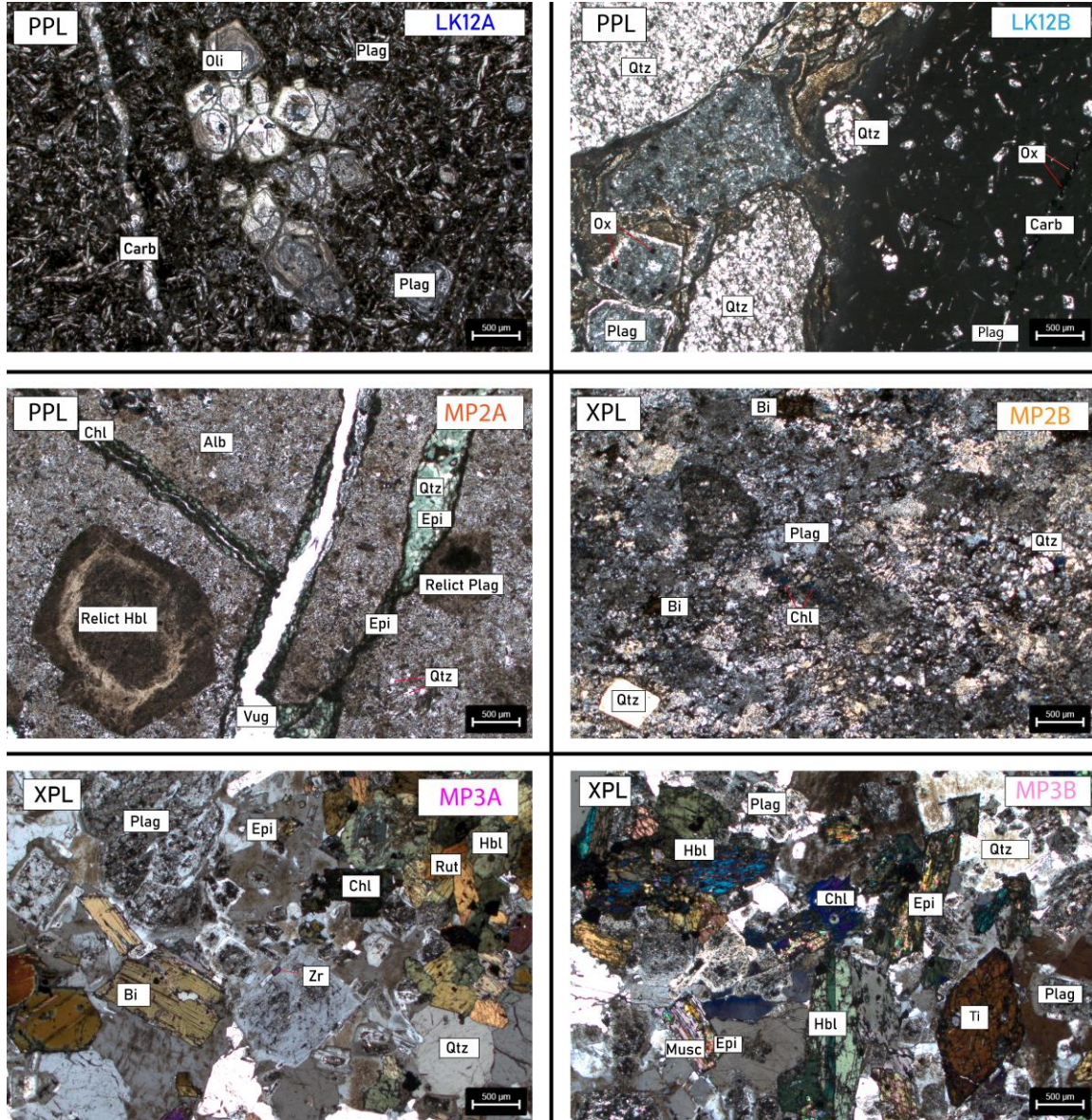
## **Petrography**

Petrographic analysis was conducted on thin sections using petrographic microscopy and SEM imaging for the purpose of deducing mineral assemblages, relationships and in the case of reflected light imaging, deducing oxide types. The main mineral phases have been highlighted in Figure 4. Table 6 presents the key minerals and textural observations found in samples using the petrographic microscope and mineral modes determined using MLA mapping analysis. A full petrographic description for each sample is available in Appendix 3.

**Table 6: Table of thin section selections of igneous rocks for analysis and its geochemical sample name equivalent. Where mineral composition % is to two decimal figures, they have come from MLA mapping. Only major mineral phases have been included in the table.**

Sample	Geochem equivalent	Description	Rock Type	Mineral Composition
LK12-172	LK12A	Fine-grained intrusion dominated by glass (>70%) groundmass. Fine grained, tabular plagioclase crystals and highly altered coarse-grained ex-olivine crystals and plagioclase are the only obvious minerals. Sample is crosscut by multiple generations of carbonate veins.	Olivine basalt (Mole et al., 2024)	Groundmass – 70% Ex-olivine – 20% Plagioclase – 5% Carbonate – 5%
LK12-173	LK12B	Equivalent intrusion to <b>LLK12-172</b> but contains the contact with the host shale. Intrusion dominated by glass (>60%) groundmass with fine-grained tabular muscovite oriented in direction of contact. Intrusion contains disseminated and veined pyrite. The veins are carbonate. The alteration halo is dominated by carbonate bearing minerals.	Olivine basalt (Mole et al., 2024)	Kaersutite – 37.31% Muscovite – 9.78% Magnesiohornblende – 6.67% Chlorite – 5.97% Ankerite – 1.56% Biotite – 18.27% Quartz – 9.64% Albite – 5.07%
MP02-556	MP2A	Sample completely dominated by albite alteration. Evidence for original plagioclase and hornblende remains but recrystallised. Breccia infill veins filled with calcite + chlorite + epidote + quartz and small amounts titanite. Potassic alteration present away from veins.	Albite breccia	Albite – 49.86% Quartz – 30.42% Orthoclase - 6.52% Chlorite – 4.04% Biotite – 1.99% Calcite – 1.63%
MP02-628	MP2B	Fine-grained igneous intrusive. Sample contains a very simple mineralogy of quartz, plagioclase, biotite and chlorite. The coarsest mineral phase is biotite, which grows in isolated clumps throughout. Chlorite replacement of this biotite occurs around the rim of these clumps.	Granite	Quartz – 40% Plagioclase – 35% Biotite – 23% Chlorite – 2%
MP03-493	MP3A	Coarse-grained intrusion containing iron-stained quartz, sieve-textured plagioclase, hornblende, rutile, biotite and zircon. Alteration assemblage of epidote + chlorite replacing biotite. Plagioclase with sieve texture and hornblende prevalent. Zircon and rutile are minor phases. Largest mineral is plagioclase.	Granodiorite	Quartz – 30% Plagioclase – 30% Hornblende – 20% Biotite – 10% Chlorite – 5% Muscovite – 4% Zircon – <1%
MP03-548	MP3B	Hornblende is the largest mineral phase along with sieve-textured plagioclase and large titanite crystals which are not present in <b>MP03-493</b> . Alteration of biotite significantly more prevalent in this sample with original biotite almost completely replaced by chlorite. Quartz has more iron staining than <b>MP03-493</b> .	Granodiorite	Quartz - 31.252% Albite – 17.55% Orthoclase – 15.22% Anorthite – 10.70% Magnesiohornblende – 7.33% Chlorite – 7.02% Muscovite – 4.78% Epidote – 2.25%





**Figure 4:** Thin section photos taken of igneous samples from LLKB captured in both PPL and XPL (labelled top left corner). Main minerals labelled in white boxes. Abbreviations: Oli = Olivine; Qtz = quartz; Plag = plagioclase; Carb = carbonate; Ox = pyrite; Musc = muscovite; Chl = chlorite; Epi = epidote; Vug = hole; Hbl = hornblende; Ti = Titanite; Zr = Zircon. Colour of sample name correlates to equivalent geochemical analysis sample.



SEM

MLA/BSE MAPS

Sample LK12-173

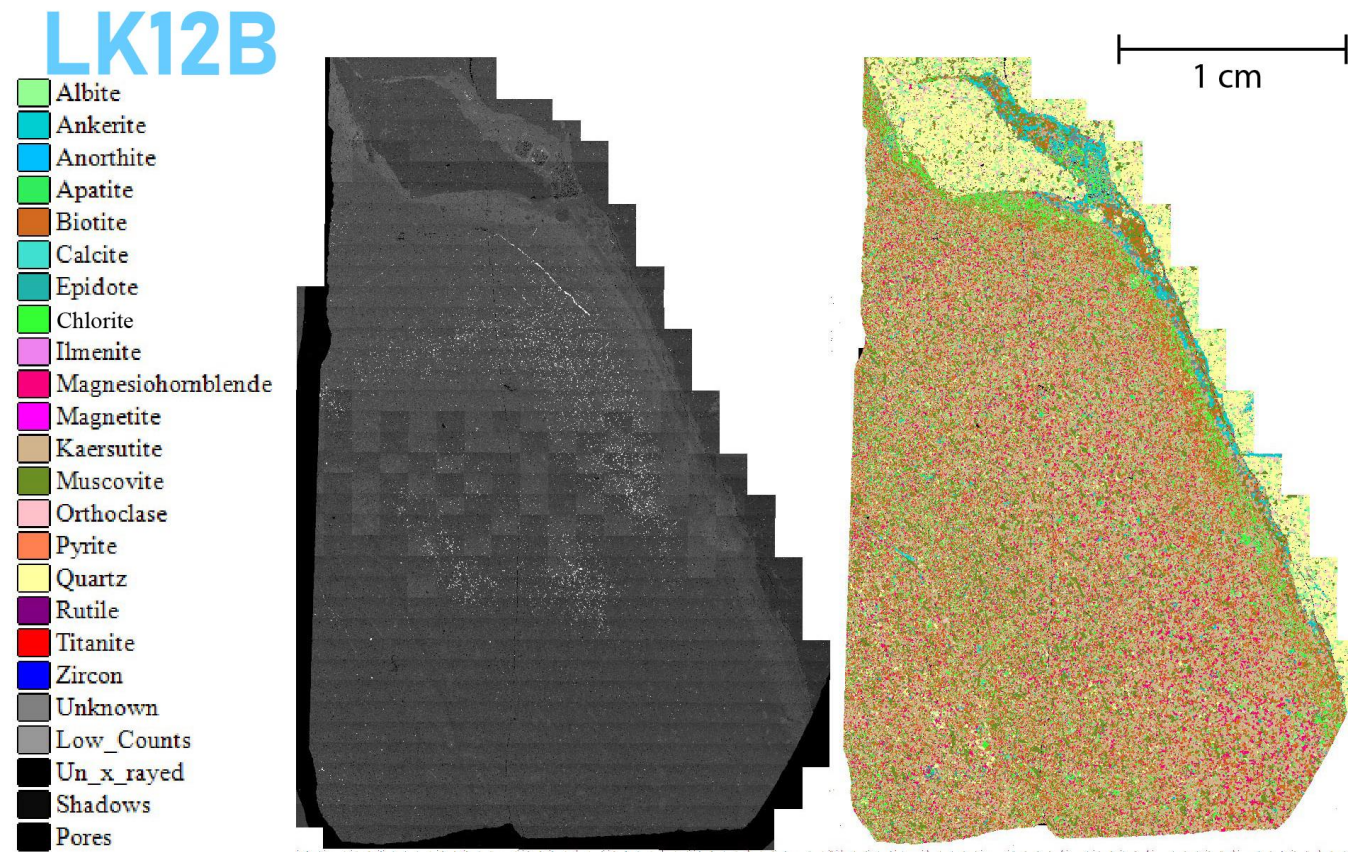


Figure 5: Back scatter electron map (middle), mineral liberation analyser (MLA) map (right) and mineral legend (left) of thin section sample LK12-173 and geochemical equivalent LK12B. Mineral Mode percentages of MLA mapping of major minerals found in Table 6.



Sample MP02-556

# MP2A

- Albite
- Ankerite
- Anorthite
- Apatite
- Biotite
- Calcite
- Epidote
- Chlorite
- Ilmenite
- Magnesiohornblende
- Magnetite
- Kaersutite
- Muscovite
- Orthoclase
- Pyrite
- Quartz
- Rutile
- Titanite
- Zircon
- Unknown
- Low\_Counts
- Un\_x\_rayed
- Shadows
- Pores

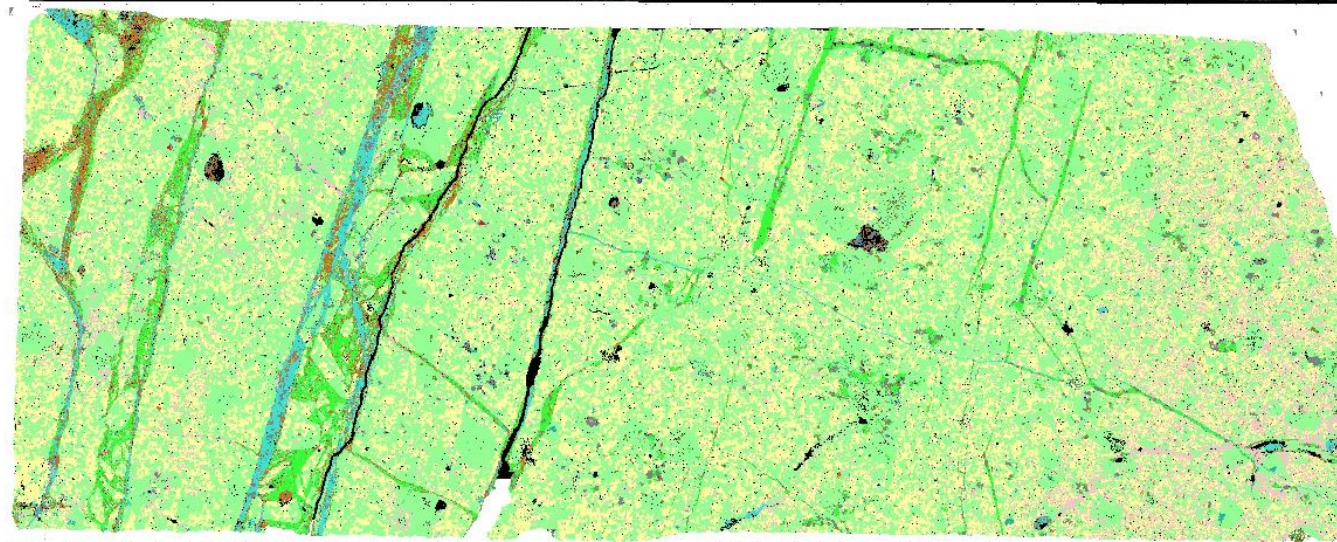
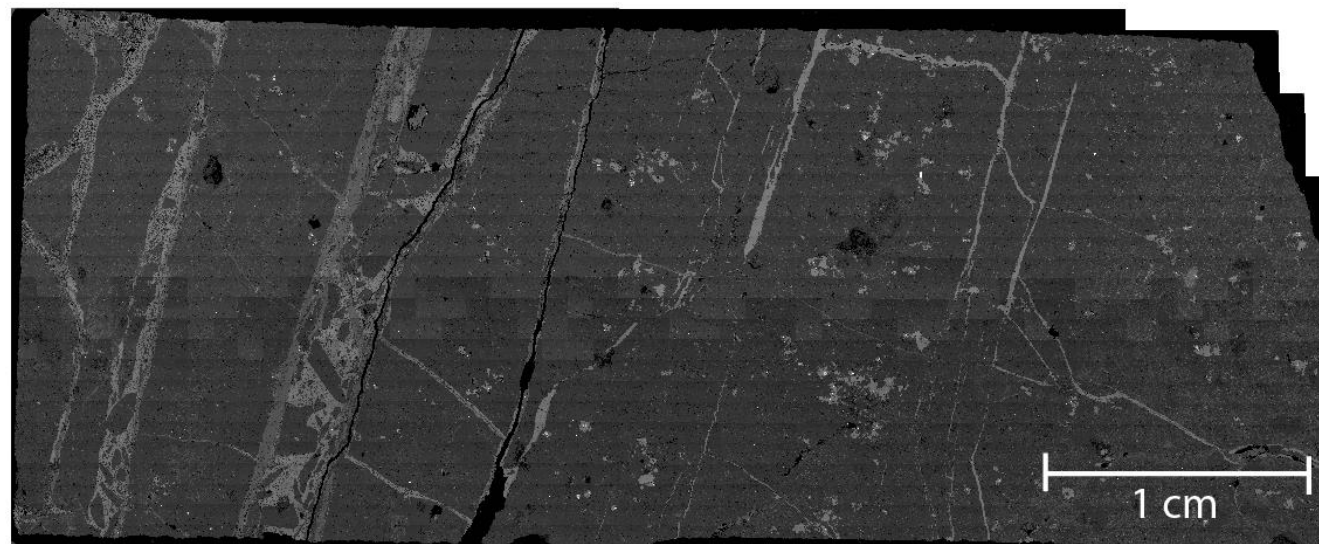


Figure 6: Back scatter electron map (top), mineral liberation analyser (MLA) map (bottom) and mineral legend (left) of thin section sample MP02-556 and geochemical equivalent MP2A. Mineral mode percentages of MLA mapping of major minerals found in Table 6.



Sample MP03-548

MP3B

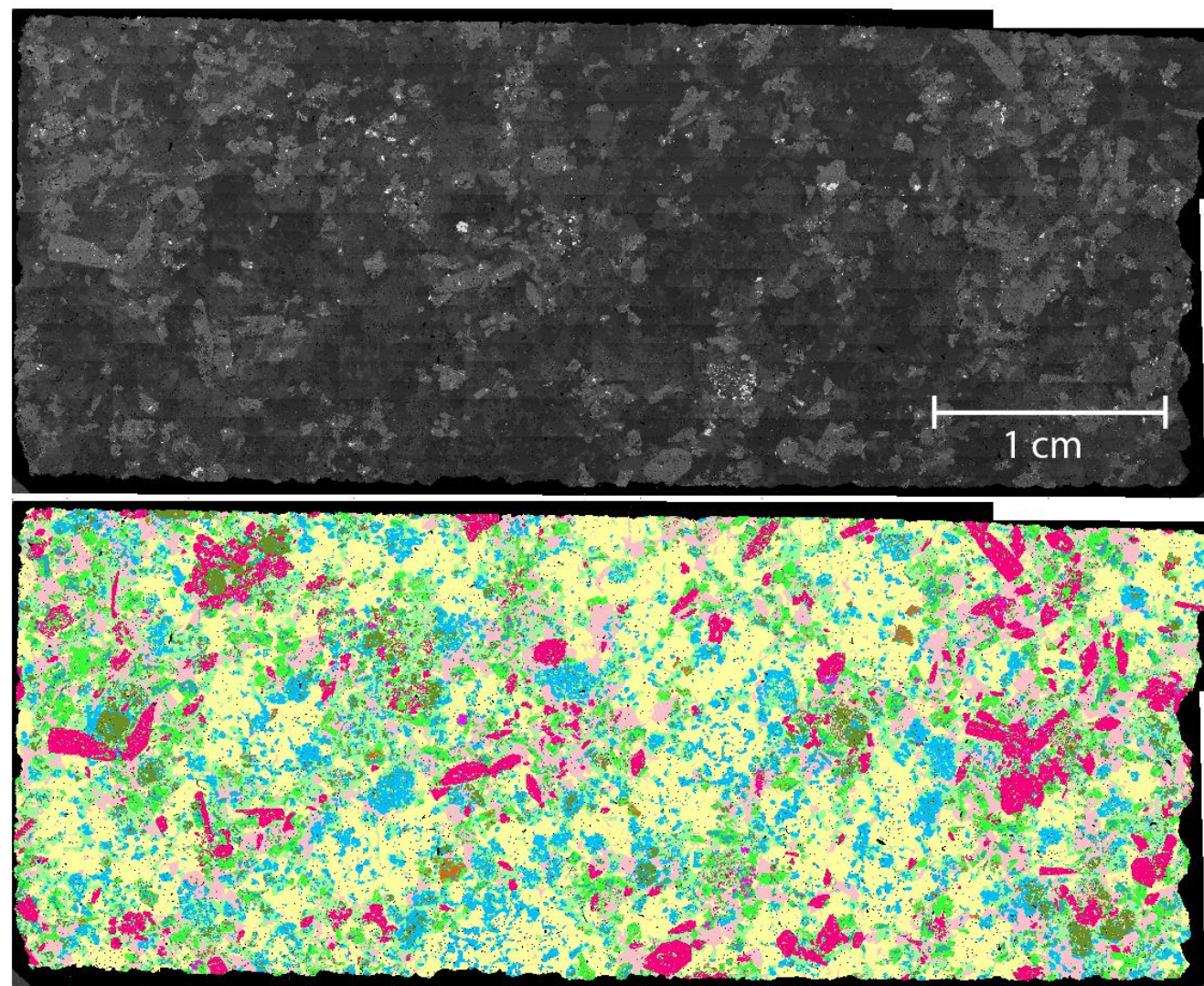


Figure 7: Back scatter electron map (top), mineral liberation analyser (MLA) map (bottom) and mineral legend (left) of thin section sample MP03-548 and geochemical equivalent MP3B. Mineral mode percentages of MLA mapping of major minerals found in Table 6.

## Geochemistry

### SOLUTION ICP-MS

Six igneous samples were selected for major and trace element analyses with whole rock images available in Appendix 2. Data are displayed on spider plots (Figure 8) whereby REEs were normalised to values for C1 chondrites (Anders & Grevesse, 1989), while major and trace elements were normalised to primitive mantle values (McDonough & Sun, 1995) (Figure 8). All elemental concentrations are available in Appendix 14. Below are selected and representative values from the samples analysed in this study (Table 7 and 8). They form the basis for the following paragraphs. Based on the results of ICP-MS, two separate suites appear to exist and will be discussed separately: the LK12 dykes, and MP granites and granodiorites.

**Table 7: Oxide weight percent values, europium and niobium anomalies and REE slopes calculated from solution ICP-MS analysis of igneous samples.**

Sample	Mg#	TiO <sub>2</sub> (wt%)	P <sub>2</sub> O <sub>5</sub> (wt%)	Fe <sub>2</sub> O <sub>3</sub> (wt%)	Eu/Eu*	Nb/Nb*	Total REE slope (La/Lu)	LREE slope (La/Sm)	HREE slope (Gd/Lu)
LK12A	45.83	1.50	0.43	8.67	0.86	0.57	9.34	2.69	2.23
LK12B	30.90	1.72	0.48	12.20	0.80	0.64	7.60	2.46	1.93
MP2A	10.89	0.22	0.05	2.05	0.48	0.14	8.78	3.62	1.57
MP2B	9.35	0.22	0.05	2.34	0.53	0.14	8.95	3.63	1.62
MP3A	26.75	0.56	0.12	5.74	0.61	0.14	10.10	3.85	1.69
MP3B	26.04	0.57	0.12	5.96	0.58	0.13	12.22	4.43	1.76

**Table 8: Table showing detected ppm values of selected elements present in six igneous samples from LLKB in 1:1000 and 1:1000000 dilution samples run on solution ICP-MS.**

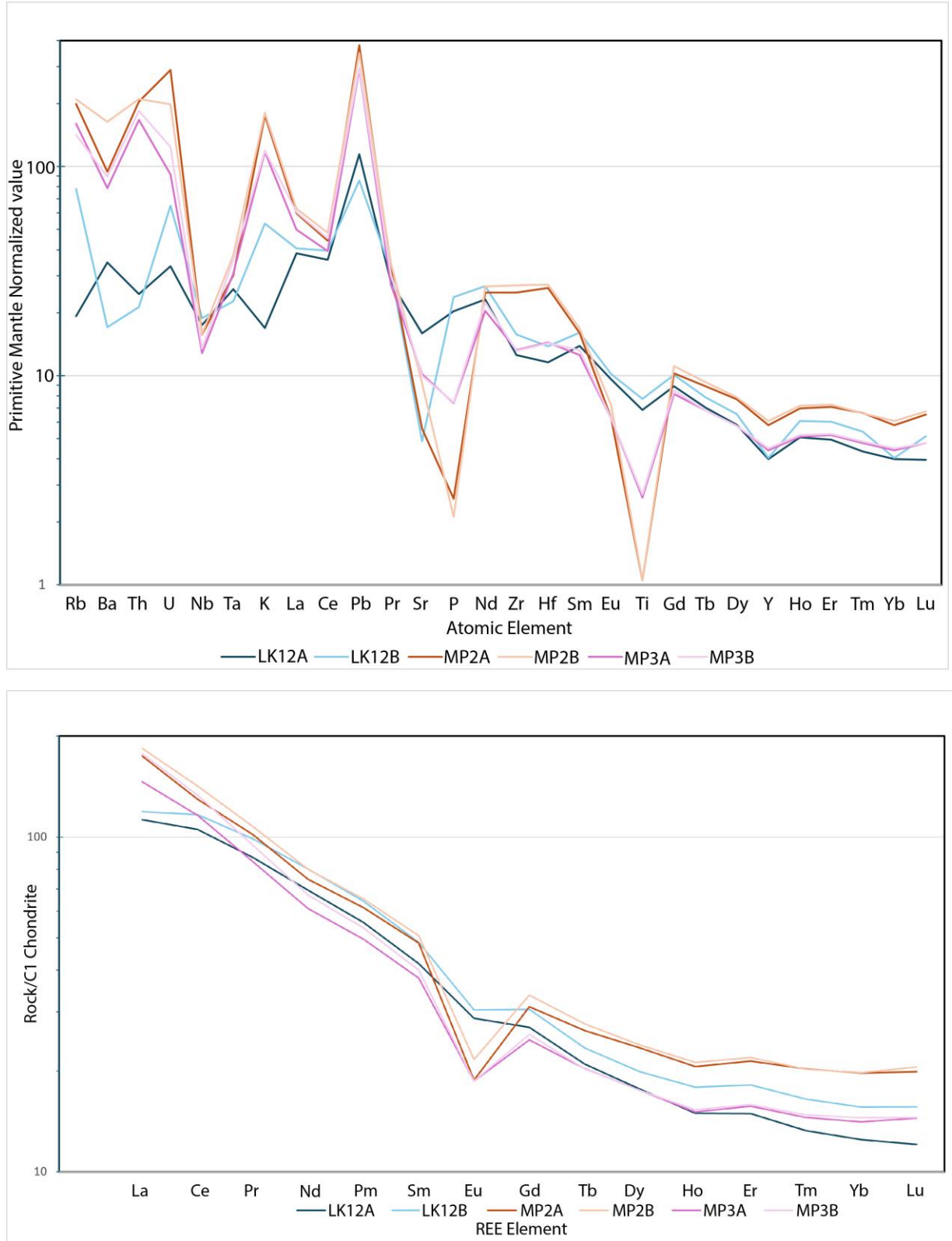
Element conc. (PPM)	LK12A	LK12B	MP2A	MP2B	MP3A	MP3B
Li	35.57	61.92	7.67	15.63	31.41	14.71
Mg	42271.31	31780.13	1670.28	1626.49	13919.08	13675.18
P	1935.62	2269.08	244.15	202.61	709.53	711.44
Ca	62964.18	41148.69	7147.30	20195.41	39332.32	34881.68
Ti	8937.40	10143.43	1364.18	1380.02	3433.51	3533.39
V	199.75	225.43	5.62	3.96	111.34	111.44
Cr	234.41	212.34	1.33	0.67	41.37	30.60
Mn	920.62	1068.49	250.56	230.51	687.09	773.10
Fe	56293.45	77812.60	13392.25	15578.42	37633.12	39085.19
Ni	117.87	99.33	0.58	0.59	9.54	9.64
Cu	41.13	37.51	12.91	10.58	14.88	12.24
Rb	12.27	49.96	125.89	134.56	102.89	90.64
Ba	243.65	120.01	657.57	1154.54	557.03	626.92
Pb	8.16	6.14	26.88	25.06	21.01	21.19
Th	2.09	1.82	17.35	18.07	14.39	15.77

#### LK12 olivine basalt dykes

The samples from drillhole NDILLK12 to the north-west (LK12A and LK12B) are differentiated by their large Mg# of greater than 30 and largest proportion of compatible oxides in the project with percentages for titanium, phosphorus and iron oxides of greater than 1.5, 0.43 and 8.67 respectively (Table 7). They have relatively small europium anomalies (0.86 and 0.8) and slightly larger niobium anomalies (0.57 and 0.64). They contain larger LREE slopes (2.69 and 2.46) than heavy rare earth element (HREE) slopes (2.23 and 1.93) (Table 7) and contain significant proportions of compatible elements including titanium, vanadium, chromium and nickel (Table 8) indicative of their mafic nature. They contain lower than expected cerium and lanthanum values based on their REE pattern (Figure 8).

### MP2 and MP3 granites/granodiorites

The samples from drillholes NDIWMP02 and NDIWMP03 further southeast in the LLKB are defined by enrichment in incompatible elements and ‘spikier’ nature of trace element pattern (Figure 8). They show the classic signature for an evolved formation history with Rb, Th, Ba and U all more than 90x more concentrated than primitive mantle values, while Pb is more than 300x more concentrated (Figure 8). They contain moderate europium anomalies, with the MP2 granites values being larger (0.48 and 0.53) than MP3 (0.61 and 0.58). They contain very similar but large niobium anomalies of 0.14 in the case of MP2 samples and 0.13 and 0.14 for MP3 samples. They preserve much larger LREE slopes (between 3.62 and 4.43) than HREE slopes (between 1.57 and 1.76) (Table 7). Although they are remarkably similar, the MP2 and MP3 suites contain some subtle differences. Firstly, while their trace element plots are almost identical, the MP2 samples are significantly depleted in some compatible elements (P, Ti and Sr) (Figure 8) and though they contain a similar HREE slope and trend, the MP2 samples appear more enriched in HREE elements than MP3 samples (Figure 8).



**Figure 8: TOP- Spiderplot of trace element concentrations of igneous samples from LLKB normalised to primitive mantle values (Sun & McDonough, 1995). BOTTOM- Spiderplot of REE element concentration in igneous samples from LLKB normalised to C1 chondrite values (Anders & Grevesse, 1989). Both are plotted on a log scale.**



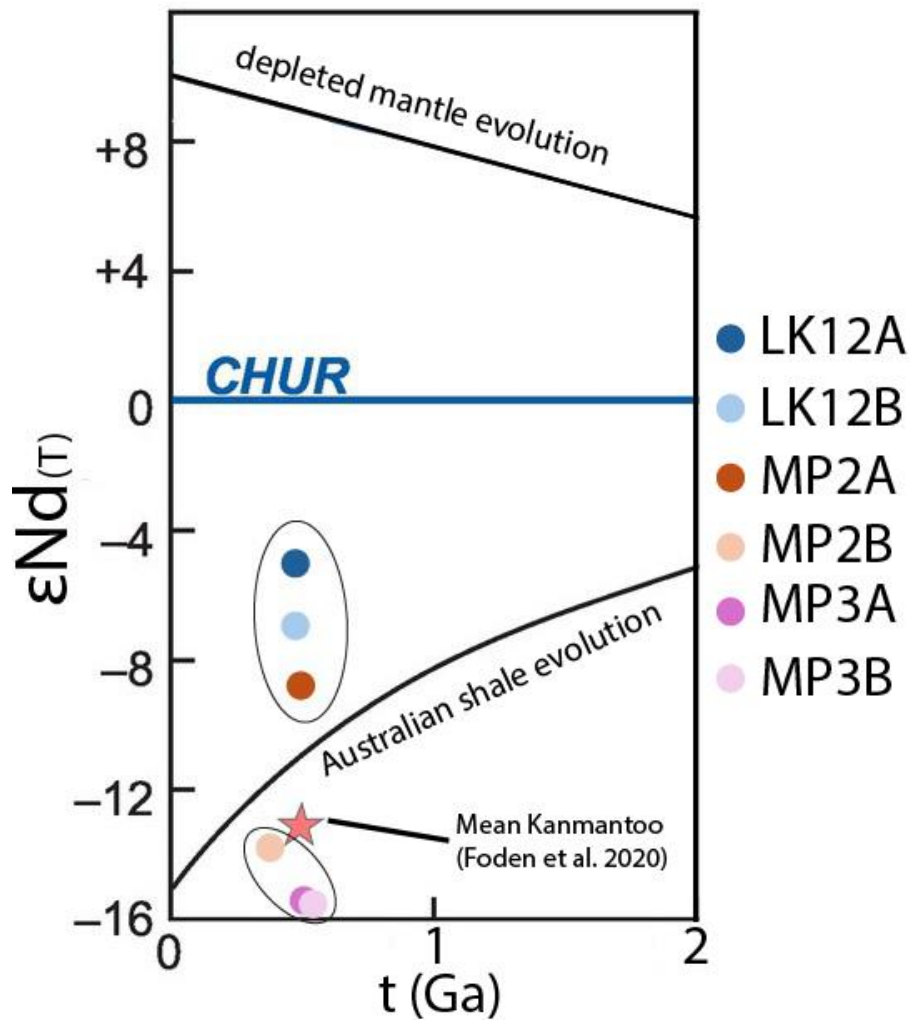
## SM–ND TIMS ANALYSIS OF IGNEOUS SAMPLES

The six samples above were analysed using TIMS to determine Sm–Nd isotopic ratios.

Values obtained are presented below (Table 9):

**Table 9: Table of values calculated from Sm–Nd isotope analysis using MASS facilities at University of Adelaide. Note that input ages may reflect alteration events and so Sm–Nd values aren’t representative of the source rock.**

Sample name	MP2A	MP2B	MP3A	MP3B	LK12A	LK12B
<i>input age of rock T (Ma)</i>	<i>490</i>	<i>490</i>	<i>484</i>	<i>509.5</i>	<i>426</i>	<i>426</i>
Unmixed 143/144Nd	.511923	.511909	.511849	.511847	.512379	.512276
Nd $\mu\text{g g}^{-1}$	35.6	35.4	27.5	29.6	31.1	37.2
Sm $\mu\text{g g}^{-1}$	6.8	7.0	5.1	5.2	5.7	6.7
147Sm/144Nd	.1159	.1190	.1127	.1066	.1110	.1096
$\epsilon\text{Nd (T=0)}$	-13.95	-14.22	-15.39	-15.43	-5.06	-7.05
143Nd/144Nd (T)	.511536	.511909	.511849	.511847	.512379	.512276
$\epsilon\text{Nd (T)}$	-8.70	-14.22	-15.39	-15.43	-5.06	-7.05
TDM (Ma)	1890	1974	1942	1836	1136	1268
TCHUR (Ma)	1348	1429	1432	1338	463	634
DM at age of rock (T)	.512434	.513150	.513150	.513150	.513150	.513150
CHUR at age of rock (T)	.511982	.512638	.512638	.512638	.512638	.512638



**Figure 9:** Scatterplot showing the obtained  $\epsilon\text{Nd}(T)$  values from TIMS analysis of Sm & Nd isotopes (Y-axis) against time (Ga) (X-axis) of samples obtained using TIMS Sm–Nd analysis. Red star depicts mean Kanmantoo  $\epsilon\text{Nd}(T)$  from Foden et al. (2020). Depleted mantle evolution line, Chondritic Uniform reservoir (CHUR) line and Australian shale  $\epsilon\text{Nd}(T)$  evolution values from Rollinson & Pease (2021) plotted. After Rollinson & Pease (2021).

The samples analysed returned values in two regions denoted by the ovals seen in Figure 9. Samples LK12A and LK12B yielded  $\epsilon\text{Nd}(t)$  values of -5.06 and -7.05, respectively, while MP3A and MP3B obtained more evolved values (-15.39 and -15.43). Interestingly, MP2A and MP2B recorded more disparate values, with MP2A significantly less evolved ( $\epsilon\text{Nd}(t) = -8.7$ ) than MP2B ( $\epsilon\text{Nd}(t) = -14.22$ ) (Figure 9).

## Geochronology

### RB–SR AGES OF SPOT ANALYSED SHALES AND INTRUSIONS

The Rb–Sr radiogenic system was used to analyse shales for their minimum age of deposition by targeting illite, while igneous intrusions targeted micas to deduce a crystallisation age. A total of nine samples were analysed (5 shales and 4 intrusions). Sample descriptions are available in Appendix 2.

All intrusions analysed were fine-grained or altered making targeting micas a challenge. Samples equivalent to those analysed in geochemistry and thin section were selected with MP02-556 and MP02-628 equivalent to MP2A and MP2B, respectively and MP03-493 and MP03-548 equating to MP3A and MP3B. Results for all igneous samples analysed are available (Table 10, Figure 10).

A total of 59 spots were analysed from sample MP03-548 yielding an age of  $510 \pm 12$  Ma ( $2\sigma$ ) with  $^{87}\text{Sr}/^{86}\text{Sr}_{(i)}$  of 0.7094 (Figure 10).

Sample MP02-628 returned an age of  $389 \pm 99$  Ma ( $2\sigma$ ) with  $^{87}\text{Sr}/^{86}\text{Sr}_{(i)}$  of 0.7157, the large error reflects a limited spread in  $^{87}\text{Rb}/^{86}\text{Sr}$  (Figure 10).

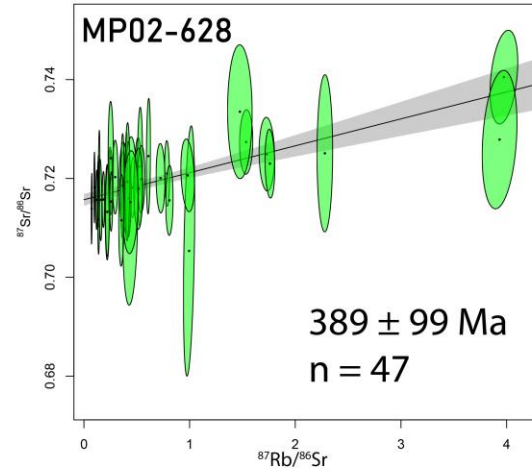
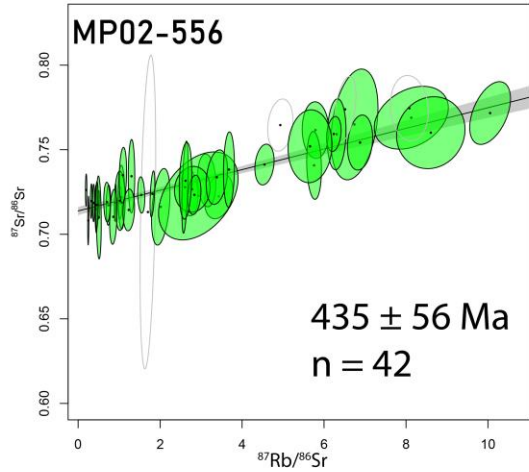
Of the 5 shales, sample LK11-323 yielded the youngest age, at  $533 \pm 39$  Ma ( $2\sigma$ ) with an  $^{87}\text{Sr}/^{86}\text{Sr}_{(i)}$  of 0.7137. A total of 56 spots were analysed (Figure 11). All other shale samples analysed returned ages between  $549 \pm 24$  Ma and  $616 \pm 55$  Ma. All ages were within uncertainty of each other (Figure 11). All samples had similar  $^{87}\text{Sr}/^{86}\text{Sr}_{(i)}$ , between 0.7100 and 0.7168 (Table 10, Figure 11).

Table 10: Summary of Rb–Sr ages and associated errors (2 $\sigma$  quoted).

Sample ID	Sample Type	Depth (m)	Initial $^{87}\text{Sr}/^{86}\text{Sr}_0$	+ / -	Age (Ma)	Analysed age uncertainty (Ma)	MSWD	Total age uncertainty (Ma)
LK11-323	Shale	323	0.7137	0.0022	533	38	0.77	39
LK11-369	Shale	369	0.714	0.002	550	36	1.2	38
LK12-186	Shale	186	0.7168	0.0094	616	54	1.4	55
LK14-361	Shale	361	0.7104	0.0048	549	21	1	24
LK14-379	Shale	379	0.71	0.01	591	50	0.84	51
MP02-556	Granite	556	0.7138	0.0024	435	53	1.1	56
MP02-628	Granite	628	0.7157	0.0012	389	97	0.88	99
MP03-493	Granodiorite	493	0.7129	0.0019	484	16	1.1	20
MP03-548	Granodiorite	548	0.7094	0.0035	510	6.3	3	12

$(^{87}\text{Rb}/^{86}\text{Sr})_0 = 0.7138 \pm 0.0024$   
MSWD = 1.1,  $p(\chi^2) = 0.3$

$(^{87}\text{Rb}/^{86}\text{Sr})_0 = 0.7157 \pm 0.0012$   
MSWD = 0.88,  $p(\chi^2) = 0.7$



$(^{87}\text{Rb}/^{86}\text{Sr})_0 = 0.7129 \pm 0.0019$   
MSWD = 1.1,  $p(\chi^2) = 0.25$

$(^{87}\text{Rb}/^{86}\text{Sr})_0 = 0.7094 \pm 0.0035$   
MSWD = 3,  $p(\chi^2) = 1.3 \times 10^{-12}$

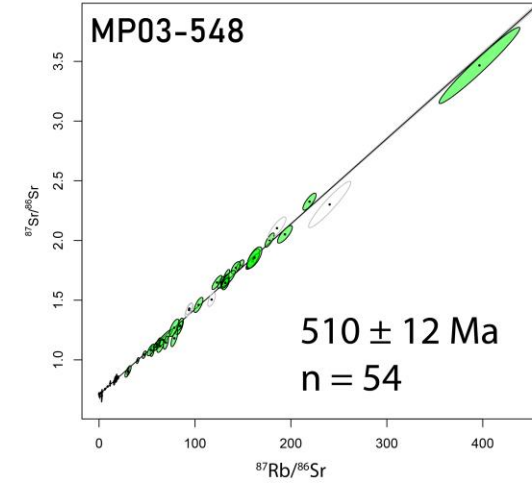
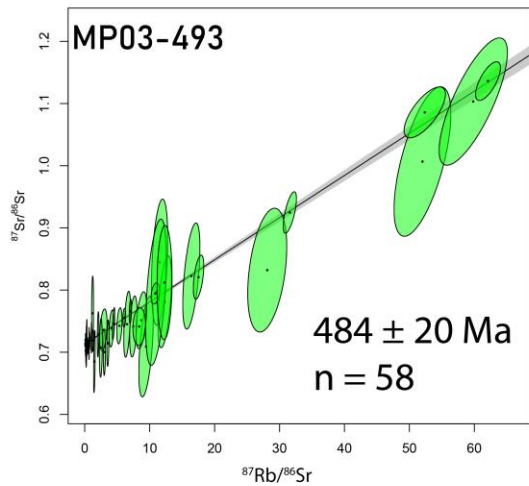
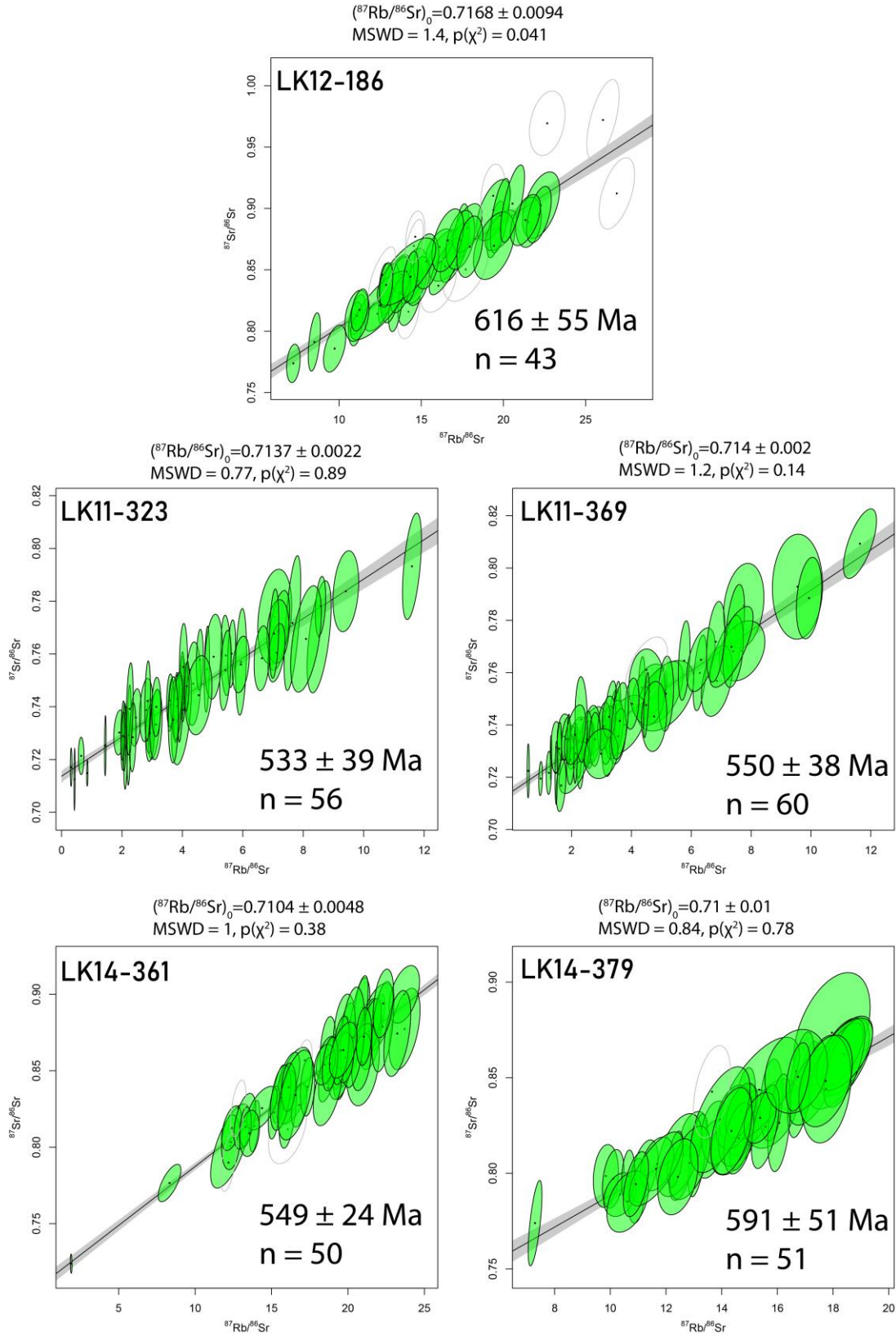


Figure 10: Isochrons from analysed intrusion samples with ages and initial  $^{87}\text{Sr}/^{86}\text{Sr}$  values along with associated propagated 2 $\sigma$  errors and mean square weighted deviation (MSWD). Sample name equates to drill hole and depth in hole. Age uncertainty is quoted as total age uncertainty.



**Figure 11: Isochrons from analysed shale samples with ages, initial  $^{87}\text{Sr}/^{86}\text{Sr}$  values along with associated errors and mean square weighted deviation (MSWD). The uncoloured circles indicate removed analysis points. Sample name equates to drill hole and depth in hole. Age uncertainty is quoted as total age uncertainty.**

## LA-ICP-MS RB–SR AGES OF RASTER ANALYSED ALTERATION TEXTURES

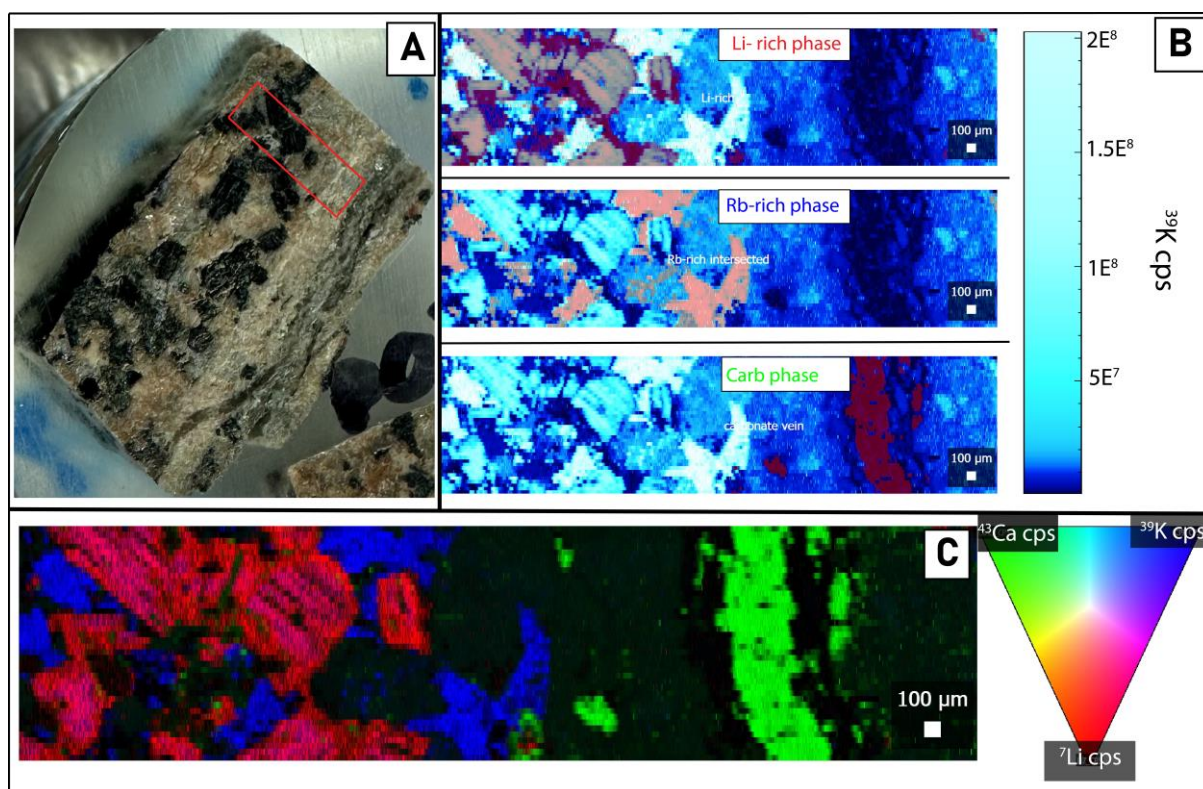
Seven samples were analysed over two separate sessions. Imaging capabilities of Iolite4 (Petrus et al., 2017; Paton et al., 2010) were used to deduce different alteration regions.

Sample descriptions are available in Appendix 2.

Samples from drill hole ID NDILLK12, NDIWMP02 and NDIWMP03 were analysed.

Each sample will be discussed individually as samples have multiple phases. The four other samples analysed utilising Rb–Sr geochronology not discussed here are available in Appendices 9 through 12 but are presented in Table 11 along with the samples below.

### Sample MP03-493



**Figure 12:** A) Sample MP03-493 mounted in epoxy with the red box depicting the mapped region; B) The three distinct pixel maps for phases (Li-rich, Rb-rich & Carb rich) present in sample MP03-493 (red regions) overlain on  $^{39}\text{K}$  concentration map (left) and  $^{39}\text{K}$  scale (right); C) The three distinct phases in B compiled into one ternary diagram showing their respective spatial relationships to each other.



LA-ICP-MS analysis of this sample yielded three distinct mineral phases (Figure 12B). There is a Li, Ti-rich phase that dominates the left portion of the analysed map (Figure 12; C). These are the largest minerals in the sample, up to 300 $\mu$ m in diameter. There is a finer grained Rb, K-rich phase that seems to dominantly fill space between the Li, Ti phases. A third, Ca-rich phase exists, filling the entire right portion of the map (Figure 12; C). This phase will not be discussed further here as it is a carbonate and therefore unsuitable for Rb–Sr geochronology. All phases have been overlaid on a  $^{39}\text{K}$  map for consistency. Maps for all analysed elements are available in Appendix 6.

The Li, Ti-rich phase (MP03-493-Li) was the oldest phase, returning an age of  $505 \pm 10$  Ma ( $2\sigma$  error) with  $^{87}\text{Sr}/^{86}\text{Sr}_{(i)}$  of 0.7105 (n=99) (Figure 13). The Rb-rich phase (MP03-493-Rb) was younger, returning an age of  $403 \pm 13$  Ma ( $2\sigma$  error) with  $^{87}\text{Sr}/^{86}\text{Sr}_{(i)}$  of 0.7130 (n=99) (Figure 13).

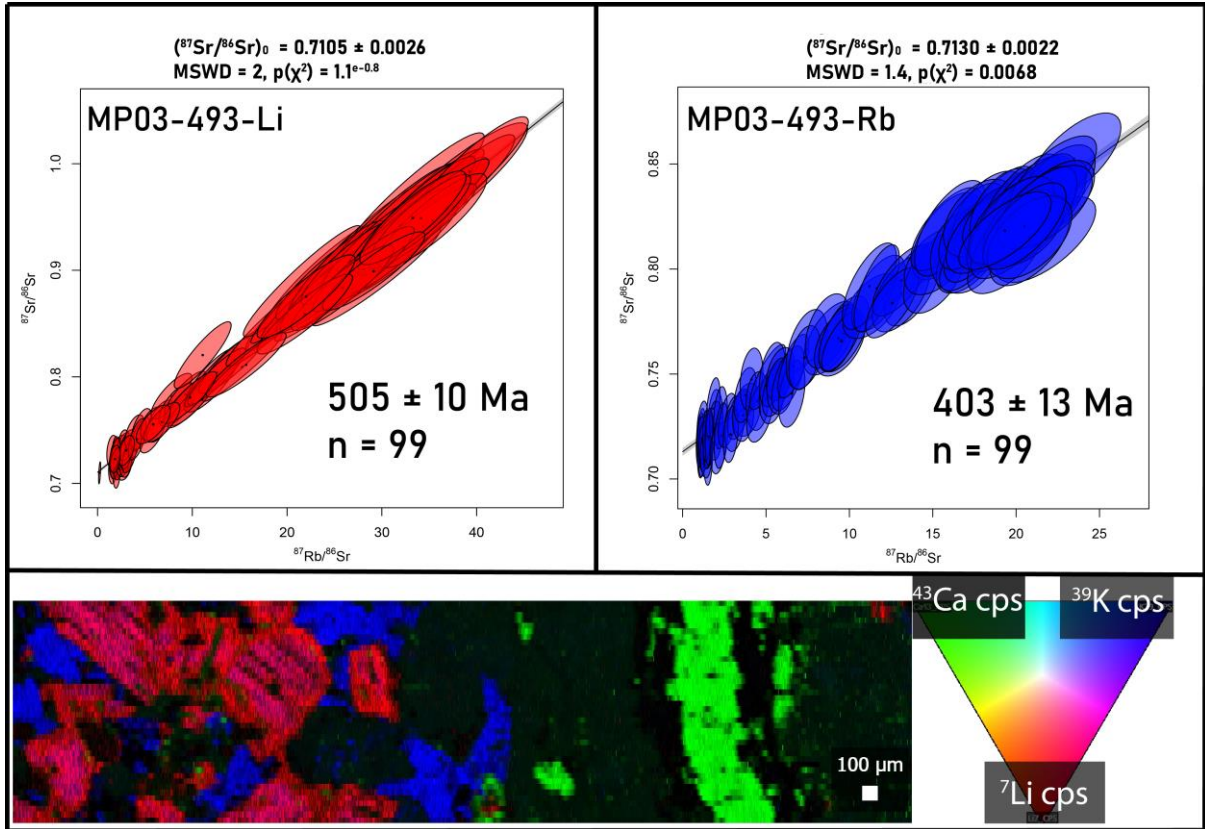
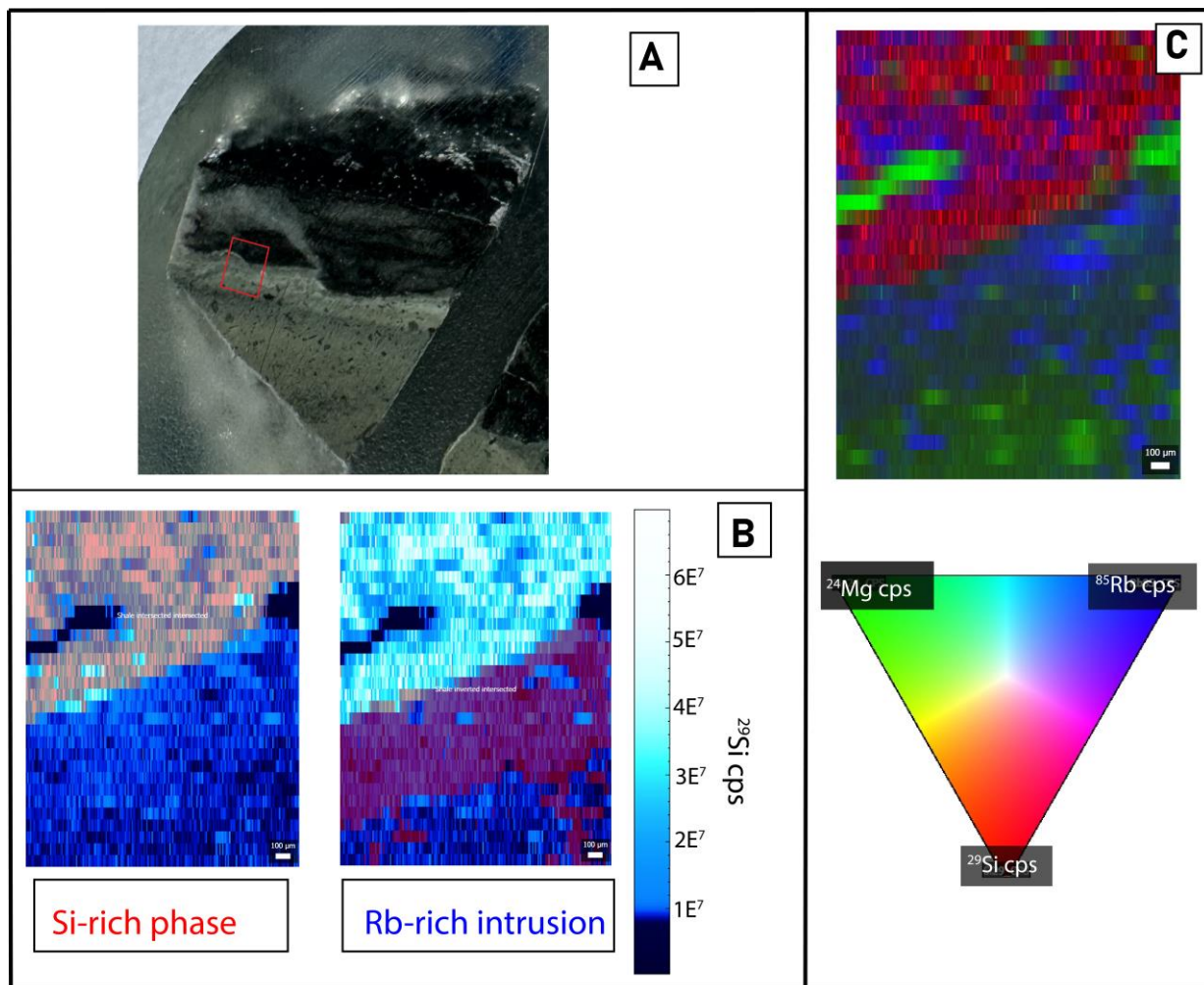


Figure 13: (TOP) Isochrons for phase MP03-493-Li (Left) and MP03-493-Rb (Right) with ages and  $^{87}\text{Sr}/^{86}\text{Sr}_{(i)}$  along with associated  $2\sigma$  errors and mean square weighted deviation (MSWD). (BOTTOM) ternary map of the pixel regions which each isochron was analysed from. Each isoplot is colour coded to its colour in the ternary map.



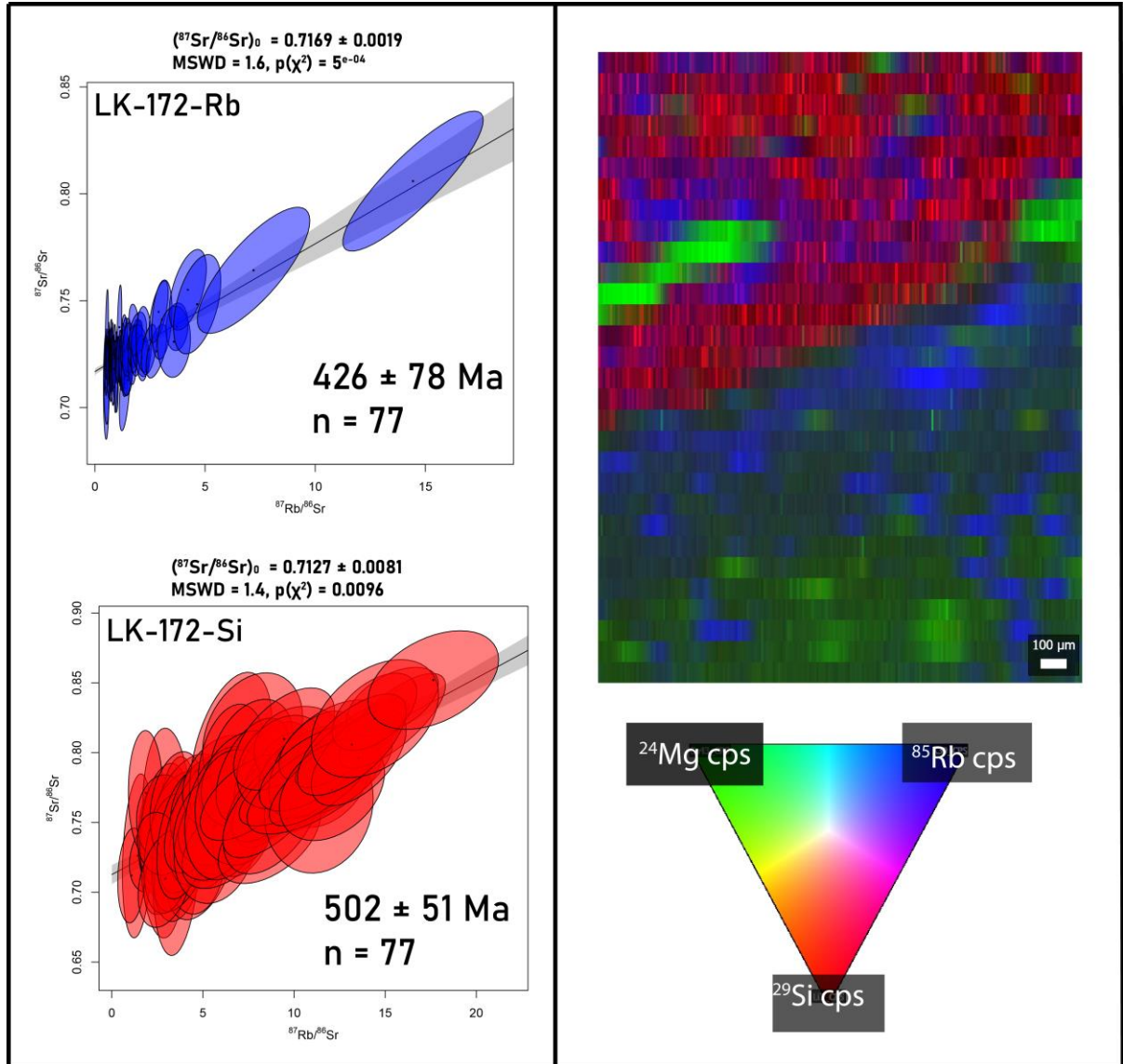
Sample LK-172



**Figure 14:** A) Sample LK-172 mounted in epoxy with the red box depicting the mapped region; B) Two distinct pixel maps for phases (Si-rich & Rb-rich) present in sample LK-172 (red regions) overlain on  $^{29}\text{Si}$  concentration map (left) and  $^{29}\text{Si}$  scale (right); C) The two distinct phases in B compiled into one ternary diagram showing their respective spatial relationships to each other.

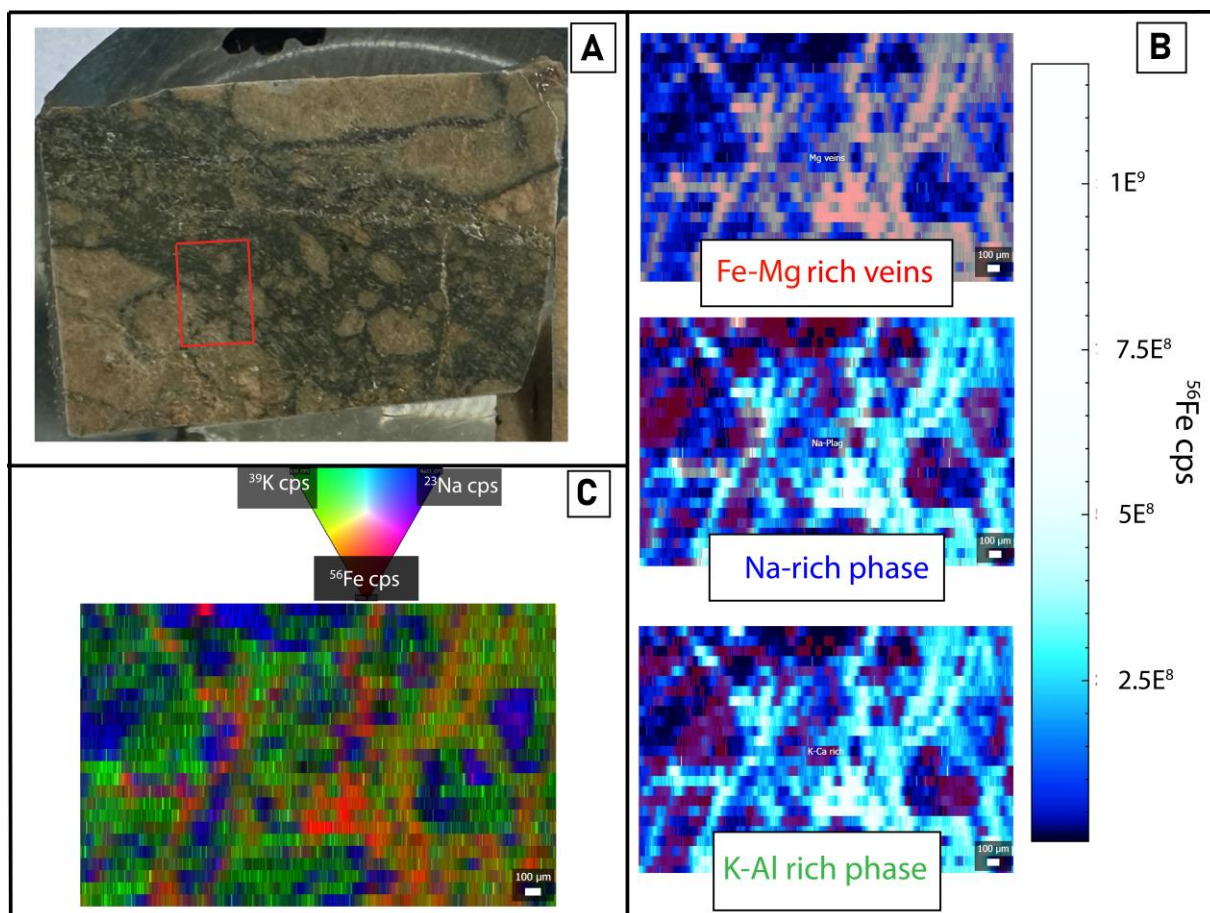
LA-ICP-MS analysis of this sample yielded two distinct domains, visible in Figure 14C and the MLA map for this sample (Figure 5). They show a sediment (top) and fine-grained dyke (bottom) contact. There is a third phase away from the contact, dominated by Mg and Fe, however Rb concentrations are negligible. All phases have been overlaid on an  $^{29}\text{Si}$  map for consistency. Maps for all analysed elements are available in Appendix 7.

The Rb-rich contact (LK-172-Rb) yielded an age of  $426 \pm 78$  Ma ( $2\sigma$  error) with  $^{87}\text{Sr}/^{86}\text{Sr}_{(i)}$  of 0.7169 ( $n=77$ ) (Figure 15) while the Si-rich shale phase (LK-172-Si) yielded an age of  $502 \pm 51$  Ma ( $2\sigma$  error), with  $^{87}\text{Sr}/^{86}\text{Sr}_{(i)}$  of 0.7127 ( $n=77$ ) (Figure 15).



**Figure 15: (LEFT) Isochrons for phase LK-172-Rb (top) and LK-172-Si (bottom) with ages and initial  $^{87}\text{Sr}/^{86}\text{Sr}$  along with associated  $2\sigma$  errors and mean square weighted deviation (MSWD). (RIGHT) ternary map of their pixel regions that each isochron was analysed from. Each isoplot is colour coded to its colour in the ternary map.**

Sample MP02-583



**Figure 16:** A) Sample MP02-583 mounted in epoxy with the red box depicting the mapped region; B) Three distinct pixel maps for phases (Fe-Mg rich veins, Na-rich phase and K-Al Rich phase) present in sample MP02-583 (red regions) overlain on  $^{56}\text{Fe}$  concentration map (left) and  $^{56}\text{Fe}$  scale (right); C) The three distinct phases in B compiled into one ternary diagram showing their respective spatial relationships to each other.

LA-ICP-MS analysis of this sample yielded three distinct domains. The most prevalent in elemental maps is the Fe, Mg-rich phase, appearing as a ‘web’ across the analysed map (Figure 16; B). Two other phases exist which appear to be closely related. The K, Al-rich phase tends to exist as a ‘halo’ separating the Mg phase from the Na-rich phase (Figure 16; B). All phases have been overlain on  $^{56}\text{Fe}$  concentration map. Maps for all analysed elements are available in Appendix 8.



The Fe rich phase (MP02-583-Fe) yielded a minimum age of  $368 \pm 29$  Ma ( $2\sigma$  error) with  $^{87}\text{Sr}/^{86}\text{Sr}_{(i)}$  of 0.7173 ( $n=99$ ) (Figure 17). The Na-rich phase (MP02-583-Na) yielded an age of  $332 \pm 29$  Ma ( $2\sigma$  error) with  $^{87}\text{Sr}/^{86}\text{Sr}_{(i)}$  of 0.7149 ( $n=72$ ) (Figure 17). The K-Al rich phase (MP02-583-K) yielded an age of  $300 \pm 50$  Ma ( $2\sigma$  error) with  $^{87}\text{Sr}/^{86}\text{Sr}_{(i)}$  of 0.7310 ( $n=99$ ) (Figure 17).

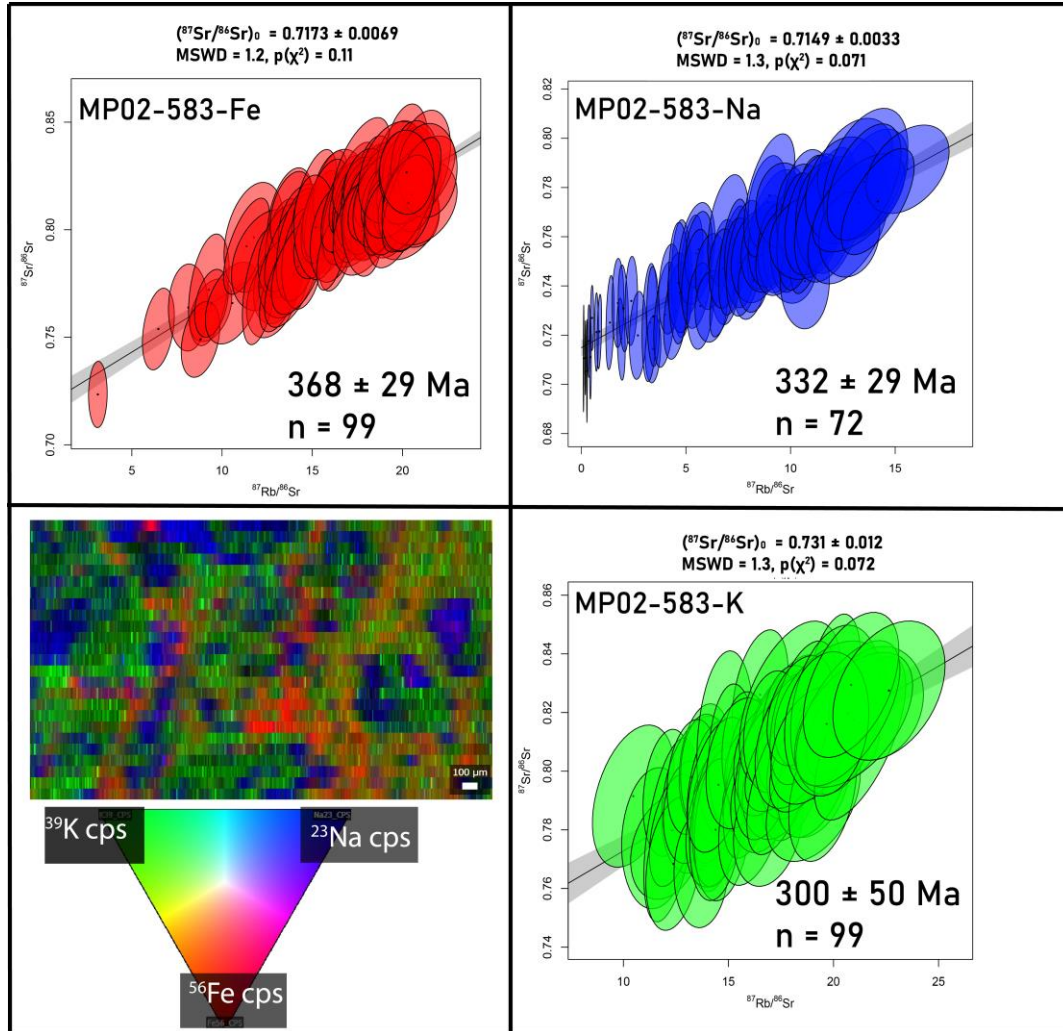


Figure 17: Isochrons for phase MP02-583-Fe (top left), MP02-583-Na (top right) and MP02-583-K (bottom right) with ages and initial  $^{87}\text{Sr}/^{86}\text{Sr}$  along with associated  $2\sigma$  errors ( $2\sigma$  quoted) and mean square weighted deviation (MSWD) and (bottom left) ternary map of their pixel regions which each isochron was analysed from. Each isoplot is colour coded to its colour in the ternary map.

Table 11: Summary of LA-ICP-MS Rb–Sr elemental mapping ages and associated errors along with major elements associated with phases. Analyses in red will not be discussed further as they did not return sufficient radiogenic Rb spread for dating. Dominant elements labelled as per periodic table abbreviation.

Sample ID	Phase ID	Dominant elements	Initial $^{87}\text{Sr}/^{86}\text{Sr}$	+/- ( $2\sigma$ )	Age	+/- ( $2\sigma$ )	MSWD
MP03-493	MP03-493-Li	Li, Mg, Fe, Rb, K, Zr	0.7105	0.0026	505	10	2
MP03-493	MP03-493-Rb	K, Si, Rb	0.7130	0.0022	403	13	1.4
LK-172	LK-172-Rb	Li, Na, Mg, Al, P, Ti, Fe	0.7169	0.0019	426	78	1.6
LK-172	LK-172-Si	Si, Th	0.7127	0.0081	502	51	1.4
MP02-583	MP02-583-Fe	Fe, Mg, Li, Ti	0.7173	0.0069	368	29	1.2
MP02-583	MP02-583-Na	Na, Si	0.7149	0.0033	332	29	1.3
MP02-583	MP02-583-K	K, Si, Rb, Ca	0.731	0.012	300	50	1.3
MP02-556	MP02-556-Si	Si, K, Na, Rb, Eu, Th	0.7160	0.0015	334	14	0.99
MP02-556	MP02-556-Fe	Li, Mg, Al, Fe	0.7096	0.0046	503	611	1.3
LK12-173	LK-173-Si	Si, K, Th	0.7084	0.0073	638	35	1.2
LK12-173	LK-173-Li	Li, Na, Mg, Al, P, Ti, Fe, Y, Zr	0.7137	0.0018	493	92	1.2
MP03-546	MP03-546-K	K, Al, Rb, Sr	0.7086	0.0019	621	533	1.6
MP03-546	MP03-546-Rb	Rb, K	0.749	0.024	212	106	1
MP02-579	MP02-579-Na	Na, K, Rb	0.7137	0.0042	358	33	1.2
MP02-579	MP02-579-Mg	Fe, Li, Mg, Ca, Ti, Fe, Sr, Y, Ce, Eu	0.7092	0.052	387	115	0.98

## LA-ICP-MS U–PB AGES OF RASTER ANALYSED CARBONATE BEDS AND VEINS

Analysis of carbonates present in samples analysed through this method revealed all carbonates contained uranium concentrations lower than 100ppm with the majority containing less than 20ppm. There was also obvious hallmarks of Pb loss as all analysed raster maps returned ages younger than 80 Ma with flat concordia lines (Vervoort, 2018; Rasbury & Cole, 2009). As such, the results of this method will not be further discussed.

## DISCUSSION

### **The rift, drift and end of a passive margin on the Tasman Line.**

Recent full-plate tectonic reconstructions suggest that prior to its positioning on the eastern edge of the Gondwanan continent next to Antarctica, cratonic Australia was a land-locked region of the supercontinent Rodinia (Merdith et al., 2019; 2021; Cao et al., 2024). Some authors suggest that south China (Li et al., 1995; 2023) and/or Tarim (Wen et al., 2017) lay to its east (present coordinates). These reconstructions were demonstrated to be hard to reconcile with Phanerozoic-like plate tectonics by Merdith et al. (2017b), suggesting that earlier models of a tight fit between Australia and Laurentia are more plausible (Figure 18A) (Merdith et al., 2019; 2021; Cao et al., 2024). It is believed that a superplume beneath this portion of Rodinia lead to Australia's eastern margin (the Tasman Line) rifting from North America during the formation of the proto-Pacific Ocean *ca.* 750 Ma (Merdith et al., 2021) (Figure 18B). The rift led to the formation of the continental slope in which the Pualco Tillite and Braemer Ironstone Formations (Mole et al., 2024) were deposited in the LLKB (Figure 18C). These formations underlie the analysed shales in this project.

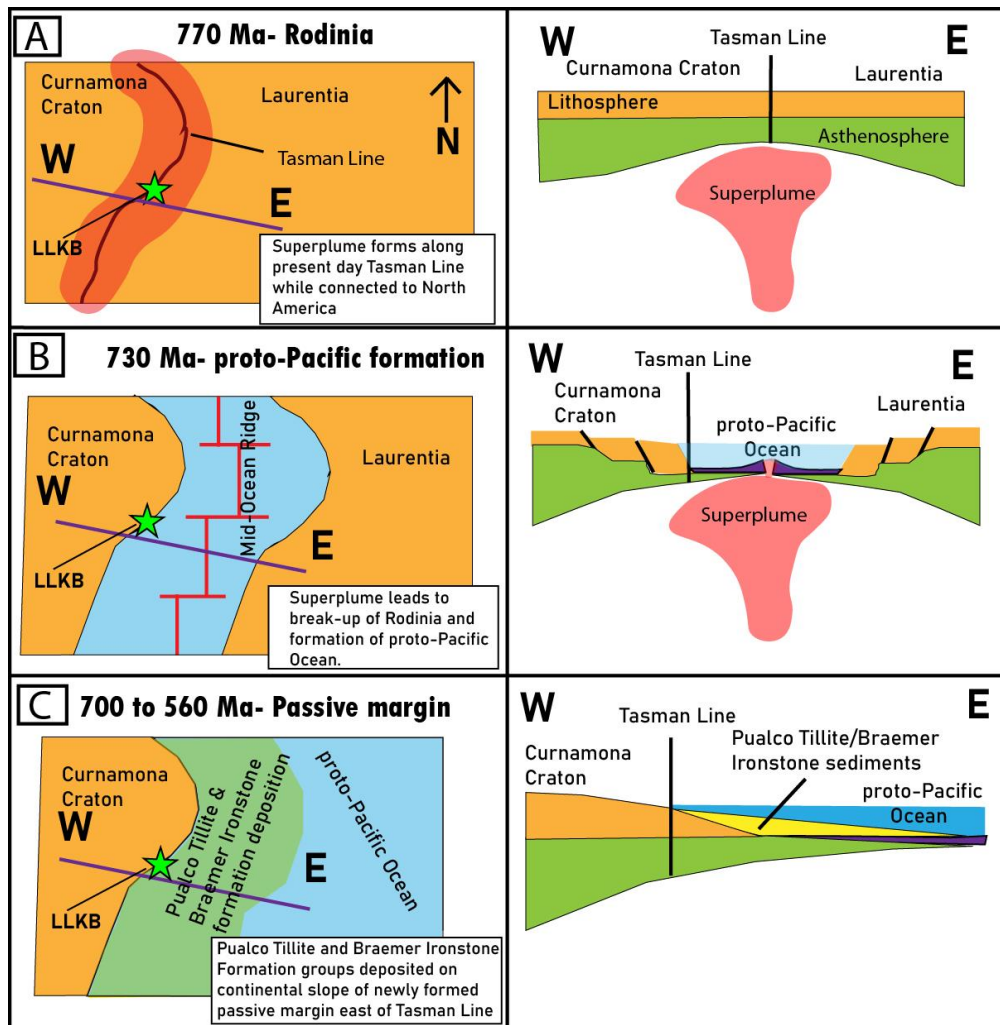


Figure 18: An overview of the evolution of the LLKB region from; (A) the initiation of rifting in Rodinia and (B) subsequent drift from Laurentia to form Gondwana to (C) the deposition of sediments associated with the passive margin prior to subduction initiation (Pualco Tillite and Braemer Ironstone Formation) on the margin. Left image is overhead view and right is a cartoon cross-section from W through E along purple line. The green star represents the westernmost point of the LLKB.

### Back-arc sedimentation in the LLKB

Rb–Sr geochronological analysis of the shale samples within the Torrawangee and Dinggali formations fit within the window between Rodinia break-up and the initiation of the Delamerian Orogeny (*ca.* 514 Ma), returning an oldest age of  $616 \pm 55$  Ma (LK12-186) and youngest of  $533 \pm 39$  Ma (LK11-323) (Figure 11). Due to the significant detrital proportions within the shales, there is some uncertainty if these are detritus ages or shale formation ages. This leads to two potential hypotheses. Firstly, these ages could record authigenic ages of illite formation in-situ and suggest that their formation pre-dates the Delamerian Orogeny,

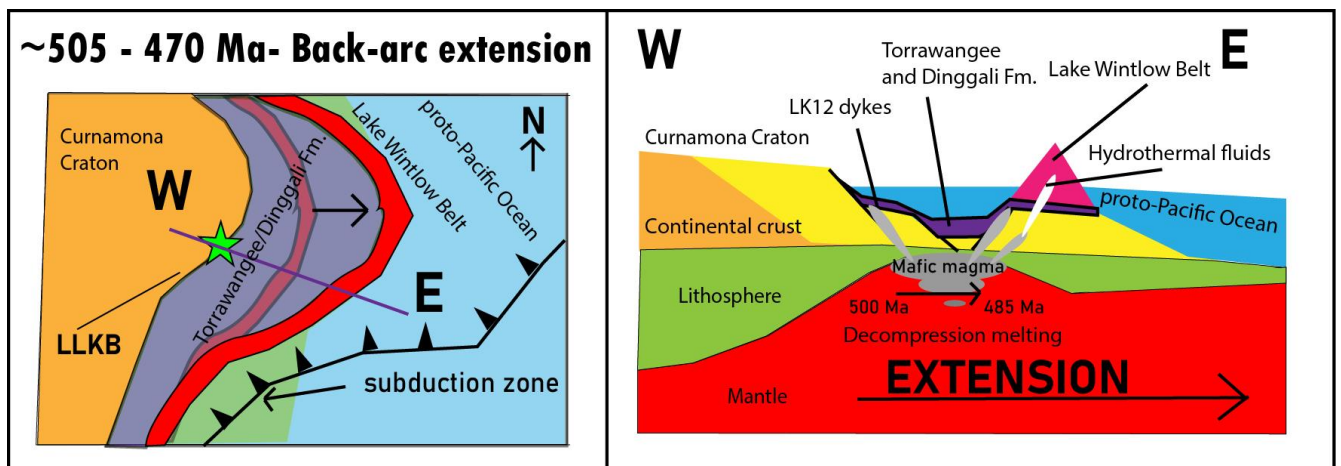
indicating these sediments formed on a static passive margin within the LLKB with no back-arc sedimentation. This seems unlikely as it differs significantly from the proximal AFB Kanmantoo sequences in the South Australian portion of the Delamerian Orogen. Foden et al. (2020) interprets the Kanmantoo sequence to be rapidly deposited sedimentary rocks formed in a deepening basin behind the Staveland arc associated with subduction rollback and terminating at *ca.* 490 Ma, significantly younger than our interpreted ages. Consequently, a more likely explanation is favoured here. The high Sr(i) values of greater than 0.71 (Table 10) and the morphology of the shales themselves being quite heterogeneous and containing significant proportions of silt-sized grains (Appendix 2), indicates the analysed ages are likely detrital. Therefore, they should be viewed as maximum depositional ages, dating the original sediment prior to its erosion and re-deposition on the LLKB passive margin. This hypothesis gains traction when discussing the isochron of the oldest sample (LK12-186) (Figure 11). The spots analysed return a wide range of Rb–Sr ratios (evidenced by the removal of 17 spots to make a coherent isochron) (Appendix 15), reflecting this heterogeneous source of detritus in the sample. This spread may reflect a mixed source in the sample, detrital grains from a Neoproterozoic source with some Ediacaran–Cambrian aged grains. This would explain why an isochron and therefore valid age was hard to define for this sample.

The remaining shale analyses (Figure 11) return more coherent isochrons and ages within error of each other *ca.* 572–540 Ma (Figure 11). If we take the same approach, that they depict detrital ages, we can see they compare favourably to the detrital zircon record for Kanmantoo sediments. There is an abrupt change at the base of the Kanmantoo group in the provenance of zircons from Mesoproterozoic aged to a dominantly Cambrian–Ediacaran population of ages ranging from 600–500 Ma (Haines et al., 2009; Brotodewo et al., 2021;



Ireland et al., 1998). A potential source is the Ross Orogen along the Antarctic Gondwanan margin, containing a newly formed volcanic complex *ca.* 560 Ma (Boger & Miller, 2004).

The findings of this paper indicate the Torrawangee and Dinggali formations north-west of the Lake Wintlow Belt (hereafter referred to as LWB) in the LLKB are likely Kanmantoo equivalents. Therefore, they were deposited in a deepening basin as subduction initiated along the margin. These sediments likely initially formed co-eval with the hypothesised newly forming volcanic arc (LWB) and then continued being deposited in the back-arc to the west as the subduction zone rolled back to the east (Figure 19) prior to the collision of VanDieland with the margin (Huston et al., 2015; Gray et al., 2024). Detrital zircon SHRIMP U–Pb analysis of zircons within these samples should be undertaken to gain more robust ages, adding further weight to this hypothesis.

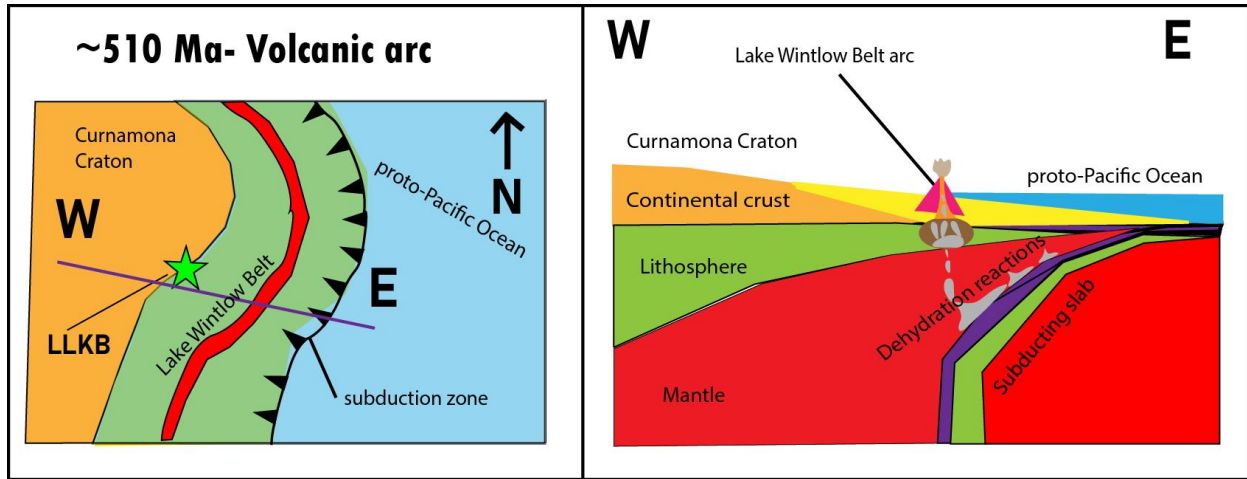


**Figure 19: A cartoon cross-section of back-arc sedimentation of the Torrawangee and Dinggali Formations in the back-arc behind the Lake Wintlow Belt during extension in the LLKB. The red linear shapes in the left image depict the initial Lake Wintlow belt location and its evolution from 505 Ma to 470 Ma. The left image is an overhead view and right is a cartoon cross-section from W through E along the purple line. The green star represents the westernmost point of the LLKB.**

### An arc in the Loch Lilly-Kars Belt

Rb–Sr spot and map analyses of igneous samples suggest that the Stavely Arc and Mt Wright Volcanic belt, interpreted by Foden et al. (2020) and Crawford et al. (1997), as the volcanic

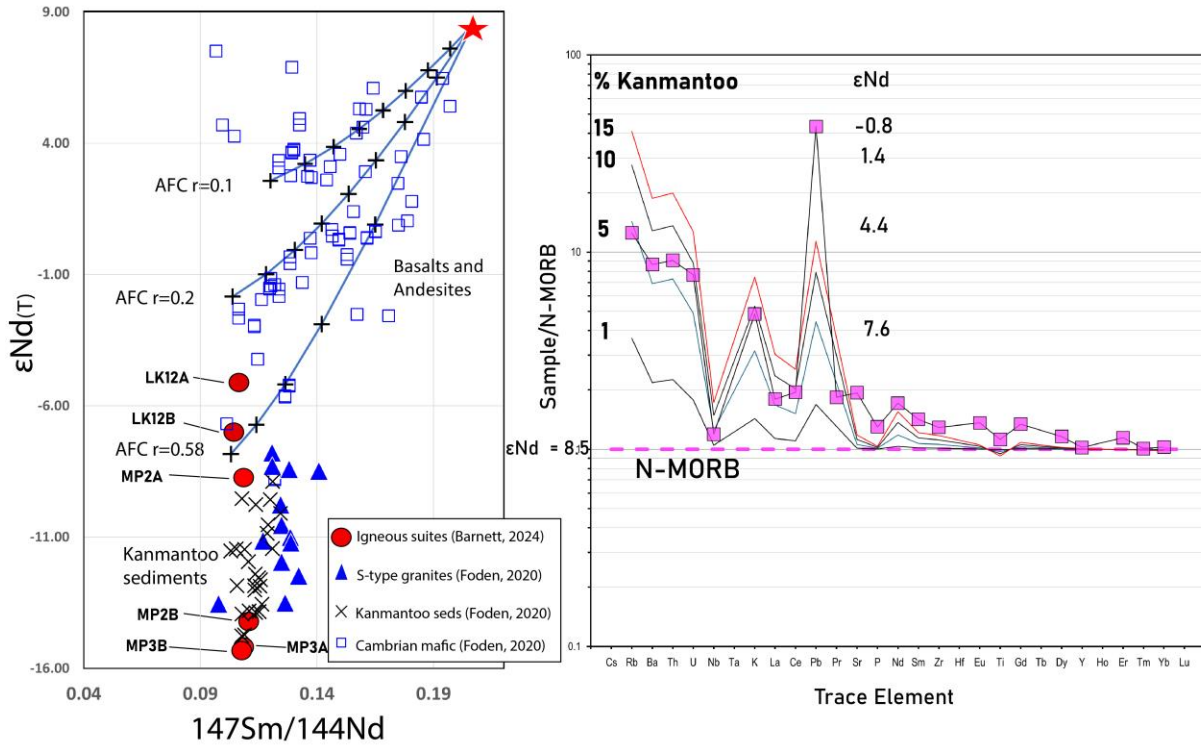
arc associated with the onset of subduction along the Gondwana margin, were indeed connected as one system through the LLKB region (Figure 20). Spot analysis of plutonic sample MP03-548 yielded an age of  $510 \pm 12$  Ma (Figure 10) while map analysis of the MP03-493-Li phase returned an age of  $505 \pm 10$  Ma (Figure 13). These both come from drillhole NDIWMP03 within the LWB and the ages fit comfortably within error of published values for S-type granites found within the Stavely Arc and Mount Wright volcanic sequences at 515–505 Ma (Foden et al., 2020). Furthermore, the geochemical analyses of these samples (MP3A and MP3B) contain the hallmarks of S-type suites with significant enrichment in incompatible elements Rb, Th and U, along with large LREE slopes (Figure 8) and significant Eu/Eu\* (0.61 and 0.58) (Table 7). Ce and Ba are also enriched, likely due to their elevated concentration in seawater which imparts its signature in arc intrusions during its release into the mantle wedge through the process of retrograde metamorphism during subduction (Villaros et al., 2009). It is suggested that, while the MP02 samples do not return an equivalent age, due to their proximity, they were initially intruded in the same arc setting. This hypothesis is validated by their similar enrichment in incompatible elements (Figure 8) and Eu/Eu\* anomaly values (0.48 and 0.53) (Table 7). Recent ages reported by GA support this hypothesis with granodiorites taken from the same hole (NDIWMP02) returning U–Pb SHRIMP zircon ages ranging from 510 to 500 Ma (Mole et al., 2024). These findings indicate the volcanic arc sat in the LWB region from 510 to 500 Ma (Figure 20). We propose that subsequent hydrothermal activity, in a manner similar to that reported by Hong et al. (2023) from the Anabama region along strike to the west has led to their alteration and younger analysed ages, which will be expanded upon later.



**Figure 20:** An overview of the LLKB region during the formation of the Lake Wintlow Belt arc and its placement on top of the Torrawangee and Dinggali Formations after subduction of the proto-Pacific Ocean initiated along the Gondwanan eastern margin. The left image is an overhead view and the right is a cartoon cross-section from W through E along purple line. The green star represents the westernmost point of the LLKB.

Evidence for these *ca.* 500 Ma intrusions has been missed in previous work because the LLKB has a significant post-formation tectonic history leading to extensive alteration. There is evidence within all igneous samples in this project, including the prevalent hematite staining of quartz in samples MP3A and MP3B, extensive late carbonate veining in our LK mafic dykes and complete recrystallisation of some arc protoliths seen in sample MP2A (Figure 4). The new mapping technique for Rb/Sr systems used here allows separate phases to be isolated and dated independently in the one sample and is key to finding the phases which are robust enough to maintain their chemistry throughout later events. A prime example being the Li-rich mineral phase within sample MP03-493, which returns the age of the arc intrusion ( $505 \pm 10$  Ma) while the finer-grained Rb-rich infill does not ( $403 \pm 13$  Ma) (Figure 13).

The tectonic setting of this arc in the LLKB region is interpreted to be continental and not oceanic due to the negative  $\epsilon\text{Nd}(t)$  values of the arc-related granites which become more negative with increasing assimilation of crustal material in the melt (Stevenson et al., 1999).



**Figure 21: LEFT-** Scatterplot of  $\epsilon_{Nd(t)}$  vs  $^{147}Sm/^{144}Nd$  of igneous samples analysed in this project (red circles) along with S-type granites, Cambrian mafic volcanics and Kanmantoo sedimentary rocks from The Delamerian Orogen (Foden et al., 2020) along with evolution lines of these samples based on specific assimilation fractional crystallisation (AFC) values. **RIGHT-** Spiderplot depicting the change in concentration of trace elements in igneous samples found in the AFB (Foden et al., 2020) compared to N-MORB values depending on the percentage of assimilated Kanmantoo sedimentary rocks in the melt and their equivalent  $\epsilon_{Nd(t)}$  values. After Foden et al. (2020).

If we consider the Kanmantoo Group of the AFB a proxy for possible sediment assimilation in the magma (Foden et al., 2020) due to their similar provenance and regional proximity to the LLKB sedimentary rocks as discussed above, it is viable to model the MP S-type granite chemistry. The highly evolved  $\epsilon_{Nd(t)}$  values of the MP samples suggest they assimilated considerable proportions of sediment deposited in the deepening basin associated with subduction onset. This assimilation of Kanmantoo Group equivalents would lead to increasing concentrations of elements such as Cs, Rb, Ba, Th and Pb as seen in S-type intrusives in the AFB (Foden et al., 2020) (Figure 21). The MP2 and MP3 granites and granodiorites are defined by significant enrichment in these elements (Figure 8).

Furthermore, an S-type granite of an oceanic arc tends to return an  $\epsilon_{Nd(t)}$  value of + 0.1 to +

1.7 (Whalen et al., 2003). In contrast, the early LLKB arc granite samples analysed here plot with a chemistry much closer to mean Kanmantoo sediment values than ‘oceanic’ S-type granites at a more evolved value (greater than  $-13 \text{ } \epsilon\text{Nd(t)}$ ) (Figure 21). This suggests an assimilation fractional crystallisation value for the arc of greater than 0.58 and indicates the largest impact on their geochemical signature is assimilation and not fractional crystallisation. These findings clearly indicate the arc in the LLKB was formed on continental crust initially, a view favoured in previous work (Cayley, 2011; Greenfield et al., 2011) (Figure 20).

### **From arc to back-arc**

The proto-Pacific subduction zone has been characterised by an eastward migration of the trench and short pulses of orogenesis as microcontinents that rifted off during the breakup of Rodinia collided with the margin (Glen & Cooper, 2021; Huston et al., 2015; Moresi, 2014). During rollback, the region on the upper plate in extension moves in the same direction as roll-back over time, resulting in regions that were initially part of the arc moving into the back-arc and extending. A present-day example of this phenomenon is the Taupo Volcanic Zone in New Zealand where there is evidence for prior arc magma emplacement in regions where current extensional collapse and high geothermal gradients are occurring due to slab retreat (Harrison & White, 2006). We propose a similar process occurring in the LLKB on the proto-Pacific margin. Previous work by Hong et al. (2024) suggested a second phase of igneous activity, occurring immediately after the Delamerian Orogeny at *ca.* 490 Ma. The results of this paper further support this hypothesis with spot analyses of samples MP03-493 (MP3A) and MP02-556 (MP2A) returning ages of  $484 \pm 20 \text{ Ma}$  and  $435 \pm 56 \text{ Ma}$ , respectively (Figure 10). Both samples contain evidence for pervasive albitic alteration, particularly MP2A. This is based on thin section analysis of this sample, where coarse relict plagioclase and hornblende (Figure 4) indicate its original composition was that of a

granodiorite with similar composition to MP3B (Table 6). This altered sample plots with a much less evolved  $\epsilon\text{Nd}(t)$  (-8.7) than the other granite samples in the LWB and returns this younger age. We argue that the low reset temperature of the Rb/Sr system due to hydrothermal fluids at as low as 120°C (Subarkah et al., 2022) means that the resulting age dates recrystallisation due to alteration (*ca.* 484 Ma) and not the formation age of the arc-protoliths discussed above. These fluids could have remobilised the incompatible REEs and led to the fluid-assisted recrystallisation of these samples with an influx of Nd leading to a more juvenile  $\epsilon\text{Nd}(t)$  signature. Supporting this hypothesis is the higher concentration of HREE elements in our MP2A and MP2B samples when compared to MP3 samples (Figure 8). We propose this more juvenile fluid source brought more HREEs into the system and explains this discrepancy between the two suites. Therefore, the  $\epsilon\text{Nd}(t)$  being less evolved at this younger age suggests the fluids appear to be sourced, at least in part, from a more juvenile magma than the initial arc magmas prior to *ca.* 500 Ma (Figure 19). We propose that when the Stavelly region of the Delamerian was closing due to the collision of VanDieland from the south-west leading to the cessation of Kanmantoo deposition *ca.* 490 Ma (Foden et al., 2020), the LLKB region to the north was rolling back rapidly, similar to that proposed by Moresi et al. (2014). This led to the oroclinal bend preserved in the Delamerian Orogen today. This extension facilitated decompression melting in the LLKB and led to the formation of the Tarrara-Menindee Trough as a basin formed behind the retreating arc. This structure is seen today as the low gravity, high magnetic corridor directly north-west of the LWB (Figure 22). Further analysis of the Tarrara-Menindee Trough sedimentary rocks to the south of drillhole NDILLK14 should be undertaken attempting to intercept shales younger than 490 Ma to confirm the theory as recent drilling in 2023 did not intercept shales within this structural corridor.



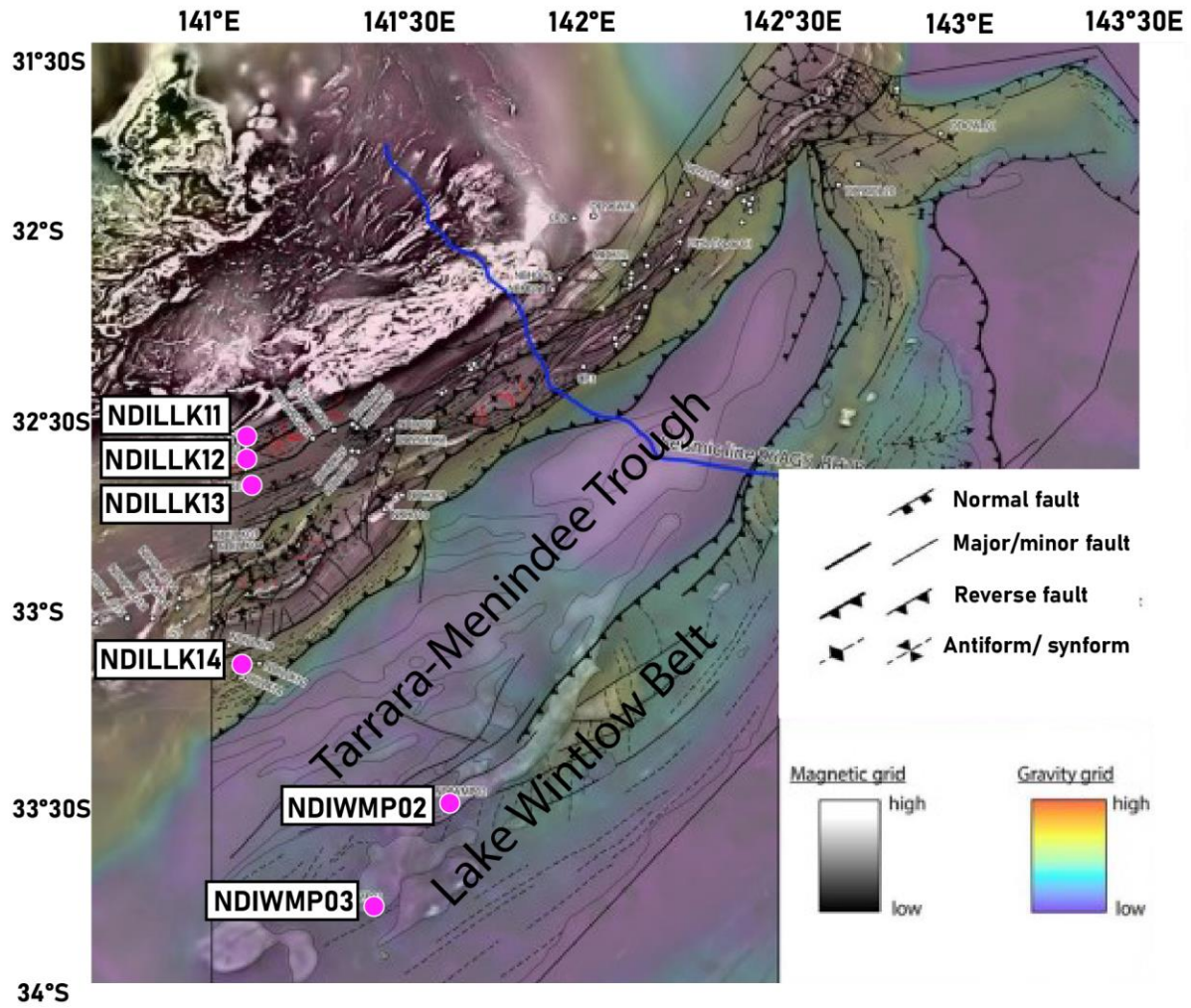


Figure 22: Linework of solid geology map of Loch Lilly-Kars and Lake Wintlow Belts, New South Wales. The drillholes used in this project are highlighted as pink dots. Background is a coloured semi-transparent Bouguer gravity anomaly grid (Lane et al., 2019) above greyscale 0.5 vertical derivative of aeromagnetic data reduced to the pole (Poudjom Djomani et al., 2019). Blue line is seismic line 96AGS\_BH1B from Korsch et al. (2006). After (Clark et al., 2024).

### The mafic olivine basalt dykes of LLKB

It is interpreted that the extension discussed above, is also responsible for the olivine basalt dykes, samples LK12A and LK12B present in drillhole NDILLK12. These dykes are dominated by compatible elements including Mg, Ti, Co and Ni (Table 8). The last two of these of particular note being at least 10x more concentrated than our LWB diorites of S-type character (Table 8). While it could be argued that their increased concentrations at up to 80x C1 values (Figure 8) of incompatible elements like Pb and U suggests an S-type character, it is important to note that this region has just undergone subduction initiation, likely resulting

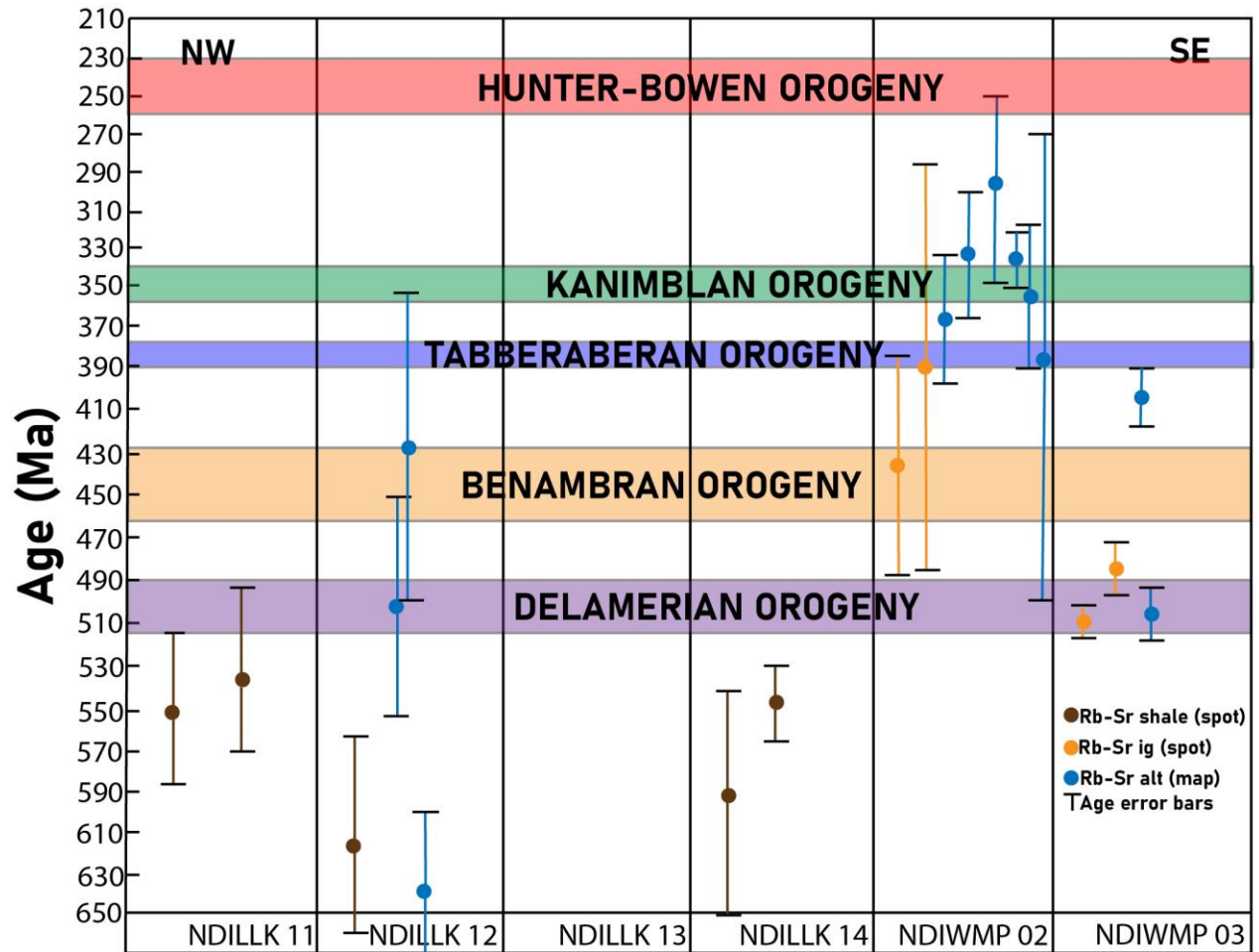
in the underplating of subduction influenced magmas to the mantle here. We argue that the remelting of these from decompression and mixing with the juvenile source would impart that ‘S-type’ signature on these back-arc intrusions.

The dykes have trace element profiles closer to C1 chondrite values than those of the LWB rocks (Figure 8), and smaller europium anomalies (0.86 and 0.8) (Table 7) indicating decreased magma fractionation at the time of crystallisation. Sm–Nd analysis also returned less evolved  $\epsilon\text{Nd}(t)$  values of -7 and -5 (Table 9), suggesting that they did not form in the same setting as our interpreted arc suites. Due to their more mafic composition, they contain less Rb and as such do not return robust ages. This is further complicated by the presence of significant carbonate veining throughout (Figure 4; Appendix 3), which could have remobilised incompatible elements including Rb leading to its depletion, reflected by the high errors in their determined ages of  $426 \pm 78$  Ma (LK-172-Rb) (Figure 15) and  $493 \pm 92$  Ma (LK-173-Li) (Table 11; Appendix 10). They intrude Torrawangee Group rocks with ages younger than 560 Ma and so cannot be connected to the prior rifting of Laurentia. This same dyke was recently dated by GA using SHRIMP U–Pb zircon dating returning an age of  $499 \pm 5.8$  Ma (Mole et al., 2024). This intrusion is likely driven by continuous decompression melting in the back-arc (Figure 19) during extension *ca.* 500 Ma and this back-arc system likely migrated eastward to sit in the LWB *ca.* 485 Ma (Fig. 19) as discussed above, evidenced by the  $\epsilon\text{Nd}(t)$  values and Rb–Sr geochronology found in samples MP2B and MP03-493, respectively (Figure 9 and Figure 10). The movement of this back-arc system, linked directly to the eastward migration of the subduction zone is therefore the likely cause of the pervasive hydrothermal fluids responsible for the albitic alteration of hydrothermal breccia MP2A (Figure 4)). This extensional period is interpreted to conclude with the collision of the Macquarie Arc with the subduction zone (Moresi et al., 2014; Foden et al.,



2020) and subsequent jumping of the subduction zone eastward behind this newly accreted microcontinental block in the Ordovician. We propose this collisional event re-activated the normal fault south of drillhole NDILLK14 (Figure 22) into a thrust fault.

### Post active margin events in the Loch Lilly-Kars Belt



**Figure 23: Time space plot showing the Rb–Sr ages and associated errors of analysed samples in this project sorted by their drill-hole location. Holes are plotted from most northwest (left) to most southeast (right). The estimated timing of orogenic events during Tasmanide formation have been taken from Foden et al. 2020 and plotted as coloured bars.**

There is extensive evidence in the rocks of the LLKB that this region did not become inactive after the subduction zone jumped outboard of the Macquarie Arc in the Ordovician. The igneous suites present in the LWB are dominated by albitic alteration, brecciation and subsequent epidote + chlorite growth (Figure 4; Appendix 2). Most notably the samples from

drillhole NDIWMP02 (Appendix 2). Rb–Sr laser-map analysis has helped to separate these different events. There is evidence for hydrothermal fluid circulation post the Delamerian Orogeny until as young as 250 Ma, in sample MP02-583-K (Table 11). While the LLKB was no longer at the boundary of an active margin after 470 Ma, the Tasmanides continued their formation further east. The LLKB at this stage was still a new accretionary orogen on the boundary of cratonic Australia and the crustal scale faults in the region could very easily be re-activated by forces from the margin. We suggest here that these later alteration events occurred shortly after contractional events in the Tasmanides, when the extensional regime restarted, facilitating higher fluid flow along structural corridors and increased geothermal gradients in the LLKB. This hypothesis supports the findings from our U–Pb carbonate dating. The significant Pb-loss and low uranium concentrations indicate that these fluids were likely oxidising in nature and active within the vast majority of the LLKB. Oxidising fluids are efficient at stripping both uranium and lead from the rocks they permeate through (Cabral Pinto et al., 2018), leading to low uranium concentrations and U–Pb ages of younger than 100 Ma with horizontal concordia lines, both of which occur in all carbonate samples analysed. Ages obtained from Rb–Sr alteration mapping indicate numerous alteration periods, including a 420–390 Ma event, seen in MP03-493-Rb (Table 11) from drillhole NDIWMP03 (Figure 23), post-dating the Benambran Orogeny (460–430 Ma), but pre-dating the Tabberaberan Orogeny (390–380 Ma). This sample supports the hypothesis that extension is responsible for at least this alteration event. While the younger phases in NDIWMP02 return age errors too broad to determine if they occur during the orogenic or extensional events (Table 11; Figure 23), they do show clear evidence that hydrothermal activity continued regionally until the Hunter-Bowen Orogeny which initiated *ca.* 260 Ma.

## CONCLUSIONS

- Rb–Sr spot analysis of igneous suites in the Lake Wintlow Belt indicate an active volcanic arc existed in the LLKB from *ca.* 510–500 Ma and is co-genetic with the Stavely Zone arc suites, implying it was continuous from the Stavely Zone to the Koonenberry Belt.
- Highly evolved  $\epsilon\text{Nd}(t)$  values (down to -13) and trace element abundance patterns of these intrusions indicate the volcanic arc formed on continental crust and suggests the dominant control on their chemistry was assimilation of ‘Kanmantoo-like’ sediments as opposed to fractional crystallization.
- Olivine basalt dykes found in NDILLK12 north of the Tarrara-Menindee Trough may be the result of back-arc extension and melting of underplated igneous rocks *ca.* 500 Ma before moving eastward to the Lake Wintlow Belt.
- Hydrothermal alteration of Lake Wintlow Belt arc protoliths by more juvenile hydrothermal fluids led to the reset of some Rb–Sr ages within arc suite samples *ca.* 490–470 Ma and remobilized REE elements, in particular HREEs and is believed to have reset the Sm–Nd system of sample MP02-556.
- Rb–Sr dating of shales from north-west of the Lake Wintlow Belt indicate they are dominantly derived from Cambrian-Ediacaran sediments, likely sourced from the Ross Orogen *ca.* 560 Ma and equivalent to Kanmantoo group rocks of the AFB, indicating a period of back-arc sedimentation in the LLKB from its formation *ca.* 514 Ma.
- There is evidence of hydrothermal alteration by oxidic fluids throughout the LLKB spanning from 500 Ma until 250 Ma, influenced by tectonic activity on the eastward migrating subduction system.

- The LLKB preserves evidence of a subduction orogenic tectonic system with an eastward migration, very similar to the Stavely/AFB region to its south.

## **ACKNOWLEDGMENTS**

I am endlessly thankful for the unwavering support and patience of my supervising team of Alan Collins, Morgan Blades and Darwinaji Subarkah who have given me so much guidance and feedback along with Chris Lewis and the extended team at Geoscience Australia for access to the datasets and samples this project analysed. Thanks also to the MinEx CRC who drilled the samples and whose umbrella this project sits. Further thanks to the extended Tectonics and Earth Systems group for being so welcoming this year. Sarah Gilbert, Paul Olin and Nobuyuki Kawashima are thanked for their technical expertise during my analyses at Adelaide Microscopy while Simon Heinrich and Robert Klæbe must be thanked for their patience in the MASS labs along with Ricky Williams for the training received in the lapidary. I would also like to thank Peak Iron Mines and The Playford Trust for their financial support. Finally endless thanks to fellow honours students Isaac Pepe, Cooper Ferguson, Kate Wilson Jayden Squire, Nicko Wyndham & Ruoheng Li for the support and friendships that have grown throughout this year.

## REFERENCES

- ABDULLAH, R. & ROSENBAUM, G. 2018. Devonian crustal stretching in the northern Tasmanides (Australia) and implications for oroclinal bending. *Journal of Geophysical Research: Solid Earth* **123**, 7108-7125.  
<https://doi.org/10.1029/2018JB015724>
- AN, Y., LI, S., ZHU, D., CAWOOD, P. A., WANG, Q., XIE, J., ZHANG, L. & ZHAO, Z. 2024. Compositional change from high-Mg to low-Mg magmatism at ca. 150 Ma in the central Lhasa terrane, Tibet: Switching from advancing to retreating subduction of the Bangong Tethyan slab. *The Geological Society of America* **136**(1/2), 689-706.  
<https://doi.org/10.1130/B36719.1>
- ANDERS, E. & GREVESSE, N. 1989. Abundances of the elements: Meteoritic and solar. *Geochimica et Cosmochimica Acta* **53**, 197-214.  
[https://doi.org/10.1016/0016-7037\(89\)90286-X](https://doi.org/10.1016/0016-7037(89)90286-X)
- BAATAR, B., PARRA-AVILA, L.A., FIORENTINI, M. L., POLITO, P. & CRAWFORD, A.J. 2020. Porphyry Cu fertility of the Loch Lilly-Kars Belt, Western New South Wales, Australia. *Australian Journal of Earth Sciences* **67**(1), 75-87.  
<https://doi.org/10.1080/08120099.2019.1637937>
- BAILEY, A., BASTRAKOV, E., CAIRNS, C., CAYLEY, R., DUNCAN, R., HUSTON, D., LEWIS, C., MCALPINE, S., SCHOFIELD, A., SKLADIZEN, P., TAYLOR, D. & THOMAS M. 2018. Regional geology and mineral systems of the Stavely Arc, western Victoria: Data release 5 – Geochemistry data. A. Schofield, *GeoScience Australia*.  
<http://dx.doi.org/10.11636/Record.2017.002>
- BOGER, S. D. & MILLER, J. M. 2004. Terminal suturing of Gondwana and the onset of the Ross-Delamerian Orogeny: the cause and effect of an Early Cambrian reconfiguration of plate motions. *Earth and Planetary Science Letters* **219**(1-2), 35-48.  
[https://doi.org/10.1016/S0012-821X\(03\)00692-7](https://doi.org/10.1016/S0012-821X(03)00692-7)
- BROTODEWO, A., WISE, T. & LLOYD, J. C. 2021. LA-ICP-MS detrital zircon geochronology from the Delamerian Orogen. *MinEx CRC Report 2021/69*.
- CABRAL PINTO, M. M. S., SILVA, M. M. V. G., NEIVA, A. M. R., GUIMARÃES, F & SILVA, P. B. 2018. Release, Migration, Sorption and (Re)Precipitation of U during Peraluminous Granite Alteration under Oxidizing Conditions in Central Portugal. *Geosciences* **8**(3), 95.  
<https://doi.org/10.3390/geosciences8030095>
- CAO, X., COLLINS, A. S., PISAREVSKY, S., FLAMENT, N., LI, S., HASTEROK, D. & MÜLLER, R. D. 2024. Earth's tectonic and plate boundary evolution over 1.8 billion years. *Geoscience Frontiers* **15**(6), 101922.  
<https://doi.org/10.1016/j.gsf.2024.101922>
- CAWOOD, P. 2005. Terra Australis Orogen: Rodinia breakup and development of the Pacific and Iapetus margins of Gondwana during the Neoproterozoic and Paleozoic. *Earth-Science Reviews* **69**(3-4), 249-279.  
<https://doi.org/10.1016/j.earscirev.2004.09.001>
- CAWOOD, P. A., KRÖNER, A., COLLINS, W. J., KUSKY, T. M., MOONEY, W. D. & WINDLEY, B. F. 2009. Accretionary orogens through Earth history. *Geological Society, London, Special Publications* **318**, 1-36.  
<https://doi.org/10.1144/SP318.1>
- CAYLEY, R. A. 2011. Exotic crustal block accretion to the eastern Gondwanaland margin in the Late-Cambrian-Tasmania, the Selwyn Block, and implications for the Cambrian–Silurian evolution of Ross, Delamerian and Lachlan orogens. *Gondwana Research* **19**, 628-649.  
<https://doi.org/10.1016/j.gr.2010.11.013>
- CHAPMAN, J. B., SHEILDS, J. E., DUCEA, M. N., PATERSON, S. R., ATTIA, S. & ARDILL, K. E. 2021. The causes of continental arc flare ups and drivers of episodic magmatic activity in Cordilleran orogenic systems. *Lithos* **398-399**.  
<https://doi.org/10.1016/j.lithos.2021.106307>
- CHEN, N., MAO, J., ZHANG, Z., DUAN, Z., SANTOS, A. & LI, H. 2023. Arc magmatic evolution and Porphyry copper deposit formation under compressional regime: A geochemical perspective From Toquepala arc in Southern Peru. *Earth-Science Reviews* **220**, 104383.  
<https://doi.org/10.1016/j.earscirev.2023.104383>
- CLARK, A. D., PITT, L., DOUBLIER, M. P., HIGHET, L., MOLE, D. R., TAYLOR, H., WISE, T., GILMORE, P. J., HARTNADY, M., KIRKLAND, C. L., BARELUVA, O., LEWIS, C. J., THOMAS, M., FOLKES, C., COLQUHOUN, G. P., CHENG, Y., ROACH, I. C. & BUDD, A. 2024. Basement

- geology of the Loch Lilly-Kars Belt, Lake Wintlow Belt and Wilcannia High. Accompanying notes. Geoscience Australia, Canberra.  
<https://dx.doi.org/10.26186/149762>
- CRAWFORD, A. J., STEVENS, B. & FANNING, M. 1997. Geochemistry and tectonic setting of some Neoproterozoic and early Cambrian volcanics in western New South Wales. *Australian Journal of Earth Sciences* **44**(6), 831-852.  
<https://doi.org/10.1080/08120099708728358>
- CRAWFORD, A. J., COOKE, D. R. & FANNING, C. M. 2007. Geochemistry and age of magmatic rocks in the unexposed Narromine, Cowal and Fairholme Igneous Complexes in the Ordovician Macquarie Arc, New South Wales. *Australian Journal of Earth Sciences* **54**(2-3), 243-271.  
<https://doi.org/10.1080/08120090701221714>
- DROST, K., CHEW, D., PETRUS, J. A., SCHOLZE, F., WOODHEAD, J. D., SCHNEIDER, J. W. & HARPER, D. A. T. 2018. An Image Mapping Approach to U-Pb LA-ICP-MS Carbonate dating and Applications to Direct Dating of Carbonate Sedimentation. *Geochemistry, Geophysics, Geosystems* **19**(12), 4631-4648.  
<https://doi.org/10.1029/2018GC007850>
- DUTCH, R. A. & HAND, M. 2009. Retention of the Sm-Nd isotopic ages in garnets subjected to high-grade thermal reworking: Implications for diffusion rates of major and rare earth elements and the Sm-Nd closure temperature in garnet. *Contributions to Mineralogy and Petrology* **159**(1), 93-112  
<https://doi.org/10.1007/s00410-009-0418-1>
- FLANAGAN, F.J. 1976. Description and analyses of eight new USGS rock standards. *USGS Professional Paper*. **840**, 1-192.  
<https://doi.org/10.3133/pp840>
- FODEN, J., ELBURG, M. A., DOUGHERTY-PAGE, J. & BURTT, A. 2006. The Timing and Duration Of the Delamerian Orogeny: Correlations with the Ross Orogen and Implications for Gondwana assembly. *The Journal of Geology* **114**(2), 189-210.  
<https://doi.org/10.1086/499570>
- FODEN, J., ELBURG, M. A., TURNER, S., CLARK, C., BLADES, M. L., COX, G., COLLINS, A.S., WOLFF, K. & GEORGE, C. 2020. Cambro-Ordovician magmatism in the Delamerian orogeny: Implications for tectonic development of the southern Gondwanan margin. *Gondwana Research*, **81**: 490-521.  
<https://doi.org/10.1016/j.gr.2019.12.006>
- FODEN, J., MAWBY, J., KELLEY, S., TURNER, S. & BRUCE, D. 1995. Metamorphic events in the eastern Arunta Inlier, Part 2. Nd-Sr-Ar isotopic constraints. *Precambrian Research* **71**, 207-227.  
[https://doi.org/10.1016/0301-9268\(94\)00062-V](https://doi.org/10.1016/0301-9268(94)00062-V)
- FOSTER, D. A. & GRAY, D.R. 2000. Evolution and Structure of the Lachlan Fold Belt (Orogen) of Eastern Australia. *Annual Review of Earth and Planetary Sciences* **28**, 47-80.  
<https://doi.org/10.1146/annurev.earth.28.1.47>
- GLEN, R. A. & COOPER R. A. 2021. Evolution of the East Gondwana convergent margin in Antarctica, southern Australia and New Zealand from the Neoproterozoic to latest Devonian. *Earth-Science Reviews* **220**  
<https://doi.org/10.1016/j.earscirev.2021.103687>
- GLORIE, S., GILBERT, S.E., HAND, M. & LLOYD, J.C., 2024. Calibration methods for laser ablation Rb-Sr geochronology: comparisons and recommendation based on NIST glass and natural reference materials. *GChron* **6**, 21-36.  
<https://doi.org/10.5194/gchron-6-21-2024>
- GOROJOVSKY, L. & ALARD, O. 2020. Optimisation of laser and mass spectrometer parameters for the in situ analysis of Rb/Sr ratios by LA-ICP-MS/MS. *Journal of Analytical Atomic Spectrometry* **35**(10), 2322-2336.  
<https://doi.org/10.1039/d0ja00308e>
- GRAY, D. R. & FOSTER, D. A. 2004. Tectonic evolution of the Lachlan Orogen, southeast Australia: Historical review, data synthesis and modern perspectives. *Australian Journal of Earth Sciences* **51**(6), 773-817.  
<https://doi.org/10.1111/j.1400-0952.2004.01092.x>
- GRAY, D. R., VICARY, M. J. & MCNEILL, A. W. 2024. The Tasmanian Tyennan Domain- a structural synthesis and review with tectonic and dynamic implications for continental margin subduction and exhumation. *Australian Journal of Earth Sciences* **71**(2), 153-210.  
<https://doi.org/10.1080/08120099.2023.2280604>
- GREENFIELD, J. E., MUSGRAVE, R. J., BRUCE, M. C., GILMORE, P. J. & MILLS, K. J. 2011. The

- Mount Wright Arc: A Cambrian subduction system developed on the continental margin of East Gondwana, Koonenberry Belt, eastern Australia. *Gondwana Research* **19**, 650-669.  
<https://doi.org/10.1016/j.gr.2010.11.017>
- GUILLONG, M., SAMANKASSOU, E., MÜLLER, I. A., SZYMANOWSKI, D., LOOSER, N., TAVAZZANI, L., MERINO-TOMÉ, Ó., BAHAMONDE, J. R., BURET, Y. & OVCHAROVA, M. 2024. Technical note: RA138 calcite U-Pb LA-ICP-MS primary reference material. *GChron* **6(3)**, 465-474.  
<https://doi.org/10.5194/gchron-6-465-2024>
- HAINES, P. W., TURNER, S. P., FODEN, J. D. & JAGO, J. B. 2009. Isotopic and geochemical characterisation of the Cambrian Kanmantoo Group, South Australia: implications for stratigraphy and provenance. *Australian Journal of Earth Sciences* **56(8)**, 1095-1100  
<https://doi.org/10.1080/08120090903246212>
- HARRISON, A. & WHITE, R. S. 2006. Lithospheric structure of an active back-arc basin: the Taupo Volcanic Zone, New Zealand. *Geophysical Journal International* **167(2)**, 968-990.  
<https://doi.org/10.1111/j.1365-246X.2006.03166.x>
- HILL, C. A., POLYAK, V. J., ASMEROM, Y. & PROVENCIO, P. P. 2016. Constraints on a Late Cretaceous uplift, denudation and incision of the Grand Canyon region, southwestern Colorado Plateau, USA, from U-Pb dating of lacustrine limestone. *Tectonics* **35**, 896-906.  
<https://doi.org/10.1002/2016TC004166>
- HOGMALM, K. J., ZACK, T., KARLSSON, A. K.-O., SJÖQVIST, A. S. L. & GARBE-SCHÖNBERG, D. 2017. *In situ* Rb-Sr and K-Ca dating by LA-ICP-MS/MS: an evaluation of N<sub>2</sub>O and SF<sub>6</sub> as reaction gases. *Journal of Analytical Atomic Spectrometry* **32(2)**, 305-313.  
<https://doi.org/10.1039/C6JA00362A>
- HONG, W., FABRIS, A., GILBERT, S., WADE, B. P., COLLINS, A. S., WISE, T. & REID, A. J. 2024. Using zircon and apatite chemistry to fingerprint porphyry Cu – Mo±Au mineralization in the Delamerian Orogen, South Australia. *Mineralium Deposita* **59(1)**.  
<https://doi.org/10.1007/s00126-024-01287-y>
- HONG, W., FABRIS, A., WISE, T., COLLINS, A. S., GILBERT, S., SELBY, D., CURTIS, S. & REID, A. J. 2023. Metallogenic Setting and Temporal Evolution of Porphyry Cu-Mo Mineralization and Alteration in the Delamerian Orogen, South Australia: Insights From Zircon U-Pb, Molybdenite Re-Os, and *In situ* White Mica Rb-Sr Geochronology. *Society of Economic Geologists* **118**, 1291-1318.  
<https://doi.org/10.5382/econgeo.5012>
- HUSTON, D., CAYLEY, R. A. & CHAMPION, D. 2015. The giant Lachlan Orocline- A powerful new predictive tool for mineral exploration undercover across eastern Australia. *Mines & Wines*.  
[PowerPoint Presentation \(smedg.org.au\)](PowerPoint Presentation (smedg.org.au))
- HUSTON, D., CAYLEY, R. A. & CHAMPION, D. 2015. Metallogenesis of the Lachlan Orocline: Is the is the mineral wealth of southeast Australia due to the accretion of VanDieland? *Mines & Wines*.
- IRELAND, T. R., FLÖTTMANN, T., FANNING, C. M., GIBSON, G. M. & PREISS, W. V. 1998. Development of the early Paleozoic Pacific margin of Gondwana from detrital-zircon ages across the Delamerian Orogen. *Geology* **26(3)**, 243-246.  
[https://doi.org/10.1130/0091-7613\(1998\)026<0243:DOTEPP>2.3.CO;2](https://doi.org/10.1130/0091-7613(1998)026<0243:DOTEPP>2.3.CO;2)
- JOHNSON, E. L., PHILLIPS, G. & ALLEN, C. M. 2016. Ediacaran-Cambrian basin evolution in the Koonenberry Belt (eastern Australia): Implications for the geodynamics of the Delamerian Orogen. *Gondwana Research* **37**, 266-284.  
<https://doi.org/10.1016/j.gr.2016.04.010>
- JOHNSON, M. R. W. & HARLEY, S. L. 2012. Orogenesis: The making of mountains. *Cambridge University Press*.
- KORSCH, R. J., FOMIN, T., CONOR, C. H. H., STEVENS, B. P. J., GOLEBY, B. R., ROBERTSON, R. S. & PREISS, W. V. 2006. A deep seismic reflection transect across the Curnamona Province from the Darling basin to the Flinders Ranges. *Broken Hill Exploration Initiative*.
- KURTZSCHBACH, M. & GLODNY, J. 2024. LA-ICP-MS/MS-based Rb-Sr isotope mapping for geochronology. *Journal of Analytical Atomic Spectrometry* **39**, 455-477.  
<https://doi.org/10.1039/D3JA00297G>
- LANE, R. J. L., WYNNE, P. E., POUDJOM DJOMANI, Y., STRATFORD, W. R., BARRETTO, J. A. & CARATORI TONTINI, F. 2019. Australian National Gravity Grids: Free Air Anomaly, Complete Bouger Anomaly, De-trended Global Isostatic Residual, 400m cell size. Geoscience Australia, Canberra.
- LEWIS, C. J., TAYLOR, D. H., CAYLEY, R. A., SCHOFIELD, A. & SKLADZIEN, P.B. 2015. New SHRIMP U-Pb zircon ages from the Stavely region, western Victoria, Geoscience Australia.  
<http://dx.doi.org/10.11636/Record.2015.026>



- LI, Z. X., BOGDANOVA, S. V., COLLINS, A. S., DAVIDSON, A., DE WAELE, B., ERNST, R. E., FITZSIMONS, I. C. W., FUCK, R. A., GLADKOCHUB, D. P., JACOBS, J. KARLSTROM, K. E., LU, S. NATAPOV, L. M., PEASE, V., PISAREVSKY, S. A., THRANE, K. & VERNIKOVSKY, V. 2008. Assembly, configuration, and break-up history of Rodinia: A synthesis. *Precambrian Research* **160**(1-2), 179-210.  
<https://doi.org/10.1016/j.precamres.2007.04.021>
- LI, Z. X., LIU, Y. & ERNST, R. 2023. A dynamic 2000-540 Ma Earth history: From cratonic amalgamation to the age of supercontinent cycle. *Earth-Science Reviews* **238**, 104336.  
<https://doi.org/10.1016/j.earscirev.2023.104336>
- LI, Z. X., ZHANG, L. & POWELL, C. M. 1995. South China in Rodinia: Part of the missing link between Australia–East Antarctica and Laurentia? *Geology* **23**(5), 407-410.  
[https://doi.org/10.1130/0091-7613\(1995\)023<0407:SCIRPO>2.3.CO;2](https://doi.org/10.1130/0091-7613(1995)023<0407:SCIRPO>2.3.CO;2)
- LISTER, G. & FORSTER, M. (2009). Tectonic mode switches and the nature of orogenesis. *Lithos* **113**, 274-291.  
<https://doi.org/10.1016/j.lithos.2008.10.024>
- MCDONOUGH, W. F. & SUN, S. -S. 1995. The composition of the Earth. *Chemical Geology* **120**(3-4), 223-253.  
[https://doi.org/10.1016/0009-2541\(94\)00140-4](https://doi.org/10.1016/0009-2541(94)00140-4)
- MERDITH, A. S., WILLIAMS, S. E., BRUNE, S., COLLINS, A. S. & MÜLLER, R. D. 2019. Rift and plate boundary evolution across two supercontinent cycles. *Global and Planetary Change* **173**, 1-14.  
<https://doi.org/10.1016/j.gloplacha.2018.11.006>
- MERDITH, A. S., WILLIAMS, S. E., COLLINS, A. S., TETLEY, M. G., MULDER, J. A., BLADES, M. L., YOUNG, A., ARMISTEAD, S. E., CANNON, J., ZAHIROVIC, S. & MÜLLER, R. D. 2021. Extending full-plate tectonic models into deep time: Linking the Neoproterozoic and the Phanerozoic. *Earth Science reviews* **214**, 103477.  
<https://doi.org/10.1016/j.earscirev.2020.103477>
- MERDITH, A.S., WILLIAMS, S. E., MÜLLER, R. D. & COLLINS, A. S. 2017. Kinematic constraints on the Rodinia to Gondwana transition. *Precambrian Research* **299**, 132-150.  
<https://doi.org/10.1016/j.precamres.2017.07.013>
- MOLE, D., CLARK, A., BODORKOS, S. & LEWIS, C. 2024. New U-Pb SHRIMP zircon geochronology from NDI drilling of the Delamerian Orogen: Loch Lilly-Kars and Lake Wintlow Belts, southwest NSW. GA Record 2024/21. Geoscience Australia, Canberra.  
<https://dx.doi.org/10.26186/149417>
- MORTIMER, G.E., COOPER, J. A. & JAMES, P.R. 1987. U Pb and Rb Sr geochronology and geological evolution of the Harts Range ruby mine area of the Arunta Inlier, central Australia. *Lithos* **20**(6), 445-476.  
[https://doi.org/10.1016/0024-4937\(87\)90029-6](https://doi.org/10.1016/0024-4937(87)90029-6)
- MORESI, L., BETTS, P. G., MILLER, M. S. & CAYLEY R.A. 2014. Dynamics of continental accretion. *Nature*, **508**, 245-248.  
<https://doi.org/10.1038/nature13033>
- NORRIS, A & DANYUSHEVSKY, L. 2018. Towards Estimating the Complete Uncertainty Budget of Quantified Results Measured by LA-ICP-MS. *Goldschmidt*, Boston, 2018—8-12.  
<http://norsci.com/ladr/>
- PATON, C. HELLSTROM, J., PAUL, B., WOODHEAD, J. & HERGT, J. 2011. Iolite: Freeware for the visualisation and processing of mass spectrometric data. *Journal of Analytical Atomic Spectrometry* **26**(12), 2508-2518.  
<https://doi.org/10.1039/C1JA10172B>
- PETRUS, J. A., CHEW, D. M., LEYBOURNE, M. I. & KAMBLER, B. S. 2017. A new approach to laser-ablation inductively-coupled-plasma mass-spectrometry (LA-ICP-MS) using the flexible map interrogation tool Monocle? *Chemical Geology* **463**, 76-93.  
<https://doi.org/10.1016/j.chemgeo.2017.04.027>
- POUDJOM DJOMANI, Y., MINTY, B. R.S., HUTCHENS, M. & LANE, R. J. L. 2019. Total Magnetic Intensity (TMI) Grid of Australia 2019- seventh edition – 80m cell size. Geoscience Australia, Canberra.  
<https://dx.doi.org/10.26186/5e9cf3f2c0f1d>
- RASBURY, E. T. & COLE, J. M. 2009. Directly dating geologic events: U-Pb dating of carbonates. *Reviews of Geophysics* **47**(3), 1-27.  
<https://doi.org/10.1029/2007RG000246>
- REDAA, A., FARKAS, J., GILBERT, S., COLLINS, A. S., LÖHR, S., VASEGH, D., FORSTER, M., BLADES, M., ZACK, T., GIULIANI, A., MASS, R., BALDERMANN, A., DIETZEL, M. & GARBE-SCHÖNBERG, D. 2023. Testing Nano-Powder and Fused-Glass Mineral Reference Materials for *in-situ*



- Rb-Sr Dating of Glauconite, Phlogopite, Biotite and Feldspar via LA-ICP-MS/MS. *Geostandards and Geoanalytical Research* **47**(1), 23-48.  
<https://doi.org/10.1111/ggr.12467>
- REDAA A., FARKAS, J., GILBERT, S., COLLINS, A. S., WADE, B., LÖHR, S., ZACK, T. & GARBE-SCHÖNBERG, D. 2021. Assessment of elemental fractionation and matrix effects during *in-situ* Rb-Sr dating of phlogopite by LA-ICP-MS/MS: implications for the accuracy and precision of mineral ages. *Journal of Analytical Spectrometry* **36**(2), 322-344.  
<https://doi.org/10.1039/D0JA00299B>
- ROBERTS, N. M. W., RASBURY, E. T., PARRISH, R. R., SMITH, C. J., HORSTWOOD, M. S. A. & CORDON, D. J. 2017. A calcite reference material for LA-ICP-MS U-Pb geochronology. *Geochemistry, Geophysics, Geosystems* **18**(7), 2807-2814.  
<https://doi.org/10.1002/2016GC006784>
- ROLLINSON, H. & PEASE, V. 2021. Using Radiogenic Isotope Data. In: *Using Geochemical Data: To Understand Geological Processes*. Cambridge University Press. 178-218.  
<https://doi.org/10.1017/9781108777834.009>
- ŞENGÖR, A. M. C. 2020. Orogenic Belts. In: Gupta, H.K. (eds). *Encyclopedia of Solid Earth Geophysics. Encyclopedia of Earth Sciences series*. Springer, Cham.  
[https://doi.org/10.1007/978-3-030-10475-7\\_253-1](https://doi.org/10.1007/978-3-030-10475-7_253-1)
- SILLITOE, R.H. 2010. Porphyry Copper Systems. *Economic Geology* **105**(1), 3-41.  
<https://doi.org/10.2113/gsecongeo.105.1.3>
- SHAANAN, U., ROSENBAUM, G. & SIHOMBING, F. M. H. 2018. Continuation of the Ross-Delamerian Orogen: insights from eastern Australian detrital-zircon data. *Australian Journal of Earth Sciences*. **65**(7-8), 1123-1131.  
<https://doi.org/10.1080/08120099.2017.1354916>
- STEVENSON, R., HENRY, P., GARIÉPY, C. 1999. Assimilation-fractional crystallization origin of Archean Sanukitoid Suites: Western Superior Province, Canada. *Precambrian Research* **96**(1-2), 83-99.  
[https://doi.org/10.1016/S0301-9268\(99\)00009-1](https://doi.org/10.1016/S0301-9268(99)00009-1)
- STRAUB, S. M., GÓMEZ-TUENA, A. & VANNUCCHI, P. 2020. Subduction erosion and arc volcanism. *Nature Reviews Earth & Environment* **1**, 574-589.  
<https://doi.org/10.1038/s43017-020-0095-1>
- SUBARKAH, D., BLADES, M. L., COLLINS, A. S., FARKAS, J., GILBERT, S., LÖHR, S. C., REDAA, A., CASSIDY, E. & ZACK, T. 2022. Unraveling the histories of Proterozoic shales through *in-situ* Rb-Sr dating and trace element laser ablation analysis. *Geology* **50**(1), 66-70.  
<https://doi.org/10.1130/G49187.1>
- SUBARKAH, D., NIXON, A. L., GILBERT, S. E., COLLINS, A. S., BLADES, M. L., SIMPSON, A., LLOYD, J. C., VIRGO, G. M. & FARKAS, J. 2024. Double dating sedimentary sequences using new applications of in-situ laser ablation analysis. *Lithos* **480-481**. 107649.  
<https://doi.org/10.1016/j.lithos.2024.107649>
- TANAKA, T., DRAGUSANU, S., SHINJO, R., HIROSHI, A., YOSHIHIRO., SHIGEKO, T., MASAKI, Y., SHIGEKAZU, Y., KAZUYA, T., TAKANORI, N., MASAHARU, T., HIROSHI, S., HIROKAZU, F., HIROO, K., HIKARI, K., ORIHASHI, Y., TAKUJI, H., TAKERU, Y. & TAKANORI, K. 2000. JNdi-1: A neodymium isotopic reference in consistency with LaJolla neodymium. *Chem. Geol.* **168**, 279-281.  
[https://doi.org/10.1016/S0009-2541\(00\)00198-4](https://doi.org/10.1016/S0009-2541(00)00198-4)
- VERMEESCH, P. 2018. IsoplotR: a free and open toolbox for geochronology. *Geoscience Frontiers* **9**, 1479-1493.  
<https://doi.org/10.1016/j.gsf.2018.04.001>
- VERVOORT, J. 2018. Geochronology and Radiogenic Isotopes. *Encyclopedia of Geochemistry*, 571-586.  
[https://doi.org/10.1007/978-3-319-39312-4\\_291](https://doi.org/10.1007/978-3-319-39312-4_291)
- VILLAROS, A., STEVENS, G., MOYEN, J-F. & BUICK, I.S. 2009. The trace element compositions of S-type granites: evidence for disequilibrium melting and accessory phase entrainment in the source. *Contributions to Mineralogy and Petrology* **158**, 543-561.  
<https://doi.org/10.1007/s00410-009-0396-3>
- WADE, B. P., BAROVICH, K. M. HAND, M., SCRIMGEOUR, I. R. & CLOSE, D. F. 2006. Evidence for early Mesoproterozoic Arc Magmatism in the Musgrave Block, Central Australia: Implications for Proterozoic crustal Growth and Tectonic Reconstructions of Australia. *The Journal of Geology* **114**(1).  
<https://doi.org/10.1086/498099>
- WEN, B., EVANS, D. A. D., LI, Y. X. 2017. Neoproterozoic paleogeography of the Tarim Block: An extended or alternative “missing-link” model for Rodinia? *Earth and Planetary Science Letters* **458**, 92-106.  
<https://doi.org/10.1016/j.epsl.2016.10.030>


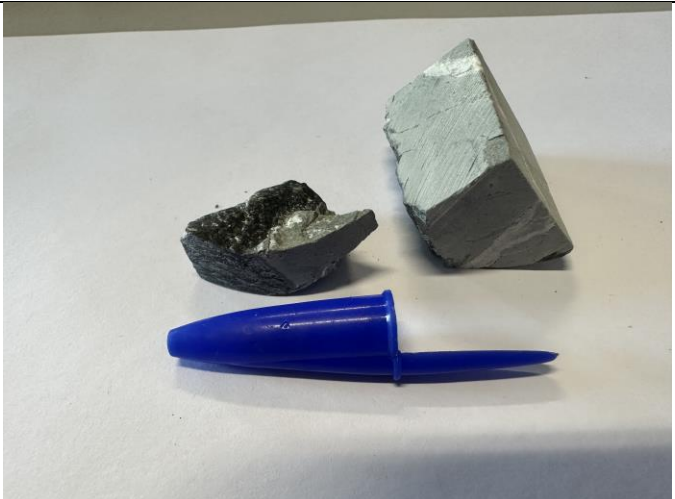
- WHALEN, J. B., PERCIVAL, J. A., MCNICOLL, V. J. & LONGSTAFFE, F. J. 2003. Intra-oceanic production of continental crust in a Th-depleted ca. 3.0Ga arc complex, western Superior Province, Canada. *Contributions to Mineralogy and Petrology* **146**, 78-99.  
[291https://doi.org/10.1007/s00410-003-0484-](https://doi.org/10.1007/s00410-003-0484-2)

## APPENDIX 1: TABLE OF SAMPLES AND EQUIVALENT HOLE AND DEPTH


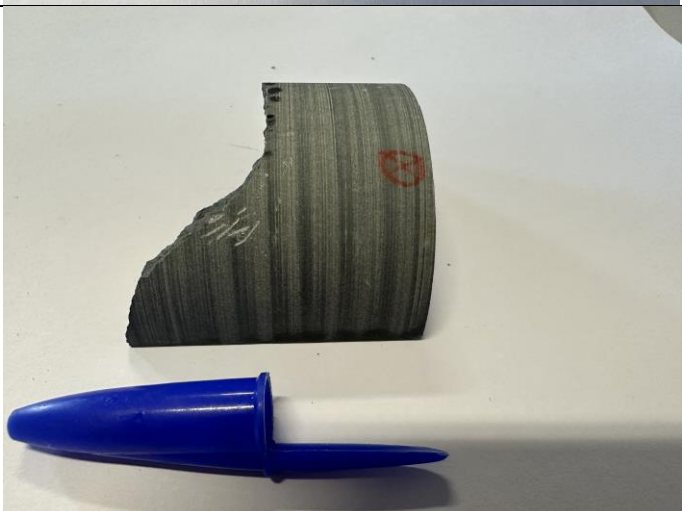
Sample Name	Description	Latitude	Longitude	Hole Number	Depth (m)
<b>LK12-186</b>	Shale cross-cut by carbonate veins	-32.5915	141.0916	NDILLK12	186.0 - 186.1
<b>LK12-173a</b>	Shale and felsic dyke contact	-32.5915	141.0916	NDILLK12	173.0
<b>LK12-173c</b>	Calcite vein (mineralised sulphides)	-32.5915	141.0916	NDILLK12	173.8
<b>LK12-173b</b>	Dyke shale margin + carbonate in dyke	-32.5915	141.0916	NDILLK12	173.15 - 173.25
<b>LK12-172</b>	Shale + dyke contact	-32.5915	141.0916	NDILLK12	172.3 - 172.37
<b>LK13-194</b>	Shale and interbedded carbonates	-32.6603	141.1043	NDILLK13	194.75 - 194.85
<b>LK13-198</b>	Shale and interbedded carbonates	-32.6603	141.1043	NDILLK13	198.85 - 199
<b>LK13-215</b>	Shale and interbedded carbonates	-32.6603	141.1043	NDILLK13	215.6 - 215.7
<b>LK13-214</b>	Shale and interbedded carbonates	-32.6603	141.1043	NDILLK13	214.7 - 214.8
<b>LK11-323</b>	Shale	-32.554	141.0915	NDILLK11	323.7
<b>LK11-369</b>	Shale	-32.554	141.0915	NDILLK11	369.3
<b>LK14-365</b>	Carbonate veins cross-cutting shale	-33.1389	141.0789	NDILLK14	365.1 - 365.15
<b>LK14-361</b>	Shale	-33.1389	141.0789	NDILLK14	361.6
<b>LK14-379</b>	Shale	-33.1389	141.0789	NDILLK14	379.6
<b>MP02-556</b>	Albitic altered host rock	-33.4995	141.6245	NDIWMP02	556.3 - 556.37
<b>MP02-628</b>	Fresh intermediate igneous rock	-33.4995	141.6245	NDIWMP02	628.8
<b>MP02-579</b>	Albitic altered host rock	-33.4995	141.6245	NDIWMP02	579 - 579.09
<b>MP02-560</b>	Albitic altered host rock	-33.4995	141.6245	NDIWMP02	560.49 - 560.65
<b>MP02-583</b>	Albitic altered host rock	-33.4995	141.6245	NDIWMP02	583.5 - 583.7
<b>MP03-493</b>	Albitic altered host rock	-33.7688	141.4251	NDIWMP03	493.43
<b>MP03-548</b>	Albitic altered host rock	-33.7688	141.4251	NDIWMP03	548.7 - 548.8
<b>MP03-546</b>	Albitic igneous rock with veining	-33.7688	141.4251	NDIWMP03	546.6 - 546.8

## APPENDIX 2: SAMPLE PHOTOS AND DESCRIPTION



SAMPLE ID	DESCRIPTION	PHOTO
<b>LK12 186</b>	This sample is dominantly shale with cross-cutting carbonate veins throughout. The shale is bordering on being a siltstone looks to be dominantly lithics (>85%) with the remainder quartz (15%) no feldspars are present and no obvious bedding layers. Carbonate veins appear to be multi-generational.	
<b>LK12 173a</b>	This sample shows the clear contact between a very fine-grained igneous dyke and its host sediment. The dyke is grey in colour and the shale is the darker region and we can see clear bedding in the shale of ~1mm between lithic-rich layers and quartz-rich layers. The contact between the two is almost white in color and we see evidence of small veins breaking away from the main intrusion.	

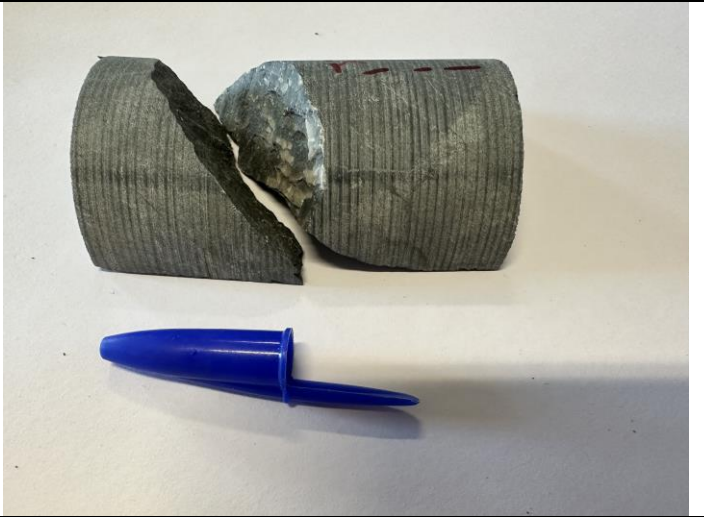

<b>LK12 173c</b>	<p>This sample is one of two samples that show sulphide mineralisation. It contains shale and complex carbonate veining throughout with sulphides only prevalent at the contact with the shale. The sulphides appear to be purely pyrite.</p>	
<b>LK12 173b</b>	<p>The only sample I have which contains the shale + dyke + carbonate. The dyke intrudes the shale and has resulted in the shale being metamorphosed and gaining a 'sheen' to it. The dyke is then subsequently intruded by carbonate veins indicating two generations of intrusion. No sulphides are present in this sample. Given the appearance and colouration, this dyke looks to be part of the same system from LK12 173a.</p>	

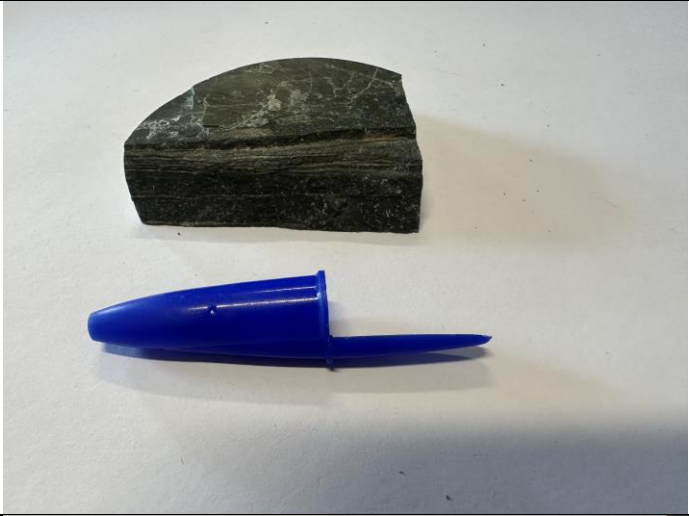





<b>LK12 172</b>	<p>This sample contains another contact between the dyke and shale. We can see that the contact appears to contain little veins of carbonate which look to be following this contact as a point of weakness. The shale no longer has straight bedding and appears to have been warped by the heat that either the dyke or carbonate have imparted on it.</p>	
<b>LK13 194</b>	<p>This core piece is an example of the interbedded carbonate and shale. The beds appear to be consistent. The shale is the dominant lithology but there appears to be a regular pattern. This likely indicates stable formation conditions and the change could be attributed to Milankovitch cycles more than tectonics.</p>	





<b>LK13 198</b>	<p>Another example from LLK13 of the interbedded carbonate and shale. We see the same consistent beds but compared to LLK13 194 this doesn't look as 'clean' with evidence for patches of carbonate present and not in beds. There are also very small veins through it like the one on the right side of this photo.</p>	 A photograph of a cylindrical rock core sample, LK13 198. The sample is dark grey to black with visible horizontal banding, indicating interbedded layers of carbonate and shale. There are some reddish-brown stains on the left side. A blue pen is placed below the sample for scale.
<b>LK13 215</b>	<p>More bedded shale + carbonates from LLK13. This sample also not as 'clean' as LLK13 194. We can see evidence for alteration post deposition here and more fine carbonate veins.</p>	 A photograph of a cylindrical rock core sample, LK13 215. The sample is dark grey to black with visible horizontal banding, indicating bedded shale and carbonates. There are some reddish-brown stains on the left side. A blue pen is placed below the sample for scale.



<b>LK13 214</b>	<p>Our last of 4 interbedded shale + carbonate sequences. We can see more clearly on this sample the alteration throughout. We see in the right piece, a contact between the lighter, more altered region and the darker less altered region. This shows we have not only interbedded carbonates but also a phase of post deposition alteration as fluids moved through the sequences.</p>	
<b>LK11 323</b>	<p>This sample is our most classic shale. It exhibits very little 'sheen' indicating it likely is our least altered shale. It also lacks the carbonate beds seen in LLK13 drill hole and there is no obvious lithological difference between bedding layers with quite a homogenous mineralogy. Dominantly lithics with minimal quartz (~10-20%) and no feldspars (&lt;1%).</p>	



<b>LK11 369</b>	<p>Another shale sample which lacks the bedded carbonates and is dominantly lithics. We can also see in this sample that while there is minimal lithological difference between the beds, that each bed is only sub-mm in scale. This sample is beginning to give that 'slaty' appearance to it unlike LLK11 323 indicating it might have been subjected to higher temperatures.</p>	 A photograph of a dark, sub-mm bedded shale sample (LK11 369) next to a blue pen for scale. The sample is a dark, irregularly shaped piece of rock with a fine, sub-mm bedded texture. The blue pen is positioned horizontally below the sample for scale.
<b>LK14 365</b>	<p>This sample is the second and final sample that contains sulphides. These sulphides are again spatially associated with the contact between the complex carbonate veins and shale. This sample shows how complex these carbonate veins are with at least 3 different generations of veining. The largest veins run ~60° to the small veins. The shale is again very dark and lacks any obvious bedding features but it does appear that the smaller veins tend to almost follow bedding planes.</p>	 A photograph of a dark, complexly veined shale sample (LK14 365) next to a blue pen for scale. The sample is a dark, irregularly shaped piece of rock with complex, multi-directional veining. The blue pen is positioned horizontally below the sample for scale.

<b>LK14 361</b>	<p>An example of a metamorphosed shale. It is a much shinier sample than those from LLK11 and we can see clearly the extent of alteration the sample has undergone on the top surface here with significant discolouration to the darker shale. Bedding is not visible on this sample at all and has likely been overprinted by the metamorphism it has undergone. Is not yet a phyllite or slate.</p>	 A photograph of a dark, shiny metamorphosed shale sample (LK14 361) resting on a white surface. A blue pen is placed horizontally below the rock sample to provide a sense of scale. The rock has a smooth, dark surface with some lighter, irregular patches of alteration.
<b>LK14 379</b>	<p>This sample is another example of a shale but here we have an example of some of the structural complexity in these rocks. We can see bedding layers of shale and carbonate and a generation of carbonate veining running perpendicular to those beds. We can also see subsequent to that that these veins have been offset by small-scale faults.</p>	 A photograph of a shale sample (LK14 379) resting on a white surface. A blue pen is placed horizontally below the rock sample to provide a sense of scale. The rock shows distinct bedding layers and a network of carbonate veining running perpendicular to the beds. Some of the veins appear to be offset by small-scale faults.



<b>MP02 556</b>	<p>This sample is the original sample that thin section and geochemical analysis sample MP02A came from. We can see clearly here the breccia veins that are co obvious in thin section and the complete alteration of any original sample textures that existed. Based on analysis this sample was initially an igneous intermediate rock that has been overprinted and brecciated by subsequent magmatism and/or hydrothermal activity.</p>	
<b>MP02 628</b>	<p>This sample is the original sample than thin section and geochemical analysis MP02B came from. This sample is clearly an intermediate igneous rock. It is fine-medium crystal size but mineralogically quite simple. The dark parches are biotite and light are a mix of quartz and plagioclase. It does not look to be highly altered.</p>	



<b>MP02 579</b>	<p>This is another example of the alteration breccia present in MP02. We can again see the extent of alteration with no original features of the rock being preserved. The brecciation has at least two generations, with some veins off-set by further brecciation. The sample exhibits the same albitic alteration seen in MP02 556.</p>	 A photograph of a rock sample labeled MP02 579. The sample is a brecciated rock, appearing as a collection of small, angular fragments of light-colored rock cemented together. A blue pen is placed horizontally below the rock for scale.
<b>MP02 560</b>	<p>This is another example of our alteration breccia and this sample in particular shows the sheer complexity of the alteration. This sample shows the extent to which broken material has been re-worked by these penetrating fluids with the pieces in the veins no longer clearly fitting together like puzzle pieces and already brecciated material being broken into even smaller pieces. We can see that this drill hole has at least a 50m section of this within it and indicates the size of the event.</p>	 A photograph of a rock sample labeled MP02 560. The sample is a long, thin, and highly brecciated rock fragment, showing a complex internal structure with many small, irregular pieces. A blue pen is placed horizontally below the rock for scale.

<b>MP02 583</b>	<p>Our final alteration breccia sample. Shows the same perverse albitic alteration but the brecciation is less complex and pronounced here.</p>	
<b>MP03 493</b>	<p>This sample is likely a proxy for what the host rock of the alteration breccia in our MP02 samples originally looked like. It is also the sample which geochemical and thin section analysis sample MP03A is. We can see an intermediate igneous rock with its coarsest phase being a dark mineral. We can see that this sample has also been altered as shown by the lighter almost yellow colouration throughout it, however much less significant than MP02. It is likely also albitic.</p>	

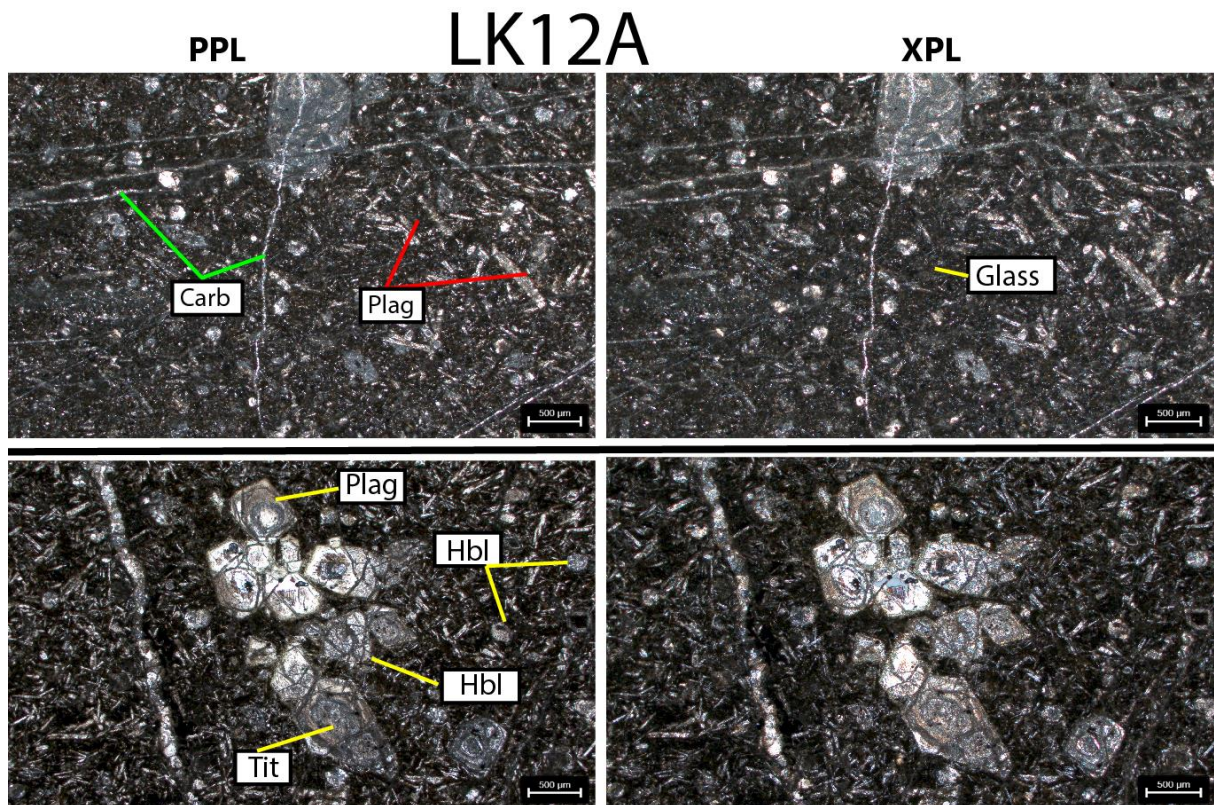


<p><b>MP03 548</b></p>	<p>This sample is what our geochemical and thin section analysis sample MP03B was taken from (bottom piece). The bottom piece is likely the least altered igneous sample we have from the entire collection. We do not see any of that yellow discolouration throughout it. The top piece shows some discolouration and is again an intermediate igneous rock with the largest mineral phase being the black crystals seen without a hand lens.</p>	
<p><b>MP03 546</b></p>	<p>This sample shows the same intermediate rock seen in other MP03 samples but in this case we see cross-cutting intrusive veins and its associated alteration halo. We can see that the veins impart the yellow discolouration to the host igneous suite. This sample likely shows the middle-ground between those fresher igneous samples in MP03 and the alteration breccias that dominate the samples in MP02 and shows a likely mechanism for the alteration.</p>	

### APPENDIX 3: DETAILED THIN SECTION DESCRIPTIONS OF IGNEOUS SAMPLES FROM LLKB

#### Appendix 3A: LK12A

Sample LLK12A is dominated (>60% of sample) by a matrix of glass and acicular plagioclase crystals along with more rounded hornblende crystals which have no preferential growth direction. There are remnants of original phenocrysts which have been altered to a point where original composition is impossible to deduce but based on the remnant shape, they appear to be dominantly olivine and hornblende with a small number of titanite crystals. There is a significant number of thin carbonate veins which run through the thin section in multiple directions and some cross-cutting other veins, indicating multiple phase carbonate intrusion.



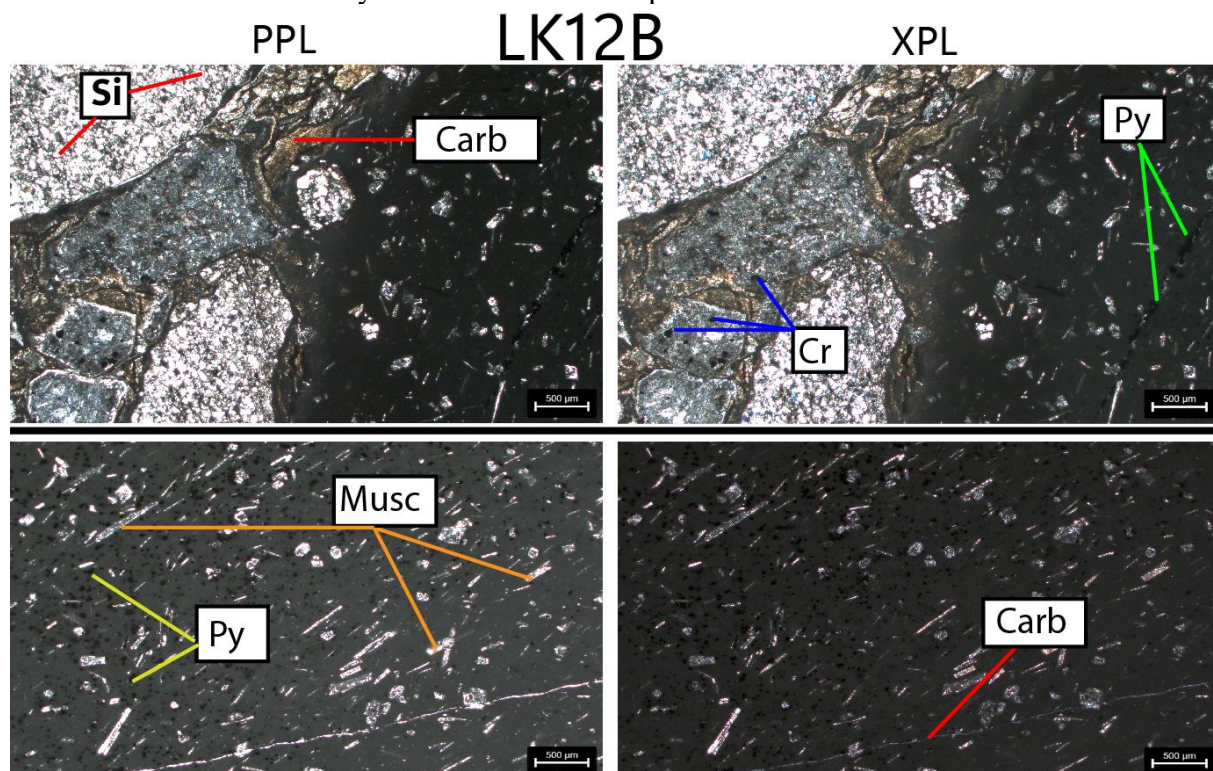
Annotated thin section photos taken of LLK12A (NDILLK12-172) sample. Photos on the left are PPL and photos on the right are XPL. Carb = Carbonate, Plag = Plagioclase, Hbl = Hornblende, Tit = Titanite, Glass = Glass.

#### Appendix 3B: LK12B

Sample LLK12B is a thin section of the contact between the host sediment and fine-grained intrusive from LLK12A. The host sediment is dominantly fine-grained, sub-rounded quartz (65%) and very fine-grained lithic fragments. The intrusion contains a dominantly glass matrix with small acicular muscovites (mineralogy deduced from MLA maps (Figure \*\*)) which are orientated parallel to the contact boundary. The



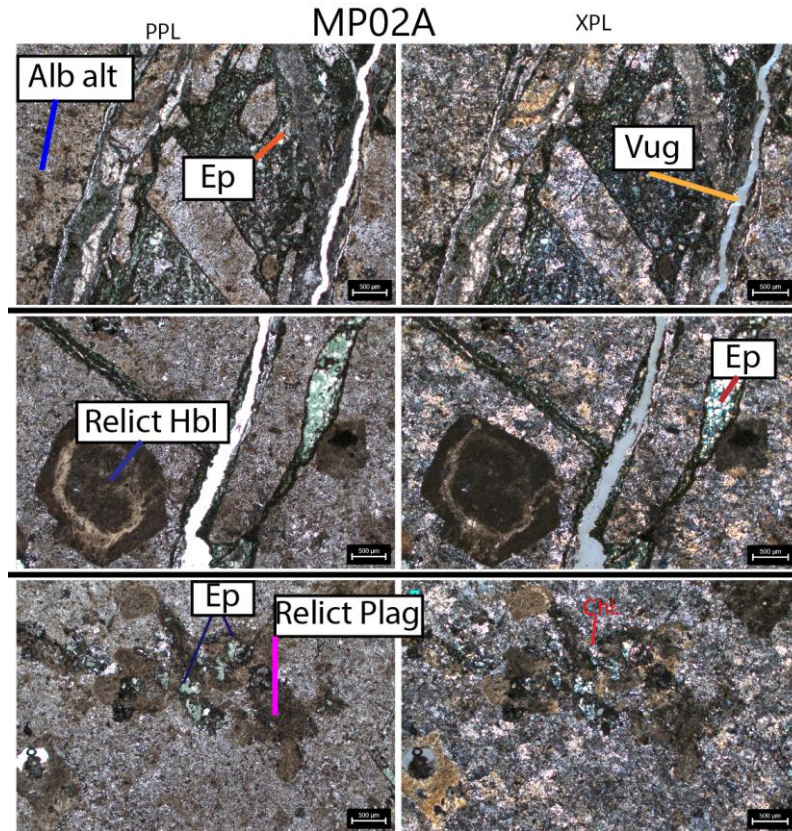
intrusion contains oxides both disseminated and veined (Figure \*\*). The oxides inside the intrusion are exclusively pyrite. The intrusion is also cross-cut by carbonate veins. The alteration halo between the intrusion and host sediment contains carbonate and large plagioclase crystals (width greater than 500µm) which don't exist elsewhere in the sample. These plagioclase crystals have chromite located around their rims and this chromite does not occur anywhere else in the sample either.



Annotated thin section photos taken of LLK12B (NDILLK12-173) sample. Photos on the left are PPL and photos on the right are XPL. Carb = Carbonate, Musc = Muscovite, Py = Pyrite, Cr = Chromite.

### Appendix 3C: MP2A

Sample MP02 is a thin section of the alteration breccia present dominantly in our NDIWMP02 drillhole. The sample is a highly altered igneous host rock. The alteration is albitic and phenocrysts have been altered beyond recognition or in some cases completely destroyed but we can see their euhedral character prior to alteration supporting the assumption they are initially igneous crystals. The sample brecciation contains an infill of dominantly epidote and chlorite. There is also a significant amount of pore-space remaining in these breccia veins. It is difficult to determine the previous mineral assemblage of the sample but looking at relict crystals, we can see that initially it was dominantly plagioclase and hornblende, similar to MP3B. These have partially broken down to epidote in some cases.

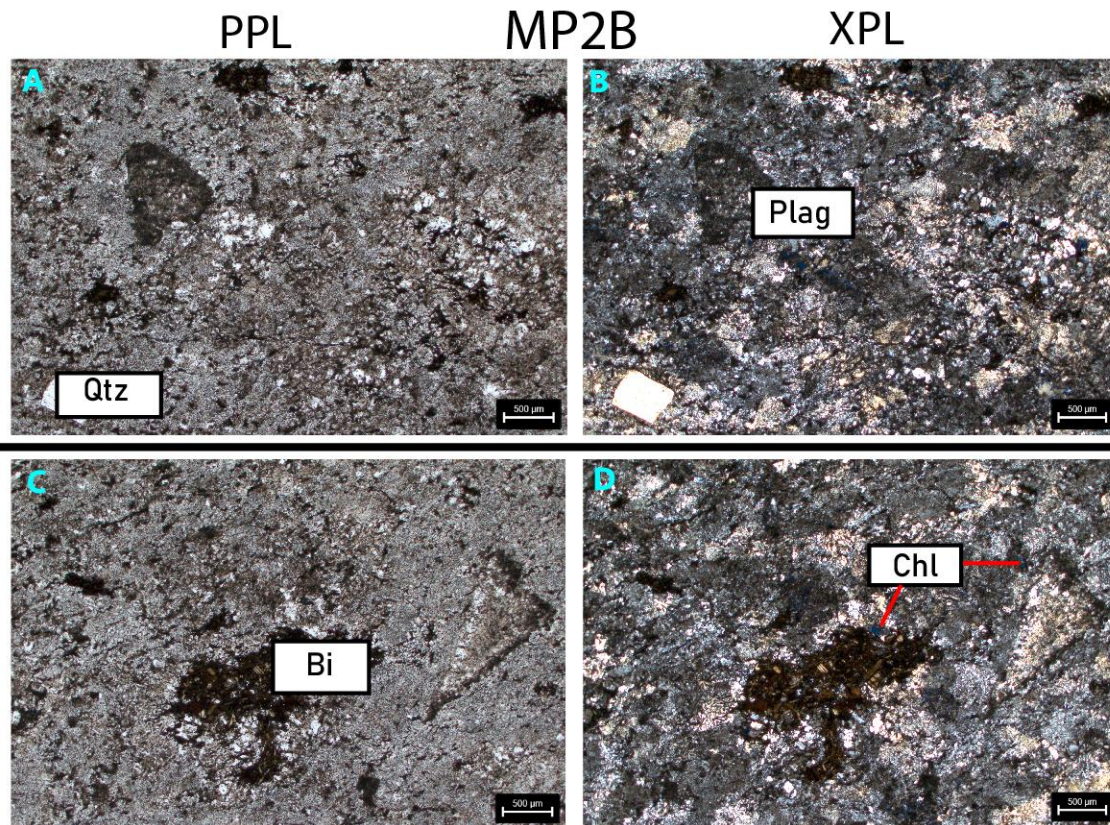


Annotated thin section photos taken of MP2A (MP02-556) sample. Photos on the left are PPL and photos on the right are XPL. Alb alt = Albitic alteration, Ep = Epidote, Vug = air, relict Hbl = Relict Hornblende, Relict Plag = relict Plagioclase.

### Appendix 3D: MP2B

Sample MP2B is a thin section of our only fresh igneous sample from drillhole NDIWMP02. It is a fine-grained felsic intrusive rock which is dominated by fine-grained quartz (40%), fine-grained plagioclase (35%) & Biotite (20%) which grows exclusively in clumps. Biotite is the largest crystals in this sample except for a small number of large square quartz crystals. Some biotite crystals on the edge of the clumps has broken down to chlorite.



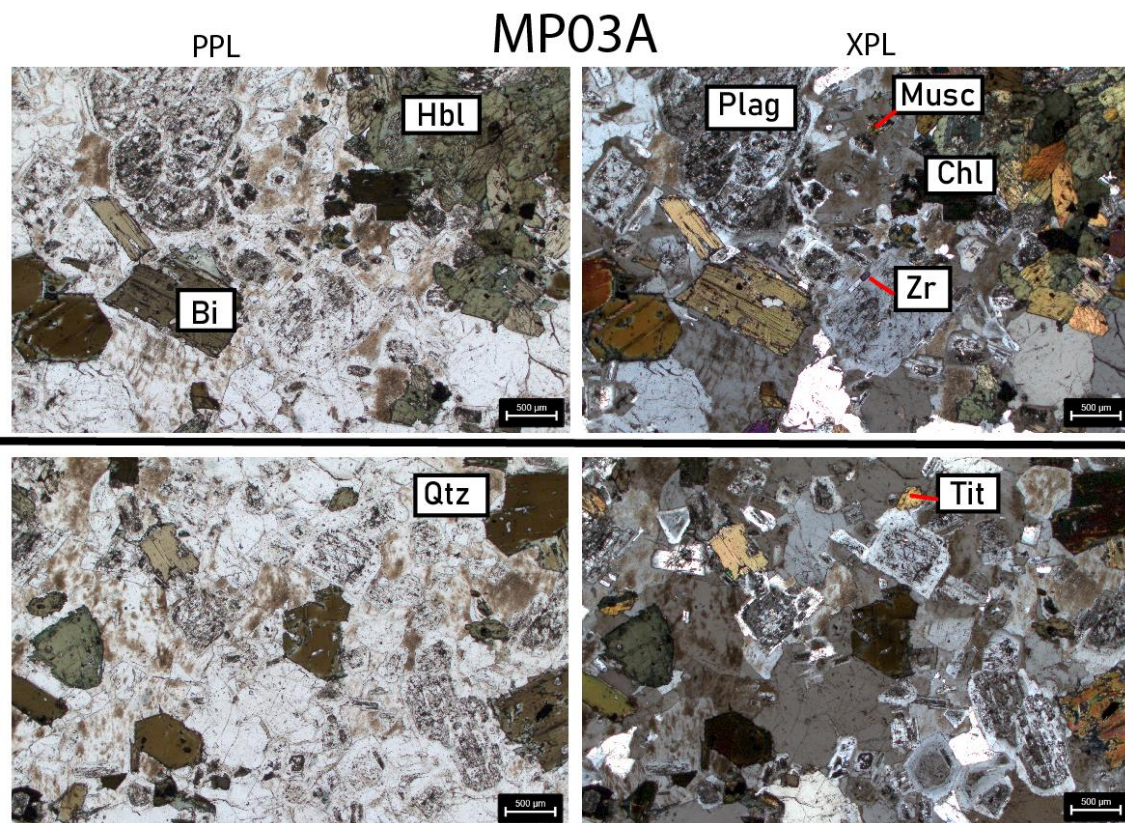


Annotated thin section photos taken of MP2B (MP02-628) sample. Photos on the left are PPL and photos on the right are XPL. Qtz = quartz, Chl = chlorite, Bi = biotite, Plag = plagioclase.

### Appendix 3E: MP3A

MP3A is a thin section of the freshest and coarsest igneous intrusive rock in this project. The dominant mineral phases are quartz and plagioclase (~30% each). The quartz contains a pervasive iron-stain throughout it which makes it easy to separate from the plagioclase which shows the classic sieve texture seen in intrusions that see multiple phases of pooling in the crust before emplacement. The plagioclase contain very clean outer rims in almost all cases. Hornblende (20%) is coarse-grained and grows in clumps together. The minor mineral phases are Biotite (10%) which when close to iron-stained quartz has broken down to chlorite (5%), muscovite (4%) and zircon and titanite (<1%).



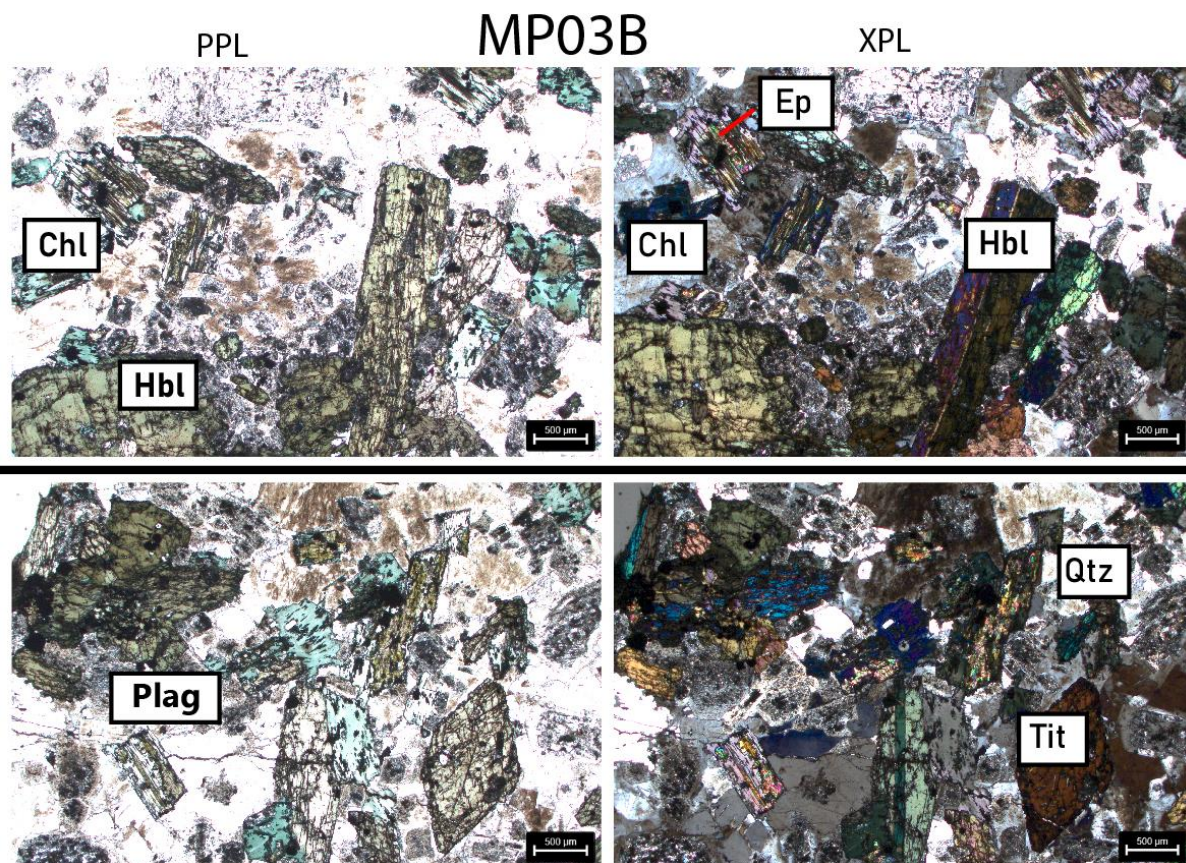


Annotated thin section photos taken of MP3A (MP03-493) sample. Photos on the left are PPL and photos on the right are XPL. Qtz = quartz, Chl = chlorite, Bi = biotite, Plag = plagioclase, Hbl = hornblende, Tit = titanite, Zr = zircon, Musc = muscovite.

### Appendix 3F:MP3B

MP3B is a thin section of an igneous intrusive sample from drillhole NDIWMP03. The sample itself comes from the freshest portion of an altered sample and as such it is not completely fresh. This is obvious when looking at the mineral textures. We can see that the biotite that was originally in the sample has completely broken down to a chlorite (15%) and epidote (5%) assemblage. The hornblende (35%) in this sample shows very distinct simple twinning. There are also a number of coarse titanite crystals (5%). These plagioclase crystals are smaller than MP3A (10%) and do not contain clean rims unlike MP3A and the quartz (30%) iron-staining is a darker colour in this sample too.





Annotated thin section photos taken of MP3B (MP03-548) sample. Photos on the left are PPL and photos on the right are XPL. Qtz = quartz, Chl = chlorite, Ep = epidote, Plag = plagioclase, Hbl = hornblende, Tit = titanite.

#### APPENDIX 4: ELEMENTAL DWELL TIMES FOR LA-ICP-MS RB–SR SPOT AND ELEMENTAL MAPPING ANALYSIS

Elemental dwell times for LA-ICP-MS Rb–Sr spot & elemental mapping analysis

Element	Atomic Mass	Dwell Time (ms)
<b>K</b>	39	2
<b>Mg</b>	24	2
<b>Y</b>	89	5
<b>Rb</b>	85	10
<b>Li</b>	7	2
<b>P</b>	31	2
<b>Sr</b>	88	20
<b>Sr</b>	87	5
<b>Sr</b>	86	5
<b>Ca</b>	43	2
<b>Si</b>	29	2
<b>Ti</b>	48	2
<b>Ce</b>	140	5
<b>Na</b>	23	2
<b>Fe</b>	56	2

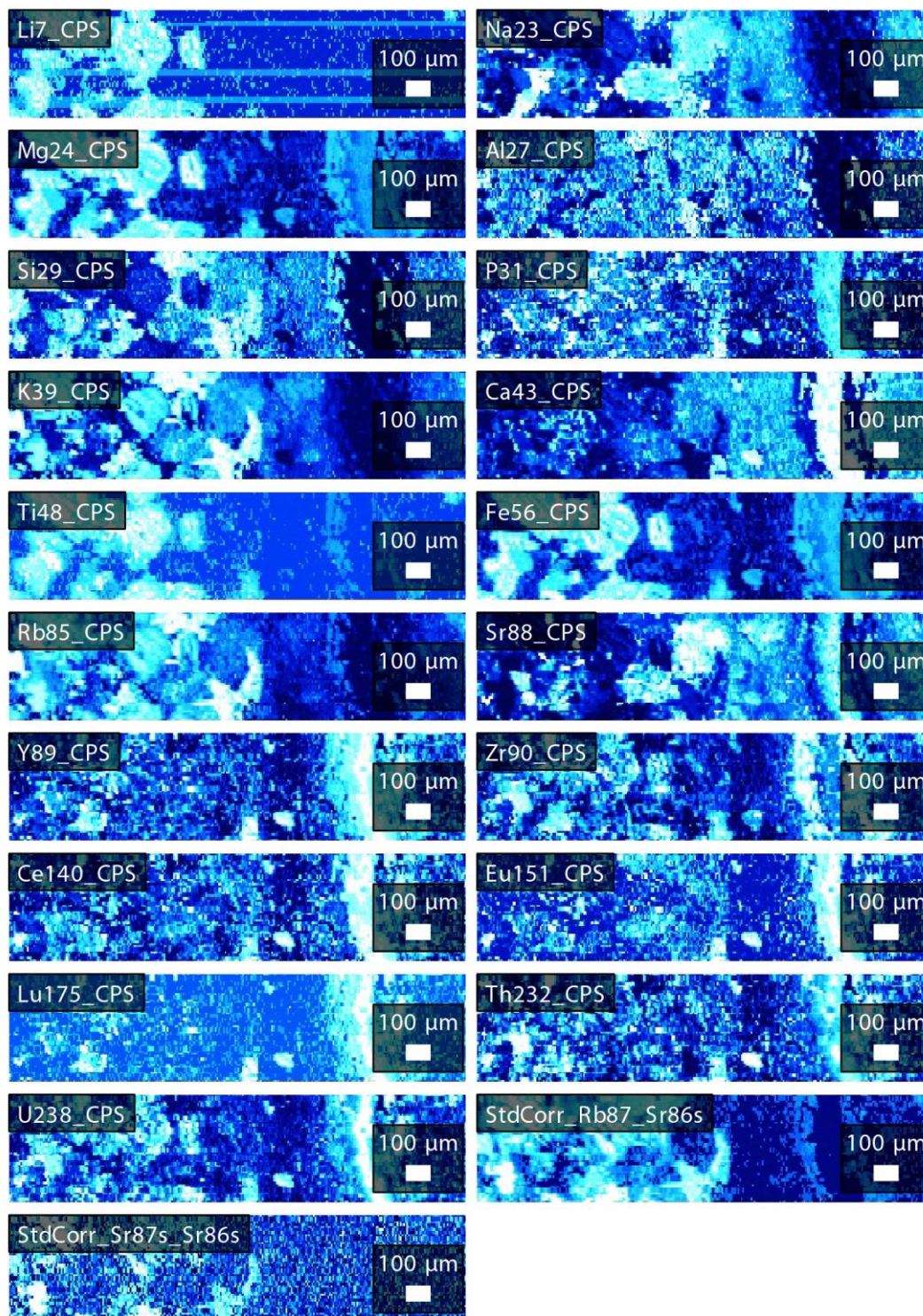


<b>Al</b>	27	2
<b>Eu</b>	151	5
<b>Lu</b>	175	5
<b>U</b>	238	5
<b>Zr</b>	90	5
<b>Th</b>	232	5
<b>TOTAL SWEEP TIME</b>		<b>95</b>

#### APPENDIX 5: ELEMENTAL DWELL TIMES FOR LA-ICP-MS U–PB ELEMENTAL MAPPING ANALYSIS

Element	Atomic Mass	Dwell Time (ms)
Al	27	2
Si	29	2
P	31	2
Ti	47	2
Ca	43	2
Fe	57	2
Mn	55	2
Rb	85	2
Zr	90	2
Ce	140	2
Hg	201	15
Pb	204	2
Pb	206	8
Pb	207	100
Pb	208	10
Th	232	10
U	238	40
U	235	20
Y	89	2
V	51	2
Sr	88	2
Ba	137	2
<b>TOTAL SWEEP TIME</b>		<b>233</b>

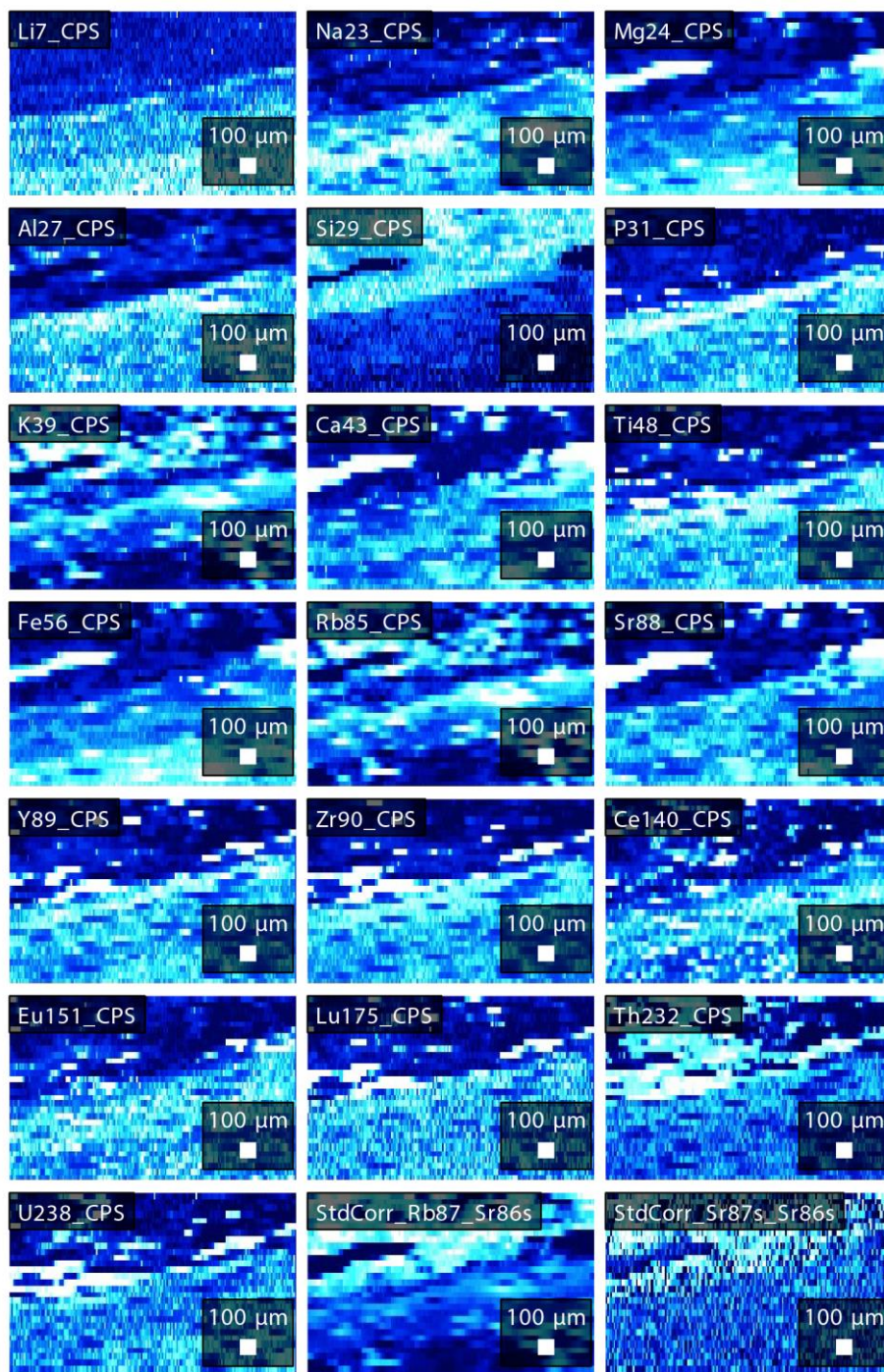
## APPENDIX 6: ELEMENTAL COMPOSITION MAPS FROM IOLITE4 FOR SAMPLE MP03-493.



Elemental concentration maps for all analysed elements in the LA-ICP-MS Rb–Sr method for sample MP03-493. Maps were used for the purpose of determining mineral phases in chip samples. Each map name is the element and atomic mass value for that sample. White colour responds to higher concentration of an element and blue is a lower concentration.



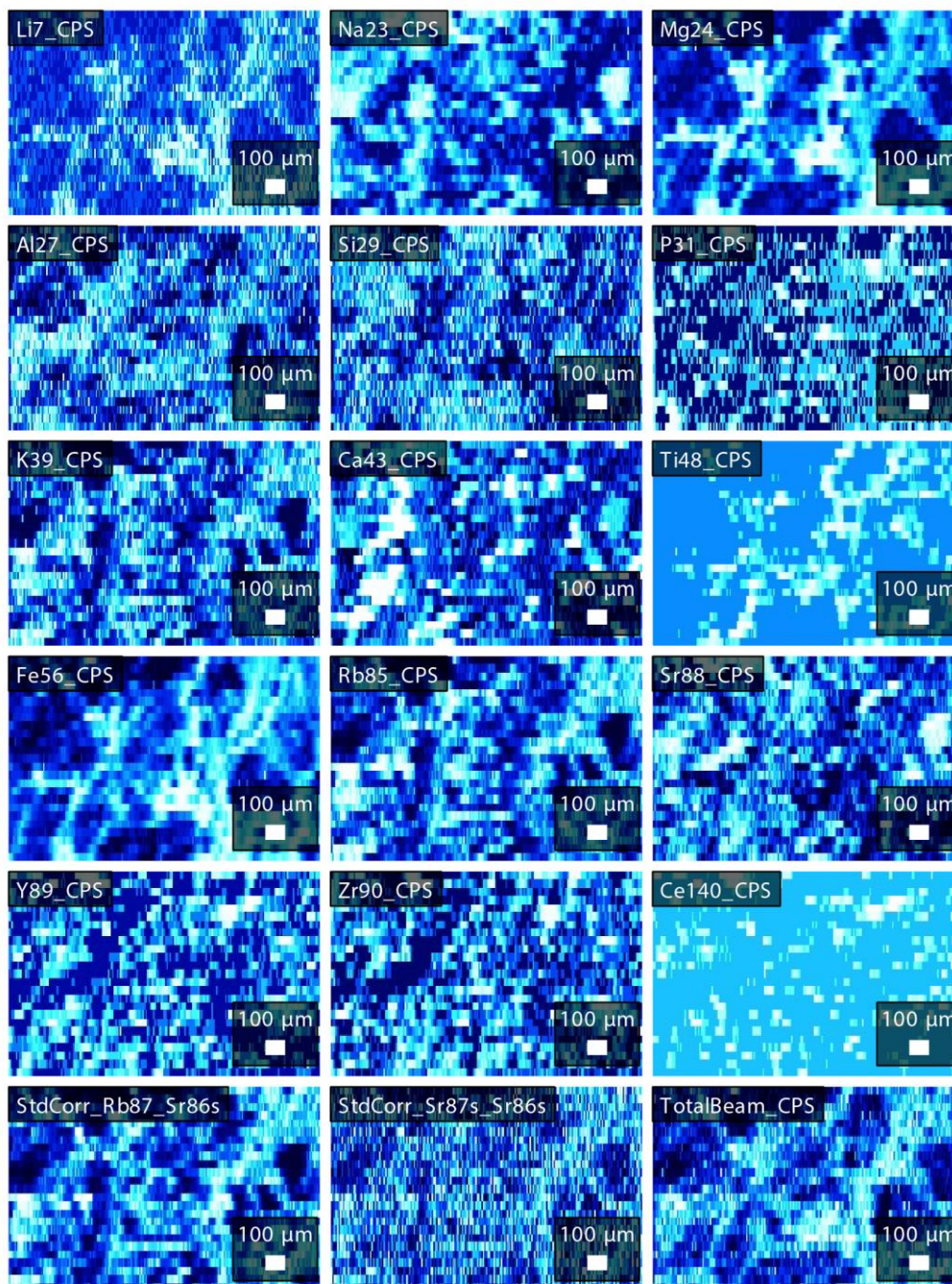
## APPENDIX 7: ELEMENTAL COMPOSITION MAPS FROM IOLITE4 FOR SAMPLE LK-172.



Elemental concentration maps for all analysed elements in the LA-ICP-MS Rb–Sr method for sample LK-172. Maps were used for the purpose of determining mineral phases in chip samples. Each map name is the element and atomic mass value for that sample. White colour responds to higher concentration of an element and blue is a lower concentration.

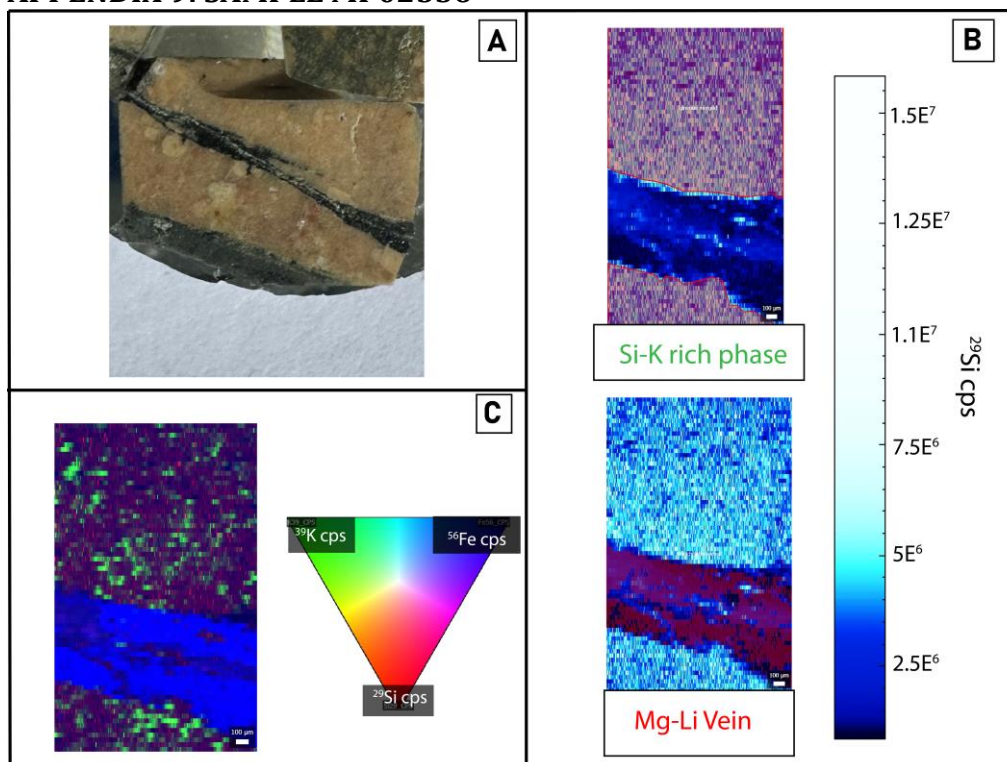


## APPENDIX 8: ELEMENTAL COMPOSITION MAPS FROM IOLITE4 FOR SAMPLE MP02-583.



Elemental concentration maps for all analysed elements in the LA-ICP-MS Rb–Sr method for sample MP02-583. Maps were used for the purpose of determining mineral phases in chip samples. Each map name is the element and atomic mass value for that sample. White colour responds to higher concentration of an element and blue is a lower concentration.

## APPENDIX 9: SAMPLE MP02556

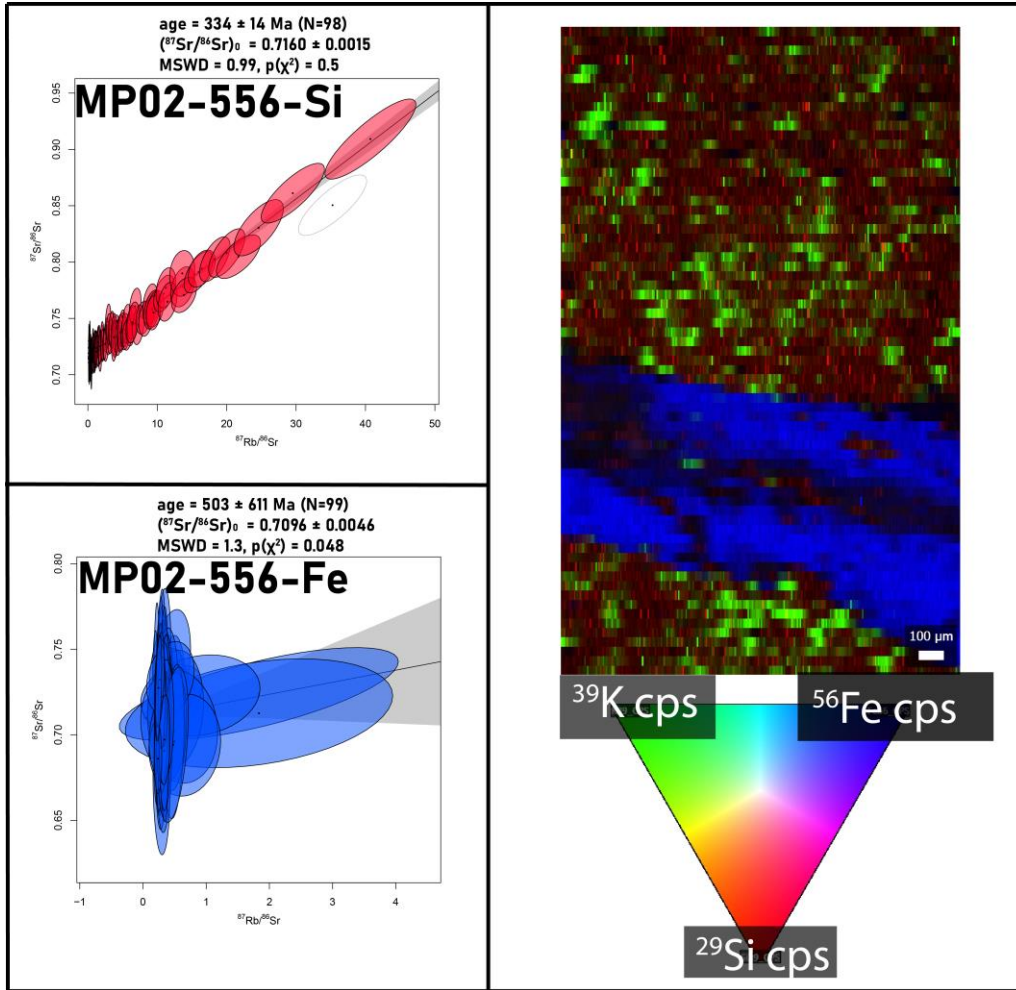


**A-** Sample MP02-556 mounted in epoxy; **B-** Two distinct pixel maps for phases (Si-K rich phase, Mg-Li vein) present in sample MP02-556 (red regions) overlain on  $^{29}\text{Si}$  concentration map (left) and  $^{29}\text{Si}$  scale (right); **C-** The two distinct phases in B compiled into one ternary diagram showing their respective spatial locations relative to each other.

LA-ICP-MS analysis of this sample revealed two clear phases within. Looking at the chip we can see the two phases, The majority of the chip is a white/salmon coloured igneous sample dominated by felsic minerals like quartz and feldspar. There is also a thin black vein cutting through this (Figure \*\*, A). These two phases were separated and geochronological analysis was run on them separately.

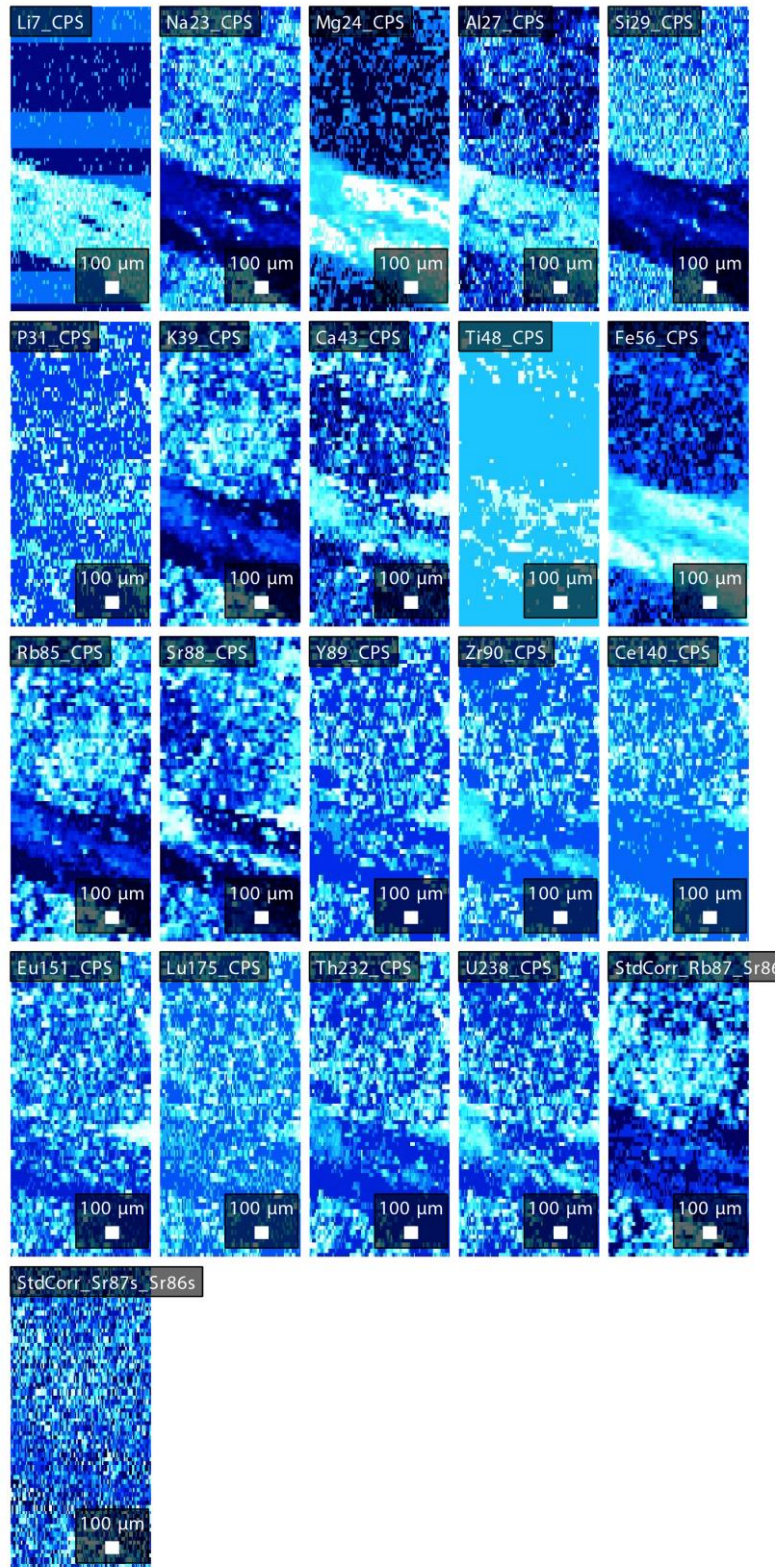
The Si-K rich phase (MP02-556-Si) returned an age of  $334 \pm 14$  Ma ( $2\sigma$  error) and an initial  $^{87}\text{Sr}/^{86}\text{Sr}$  of  $0.7160 \pm 0.0015$  from 99 analytical points (Figure \*\*).

The Fe-Li rich phase (MP02-556-Fe) returned an age of  $503 \pm 611$  Ma ( $2\sigma$  error) and an initial  $^{87}\text{Sr}/^{86}\text{Sr}$  of  $0.7096 \pm 0.0046$  from 99 analytical points (Figure \*\*).



Isochrons for phase MP02-556-Si (top left), MP02-556-Fe (bottom left) with ages and initial  $^{87}\text{Sr}/^{86}\text{Sr}$  along with associated  $2\sigma$  errors ( $2\sigma$  quoted) and mean square weighted deviation (MSWD) and (right) ternary map of their pixel regions which each isochron was analysed from. Each isoplot is colour coded to its colour in the ternary map.

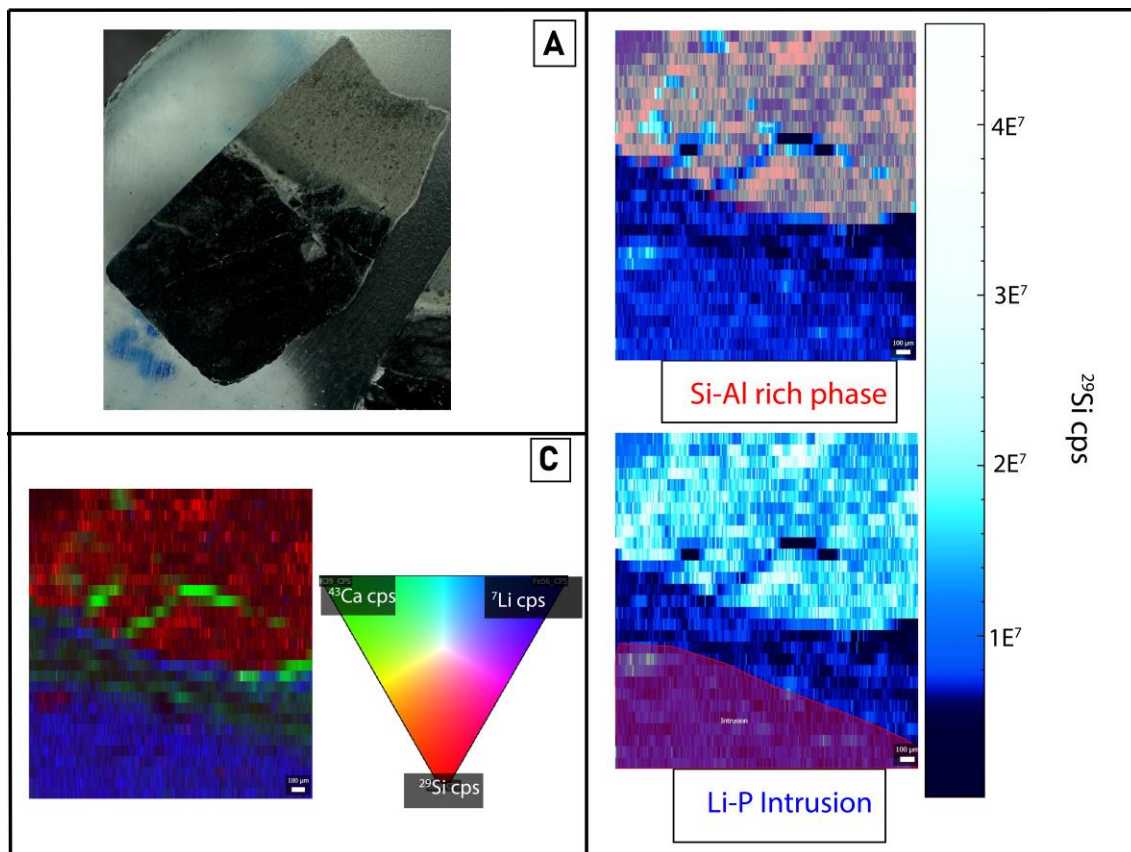




Elemental concentration maps for all analysed elements in the LA-ICP-MS Rb–Sr method for sample MP02-556. Maps were used for the purpose of determining mineral phases in chip samples. Each map name is the element and atomic mass value for that sample. White colour responds to higher concentration of an element and blue is a lower concentration.



## APPENDIX 10: SAMPLE LK12-173

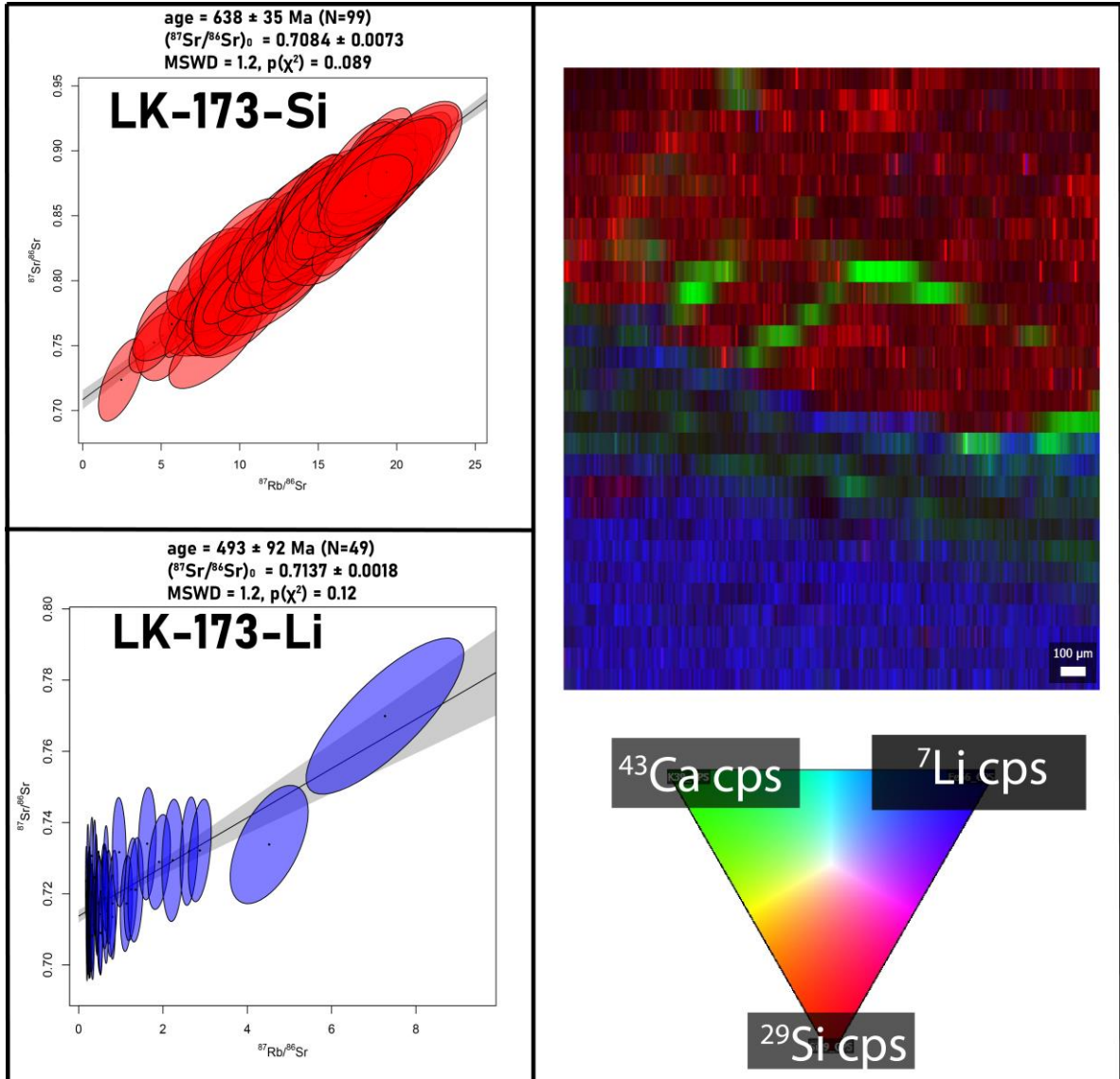


**A- Sample LK12-173 mounted in epoxy; B- Two distinct pixel maps for phases (Si-Al rich phase & Li-P intrusion) present in sample LK12-173 (red regions) overlain on  $^{29}\text{Si}$  concentration map (left) and  $^{29}\text{Si}$  scale (right); C- The two distinct phases in B compiled into one ternary diagram showing their respective spatial locations relative to each other.**

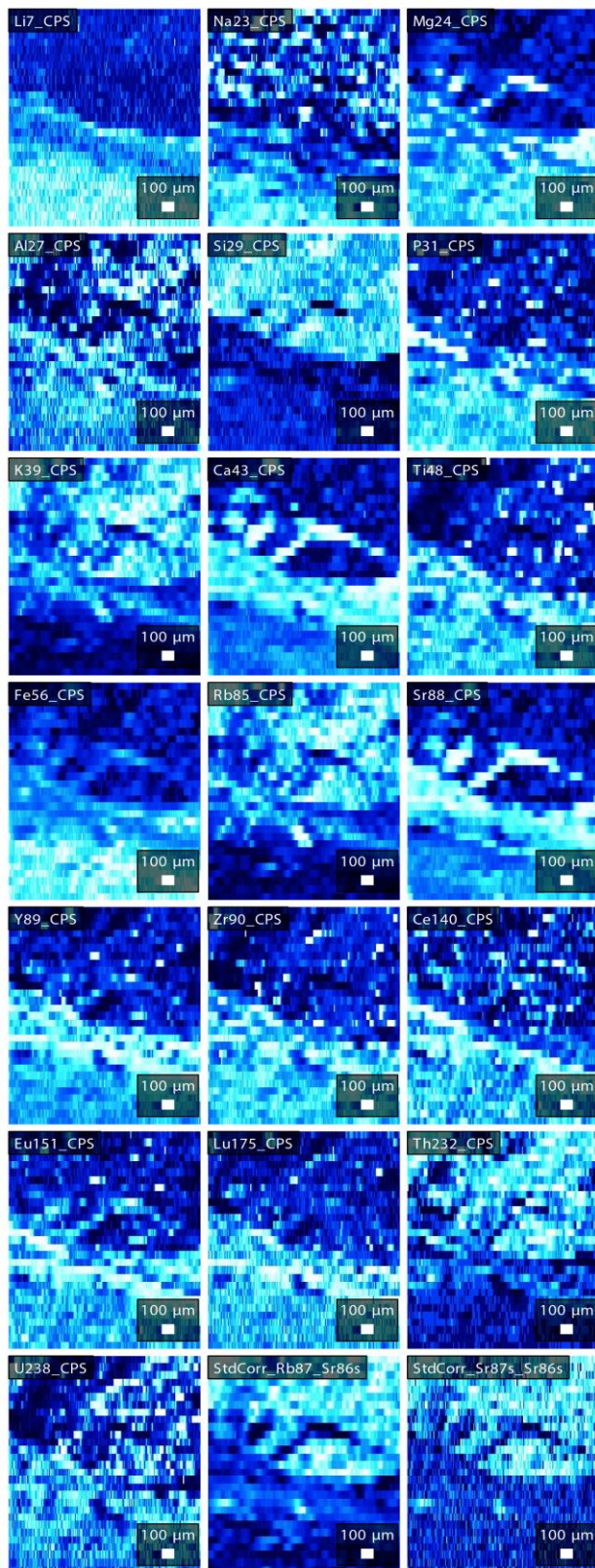
LA-ICP-MS analysis of this sample returned three clear phases in this chip. The Si-Al rich phase, a Li-P rich intrusive phase and a Ca-rich phase which sits at the contact between the two others. The Ca-rich phase has not been included in this analysis as it is a carbonate and therefore unsuitable for this technique.

The Si-Al rich phase (LK12-173-Si) returned an age of  $638 \pm 35$  Ma ( $2\sigma$  error) and an initial  $^{87}\text{Sr}/^{86}\text{Sr}$  of  $0.7084 \pm 0.0073$  from 99 analytical points (Figure \*\*).

The Li-P rich phase (LK12-173-Li) returned an age of  $493 \pm 92$  Ma ( $2\sigma$  error) and an initial  $^{87}\text{Sr}/^{86}\text{Sr}$  of  $0.7137 \pm 0.0018$  from 49 analytical points (Figure \*\*)



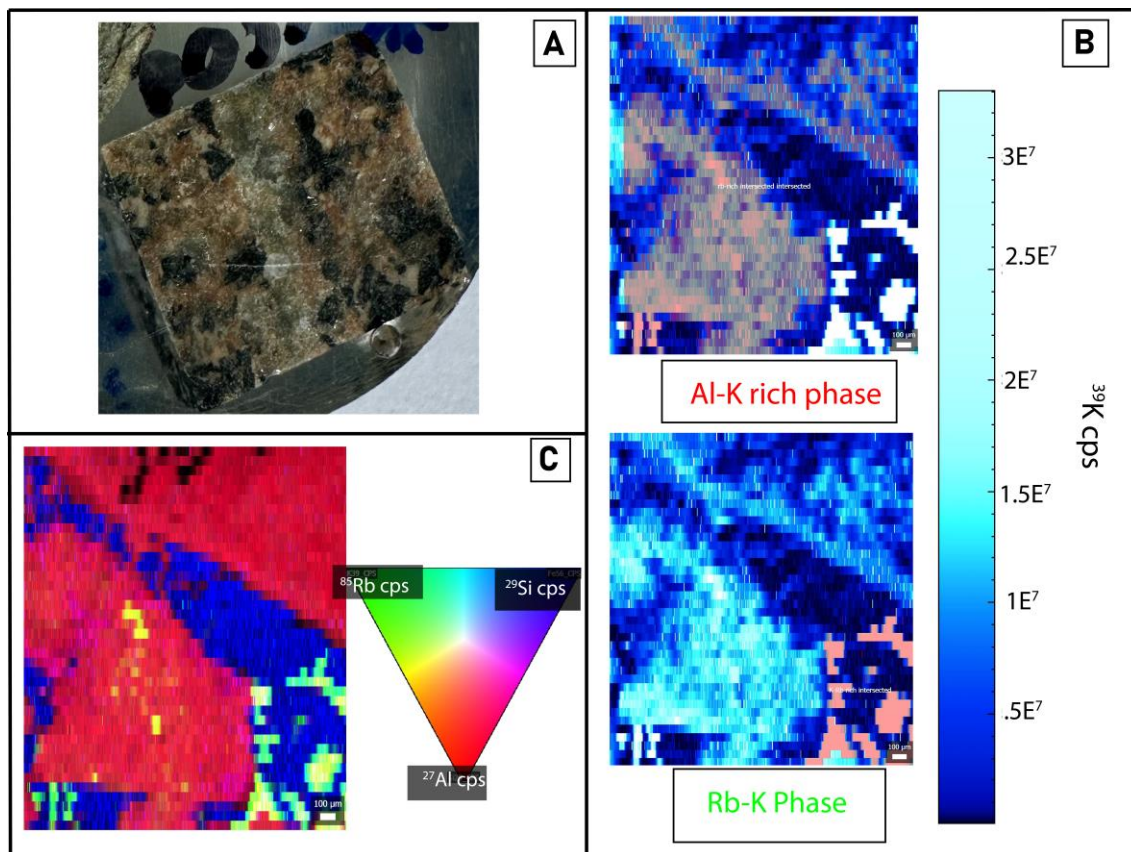
Isochrons for phase LK-173-Si (top left), LK-173-Li (bottom left) with ages and initial  $^{87}\text{Sr}/^{86}\text{Sr}$  along with associated  $2\sigma$  errors ( $2\sigma$  quoted) and mean square weighted deviation (MSWD) and (right) ternary map of their pixel regions which each isochron was analysed from. Each isochron is colour coded to its colour in the ternary map.



Elemental concentration maps for all analysed elements in the LA-ICP-MS Rb–Sr method for sample LLK-173. Maps were used for the purpose of determining mineral phases in chip samples. Each map name is the element and atomic mass value for that sample. White colour responds to higher concentration of an element and blue is a lower concentration.



## APPENDIX 11: MP03-546

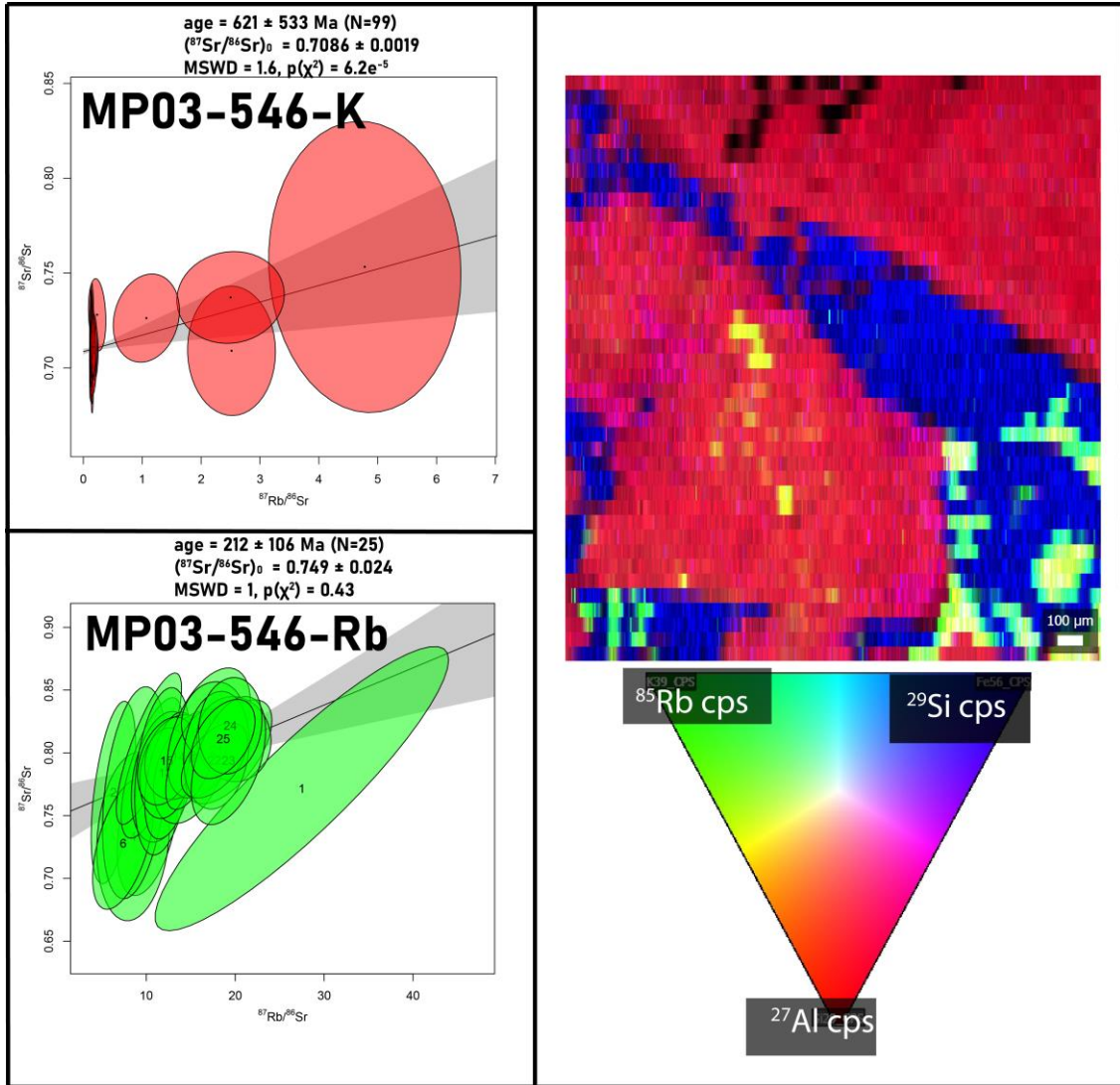


A- Sample MP03-546 mounted in epoxy; B- Two distinct pixel maps for phases (Al-K rich phase & Rb-K phase) present in sample MP03-546 (red regions) overlain on  $^{39}\text{K}$  concentration map (left) and  $^{39}\text{K}$  scale (right); C- The two distinct phases in B compiled into one ternary diagram showing their respective spatial locations relative to each other.

LA-ICP-MS analysis of this sample revealed two clear phases. Phase one is dominated by high Al and K concentrations and sits dominantly on the left of the analysed region (Figure \*\*, B). The second phase is minor and contains elevated Rb and K concentrations while compared to phase one but significantly less Fe and Na (Figure \*\*, B).

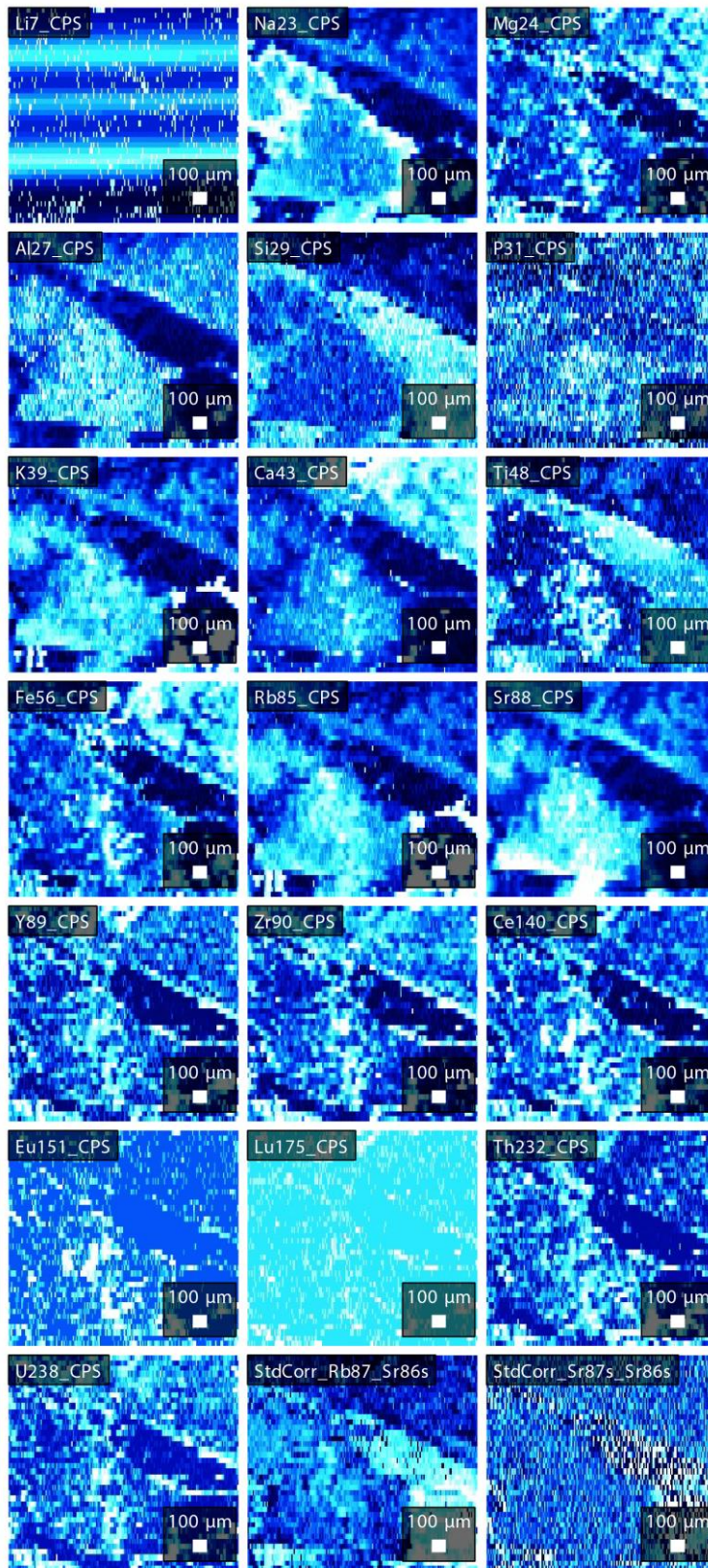
Phase one (MP03-546-K) returned an age of  $621 \pm 533$  Ma ( $2\sigma$  error) and an  $^{87}\text{Sr}/^{86}\text{Sr}$  ratio of  $0.7086 \pm 0.0019$  from 99 analytical points (Figure \*\*).

Phase two (MP03-546-Rb) returned an age of  $212 \pm 106$  Ma ( $2\sigma$  error) and an  $^{87}\text{Sr}/^{86}\text{Sr}$  ratio of  $0.749 \pm 0.024$  from 25 analytical points (Figure \*\*).



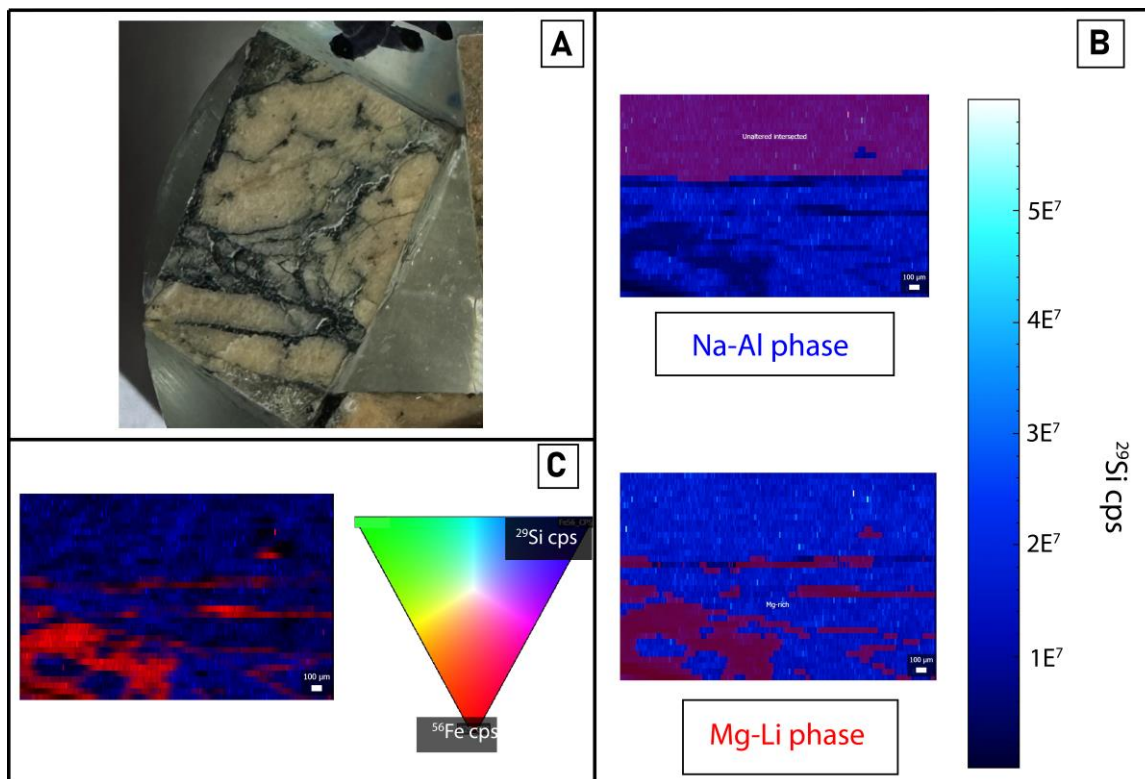
Isochrons for phase MP03-546-K (top left), MP03-546-Rb (bottom left) with ages and initial  $^{87}\text{Sr}/^{86}\text{Sr}$  along with associated  $2\sigma$  errors ( $2\sigma$  quoted) and mean square weighted deviation (MSWD) and (right) ternary map of their pixel regions which each isochron was analysed from. Each isoplot is colour coded to its colour in the ternary map.





Elemental concentration maps for all analysed elements in the LA-ICP-MS Rb–Sr method for sample LLK-173. Maps were used for the purpose of determining mineral phases in chip samples. Each map name is the element and atomic mass value for that sample. White colour responds to higher concentration of an element and blue is a lower concentration.

## APPENDIX 12: SAMPLE MP02-579



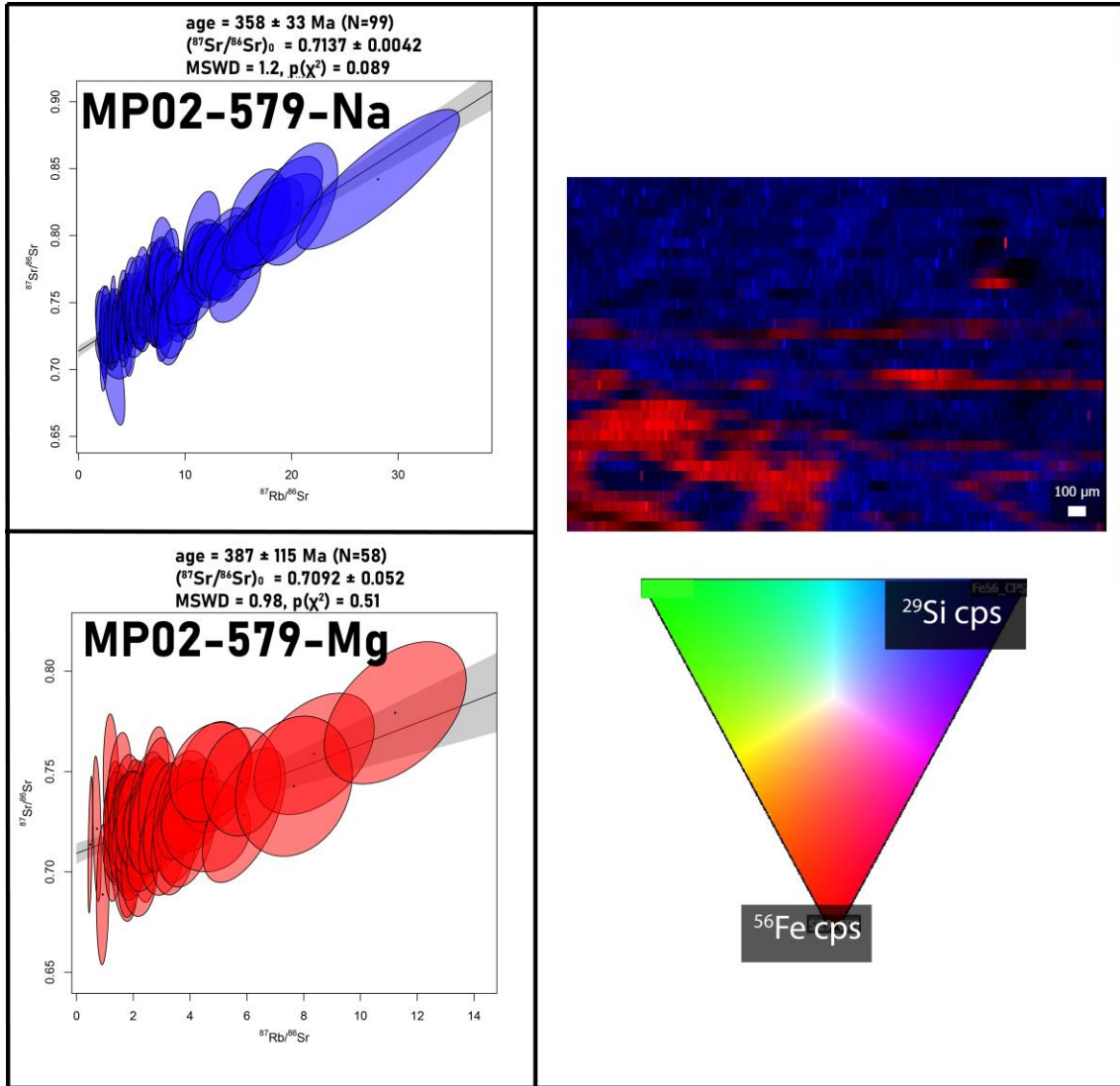
A- Sample MP02-579 mounted in epoxy; B- Two distinct pixel maps for phases (Na-Al rich phase & Mg- Li phase) present in sample MP02-579 (red regions) overlain on  $^{29}\text{Si}$  concentration map (left) and  $^{29}\text{Si}$  scale (right); C- The two distinct phases in B compiled into one ternary diagram showing their respective spatial locations relative to each other.

LA-ICP-MS analysis of this sample revealed two clear phases. Phase one is dominated by high Na and Al concentrations and dominates the analysed region (Figure \*\*, B). The second phase is minor and vein-like and contains elevated Mg, Li & Fe concentrations while compared to phase one (Figure \*\*, B).

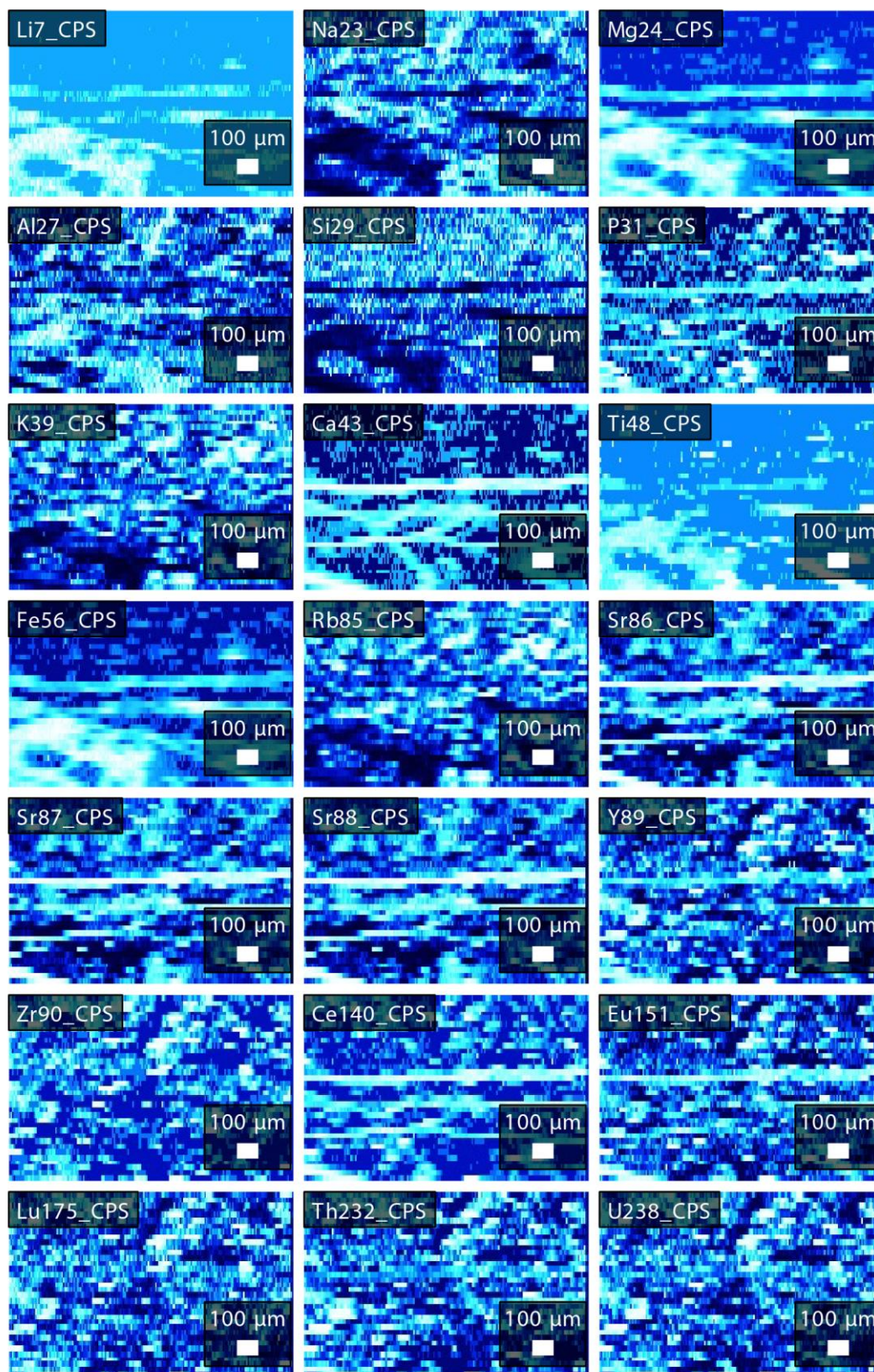
Phase one (MP02-579-Na) returned an age of  $358 \pm 33$  Ma ( $2\sigma$  error) and an initial  $^{87}\text{Sr}/^{86}\text{Sr}$  of  $0.7137 \pm 0.0042$  from 99 analytical points (figure \*\*).

Phase two (MP02-579-Mg) returned an age of  $387 \pm 115$  Ma ( $2\sigma$  error) and an initial  $^{87}\text{Sr}/^{86}\text{Sr}$  of  $0.7092 \pm 0.0052$  from 58 analytical points (Figure \*\*).





Isochrons for phase MP02-579-Na (top left), MP02-579-Mg (bottom left) with ages and initial  $^{87}\text{Sr}/^{86}\text{Sr}$  along with associated  $2\sigma$  errors ( $2\sigma$  quoted) and mean square weighted deviation (MSWD) and (right) ternary map of their pixel regions which each isochron was analysed from. Each isoplot is colour coded to its colour in the ternary map.



Elemental concentration maps for all analysed elements in the LA-ICP-MS Rb–Sr method for sample MP02-579. Maps were used for the purpose of determining mineral phases in chip samples. Each map name is the element and atomic mass value for that sample. White colour responds to higher concentration of an element and blue is a lower concentration.

**APPENDIX 13: PARAMETERS FOR DATA ACQUISITION OF RB–SR SHALE & ILLITE LA-ICP-MS SPOT ANALYSIS.**

Sample ID	Sample Target	Date of session	Spot Size (µm)	# of spots
LLK11-323	Illite	05/08/2024	67	60
LLK11-369	Illite	05/08/2024	67	65
LLK12-186	Illite	05/08/2024	67	60
LLK14-361	Illite	05/08/2024	67	60
LLK14-379	Illite	05/08/2024	67	60
MP02556	Mica	05/08/2024	67	80
MP02628	Mica	05/08/2024	67	59
MP03493	Mica	05/08/2024	67	60
MP03548	Mica	05/08/2024	67	60

# APPENDIX 14: SOLUTION ICP-MS GEOCHEMICAL DATA

Elements (ppm)	LK12A	LK12B	MP2A	MP2B	MP3A	MP3B	JT1 (USGS G2)	USGS values (Flanagan, 1976)
Li	35.5677	61.9219	7.6745	15.6264	31.4064	14.7099	31.5117	33.6
Be	1.967	2.4808	3.076	3.3048	2.6	2.4134	2.8608	2.486
Na	8423.1527	10334.9015	28468.403	18973.1346	16836.8593	16251.238	29922.6747	
Mg	42271.31062	31780.1307	1670.2773	1626.492	13919.0849	13675.1816	4746.2371	
Al	62705.5544	53507.5752	72873.5148	83875.6126	93296.6539	91258.4258	101981.5081	
P	1935.6181	2269.0829	244.1467	202.6064	709.5296	711.4409	814.4195	
K	4243.9063	13523.7482	43555.9502	46254.2824	30126.4982	30111.656	50968.6181	
Ca	62964.1801	41148.6865	7147.2994	20195.4057	39332.3219	34881.6791	16683.7496	
Sc	16.456	11.8855	10.1418	11.8417	21.2636	21.1734	4.7336	3.66
Ti	8937.4028	10143.4314	1364.1771	1380.0209	3433.5083	3533.3888	3022.9607	
V	199.7527	225.4343	5.6217	3.9615	111.3374	111.4445	30.3812	35.12
Cr	234.4081	212.3362	1.3256	0.6722	41.3687	30.6049	6.7113	7.88
Mn	920.6204	1068.4938	250.5638	230.5135	687.0857	773.0966	231.4935	
Fe	56293.4532	77812.6008	13392.2486	15578.4205	37633.1177	39085.1855	17076.2623	
Co	41.4336	36.8915	26.598	43.3868	31.2588	37.3692	3.9456	4.478
Ni	117.8729	99.3349	0.5779	0.5877	9.5357	9.641	1.7796	3.46
Cu	41.1262	37.5144	12.9069	10.5837	14.8752	12.2379	8.0991	10.98
Zn	61.6342	36.8954	43.702	33.0265	64.978	66.7295	78.7215	83.5
Ga	13.8343	16.0293	12.9601	15.2494	16.3856	16.1103	21.6124	23.32
Rb	12.2742	49.9574	125.8896	134.559	102.8944	90.6363	165.1225	168.5
Sr	336.5344	103.391	117.1976	195.7986	216.8866	211.2115	467.7368	474.9
Y	18.1976	18.5393	26.2778	27.9703	20.2517	20.5247	8.7805	9.88
Zr	141.0835	177.6584	278.4706	305.7485	149.9386	148.2102	339.7257	319
Nb	12.4683	13.5377	11.1939	11.39	9.2426	9.6698	10.0849	12.02
Mo	0.7376	0.736	0.3743	0.8189	0.8265	0.4748	0.239	0.38
Cd	0.08	0.0429	0.0756	0.069	0.0648	0.0648	0.0583	0.08



Sn	1.1738	1.3978	1.4526	2.0517	3.3108	2.8843	1.6326	1.72
Sb	0.1942	0.347	1.0483	1.2687	0.0538	0.1547	0.0502	0.058
Cs	12.1356	5.1927	2.2769	3.5846	5.9307	4.5865	1.3439	1.357
Ba	243.6469	120.0071	657.5667	1154.5365	557.0279	626.9163	1956.8329	1860
La	26.5016	28.1526	40.8557	43.6908	34.7182	41.8356	93.3544	88.4
Ce	63.6754	70.8996	78.0558	86.5453	70.9407	80.8666	170.7051	161.2
Pr	7.7577	8.8724	9.0319	9.6725	7.6186	8.4713	16.4386	16.88
Nd	31.4377	36.5601	33.6835	36.5586	27.9719	30.4742	53.2173	53.81
Sm	6.1654	7.1773	7.0705	7.5373	5.6446	5.9157	7.6867	7.19
Eu	1.6138	1.7185	1.0483	1.225	1.0567	1.0525	1.3107	1.414
Gd	5.3077	6.0027	6.1146	6.6251	4.875	5.0612	4.9147	4.23
Tb	0.761	0.85	0.9587	1.0045	0.7387	0.7372	0.5325	0.495
Dy	4.2969	4.8612	5.6684	5.8635	4.2938	4.2674	2.2592	2.278
Ho	0.8323	0.9943	1.1454	1.1783	0.8384	0.8516	0.3756	0.3725
Er	2.3699	2.8902	3.4008	3.4874	2.4973	2.522	1.0534	0.927
Tm	0.321	0.3987	0.491	0.4896	0.3519	0.3575	0.1273	0.1232
Yb	2.0314	2.5549	3.1964	3.2475	2.3149	2.3682	0.7782	0.722
Lu	0.2937	0.3831	0.4817	0.5051	0.3559	0.3547	0.1085	0.1019
Hf	3.5857	4.2734	8.1002	8.4368	4.4483	4.4211	8.9033	7.78
Ta	1.0674	0.9368	1.2341	1.5572	1.2791	1.4734	0.6222	0.834
Tl	0.2966	0.4192	1.0689	0.7509	0.7317	0.5978	0.8786	0.884
Pb	8.1616	6.1382	26.8799	25.0618	21.0123	21.1907	30.7533	30
Bi	0.0381	0.0507	0.2007	0.0408	5.2877	0.0903	0.0377	0.034
Th	2.087	1.8199	17.3458	18.0675	14.3867	15.7681	25.7758	24.54
U	0.7025	1.3764	6.052	4.2179	1.951	2.621	1.8845	1.964

# APPENDIX 15: RAW DATA FROM RB–SR LA-ICP-MS SPOT ANALYSIS OF SHALES AND INTRUSIONS

ALnum	Sample	Analysis	Rb87Sr86	Rb87Sr86_2SE	Sr87Sr86	Sr87Sr86_2SE	Rho_Rb87Sr86_Sr87Sr86]	Comment	Corrected	Corrected 2se	omit
8	LLK11323	LLK11323-001	4.792864788622850	0.221958533	0.74876048	0.012958013	0.136252657	zr inc	4.357730409	0.204090405	
9	LLK11323	LLK11323-002	4.364070815633300	0.295881448	0.73710656	0.015644067	0.45464903	zr inc	3.967865763	0.270443145	
10	LLK11323	LLK11323-003	3.204356966193770	0.107663379	0.73272036	0.008507302	0.157315567	high y	2.913439959	0.099982173	
11	LLK11323	LLK11323-004	9.376589253331270	0.351610669	0.76651328	0.017381384	0.538483256	zr inc	8.525307917	0.325188512	
12	LLK11323	LLK11323-005	3.383587499569820	0.177085779	0.73323387	0.01075002	0.475334628	zr/y def	3.076398519	0.162436408	
13	LLK11323	LLK11323-006	2.101348414412910	0.161960573	0.73022712	0.006966141	0.185927333		1.910571295	0.147860093	
14	LLK11323	LLK11323-007	0.935996217	0.02058685	0.714843	0.004045376	0.138844389		0.851019037	0.019639199	
15	LLK11323	LLK11323-008	4.415493334191120	0.066043508	0.74673602	0.010141847	0.048810357		4.014619737	0.066273716	
22	LLK11323	LLK11323-009	7.761676817823520	0.50224261	0.77411212	0.014712322	0.237529603		7.057010074	0.459298299	
23	LLK11323	LLK11323-011	0.714422361	0.085054478	0.72137115	0.005800878	-0.008677774		0.649561418	0.077465566	
24	LLK11323	LLK11323-012	2.700489579159970	0.164835379	0.73595101	0.008891585	0.263361565	zr peak	2.45531766	0.150848592	
25	LLK11323	LLK11323-013	3.972853068385540	0.080292857	0.74064808	0.008147382	0.420255478	zr/ce peak	3.612165874	0.077241081	
26	LLK11323	LLK11323-014	8.404525751609730	0.241471217	0.77170965	0.020900913	0.602662223	zr peak	7.64149607	0.225944764	
27	LLK11323	LLK11323-015	4.183722304611360	0.078606053	0.73970238	0.010873009	0.232848909		3.803890724	0.076249565	
28	LLK11323	LLK11323-016	0.348353205	0.024606715	0.71707372	0.005947732	0.054447056	zr inc	0.316726931	0.022481859	
29	LLK11323	LLK11323-017	0.47332625	0.015582812	0.71247994	0.009630109	0.188247806	zr peak	0.430353929	0.014483517	
30	LLK11323	LLK11323-018	6.533930832604330	0.153681657	0.75700439	0.016530464	0.241380329	zr inc	5.940728633	0.145761686	
31	LLK11323	LLK11323-019	5.031445678067140	0.096885294	0.75782282	0.009443938	0.162494385	y drop	4.574651028	0.093706733	
32	LLK11323	LLK11323-020	3.080942180288790	0.195410985	0.73874393	0.009809029	0.235485321	zr inc	2.801229749	0.178744383	
33	LLK11323	LLK11323-021	3.223271384065880	0.131330163	0.73001105	0.008781015	0.186608245	zr peaks	2.930637176	0.121149237	
34	LLK11323	LLK11323-022	7.911807788860590	0.311720718	0.76891332	0.012394382	0.510799997	zr peak	7.193510962	0.28784057	
35	LLK11323	LLK11323-023	2.241069087162260	0.065762447	0.72908368	0.010740064	0.192708281	P peak	2.037607014	0.061462906	
36	LLK11323	LLK11323-024	7.879481919224020	0.325314189	0.76852154	0.009858034	0.152595492	ree peak	7.164119892	0.299983556	
37	LLK11323	LLK11323-025	4.262434954616990	0.16533861	0.74301291	0.006859671	0.21107849	zr peak	3.875457214	0.152746129	
38	LLK11323	LLK11323-026	9.427339839696700	0.138268175	0.77818081	0.009186461	0.303394025	zr peak	8.571450961	0.139246228	
39	LLK11323	LLK11323-027	7.823428680236400	0.251265689	0.7604555	0.009037256	0.425074986	zr peaks	7.113155611	0.233795212	
40	LLK11323	LLK11323-028	3.953757834770700	0.100366437	0.74241171	0.008198437	0.102775186	zr drop	3.594804258	0.094646539	
41	LLK11323	LLK11323-029	10.349831309316400	0.375066503	0.78376856	0.012556931	0.232871793	y peak	9.410191319	0.347292997	
42	LLK11323	LLK11323-030	4.346539754161660	0.082692551	0.74373589	0.013995741	0.564612683	y drop	3.951926311	0.080093184	
43	LLK11323	LLK11323-031	2.328907028007460	0.056993578	0.72435102	0.012750036	0.192296888	zr peaks	2.117470328	0.053889072	

44	LLK11323	LLK11323-032	2.361648880083600	0.073556175	0.73234327	0.006261291	0.13795001		2.147239615	0.068539634
45	LLK11323	LLK11323-033	12.756520197442600	0.268307212	0.79322675	0.016507875	0.503130099	z/y peak	11.59838185	0.257051004
46	LLK11323	LLK11323-034	4.437925628432220	0.118754961	0.75507889	0.013505641	0.083033767	zr peak	4.035015449	0.111591991
49	LLK11323	LLK11323-035	5.979236326091040	0.14428339	0.7594626	0.012453926	-0.133447299	y peaks	5.436393704	0.136570524
50	LLK11323	LLK11323-036	5.289894179894560	0.069461631	0.75422603	0.013344991	0.286409403	z/y variance	4.80963552	0.071536274
52	LLK11323	LLK11323-039	2.454690275641160	0.058231406	0.729294	0.015542321	0.343292031	y drop	2.231833972	0.055192491
53	LLK11323	LLK11323-040	5.536192600306240	0.258791515	0.75895678	0.01317628	0.207649817	y drop z peak/y drop	5.033573011	0.237909193
54	LLK11323	LLK11323-041	3.439528020153110	0.179921786	0.73326334	0.010922727	0.232047764		3.127260315	0.16503928
55	LLK11323	LLK11323-042	7.292037835013830	0.226546596	0.75838033	0.010052581	0.202617741	y drop	6.630008653	0.211121646
56	LLK11323	LLK11323-043	8.898780568011970	0.45389358	0.76570802	0.016502689	0.493798364	zr peak	8.090878503	0.416537881
57	LLK11323	LLK11323-044	6.192070584202400	0.110651983	0.76012436	0.010486608	0.281106144	y drop	5.629905176	0.108019931
58	LLK11323	LLK11323-045	1.593001942040690	0.021574802	0.72524867	0.009311834	0.200613692		1.448376558	0.022071697
59	LLK11323	LLK11323-046	3.449205455056650	0.134597082	0.73995456	0.009178482	0.114016208	z peak	3.136059155	0.124322682
60	LLK11323	LLK11323-047	4.992676687823950	0.395382387	0.74437074	0.01229248	0.22653764	Y drop	4.539401795	0.360882317
61	LLK11323	LLK11323-048	4.187457466125920	0.174378102	0.74298962	0.00757408	0.322838945		3.807286778	0.160761952
66	LLK11323	LLK11323-049	5.965049054821770	0.168034167	0.75381426	0.012402923	0.384453641	y spike	5.423494467	0.157406183
67	LLK11323	LLK11323-050	6.528113604568660	0.247382541	0.75602773	0.008772184	0.307351758		5.935439539	0.228712899
68	LLK11323	LLK11323-051	2.588815427460200	0.099052	0.72845254	0.010737591	0.190659878	z peak	2.353782176	0.091547973
69	LLK11323	LLK11323-052	7.735812171839510	0.130828756	0.76772954	0.013845821	0.280638162	y peak	7.033493626	0.128698999
70	LLK11323	LLK11323-053	2.288138686773030	0.049475771	0.72843406	0.010539068	0.179654845	z/y drop	2.080403261	0.047273267
72	LLK11323	LLK11323-055	2.480340906764390	0.102335803	0.739206	0.014287531	0.317288784	ree drops	2.255155835	0.094369162
73	LLK11323	LLK11323-056	4.223174983108750	0.141253712	0.74030253	0.010577206	0.472823107	z spikes	3.839761575	0.131200735
74	LLK11323	LLK11323-057	4.558198565463160	0.06229216	0.74779093	0.007717695	0.291574621	y drop	4.144369052	0.063607242
75	LLK11323	LLK11323-058	3.134089047262290	0.082183498	0.74216815	0.012441983	0.216248706	ree drops	2.849551521	0.07732822
76	LLK11323	LLK11323-059	4.067650400839680	0.145439642	0.73504034	0.013379631	0.063699856	zr inc	3.698356751	0.134735598
77	LLK11323	LLK11323-060	2.238629521218850	0.057452132	0.72887611	0.007440167	0.308501428		2.035388931	0.054136689
288	LLK11369	LLK11369-001	3.754933727763620	0.174620478	0.74246893	0.009151351	0.468723483	P peak	3.414030984	0.160548285
289	LLK11369	LLK11369-002	5.556850532195630	0.601836469	0.75245896	0.009709756	0.524934279	y drop	5.052355452	0.548333997
290	LLK11369	LLK11369-003	4.776344298467190	0.097518653	0.75427169	0.009679585	0.255144086	Y peaks	4.342709781	0.093711294
291	LLK11369	LLK11369-004	5.066229275436510	0.51794884	0.75281818	0.0085445	0.373242752	y peak	4.606276694	0.47202337
292	LLK11369	LLK11369-005	5.646373366400730	0.858745958	0.75115172	0.011029596	0.456290069	y peak/zr dip	5.133750691	0.78160534
293	LLK11369	LLK11369-006	6.337429757481310	0.17112808	0.7646101	0.012437695	0.360542044	P peak	5.762067488	0.160713928



Matthew Robert Barnett  
Constraining the hidden Delamerian margin

294	LLK11369	LLK11369-007	3.567410591485390	0.194576182	0.73160329	0.009230662	0.288735663	z peak	3.243532689	0.178356081
295	LLK11369	LLK11369-008	2.887105163723120	0.143897649	0.73237038	0.007425319	0.28813967	y peak	2.624990798	0.132112261
300	LLK11369	LLK11369-009	4.143337034849940	0.646433595	0.74004585	0.00923047	0.475514638	Ree spike	3.76717195	0.58833406
301	LLK11369	LLK11369-010	6.914325960654680	0.196873971	0.75986785	0.011815459	0.477199462	Y peaks	6.286588466	0.18430857
304	LLK11369	LLK11369-011	12.798782013775700	0.489774171	0.80932594	0.010891751	0.662634182	Z inc	11.6368068	0.452667445
305	LLK11369	LLK11369-012	2.969719924785890	0.407730573	0.73735305	0.007864968	0.441373593	zr peaks	2.700105134	0.371193084
306	LLK11369	LLK11369-014	4.971953752812930	0.542872917	0.75444776	0.011937741	-0.01609554	Y peaks	4.520560253	0.494595746
307	LLK11369	LLK11369-015	2.780905451383610	0.198576031	0.73317235	0.006876801	0.307436916	Y spike	2.52843274	0.181409613
308	LLK11369	LLK11369-016	5.668463016166750	0.223969543	0.75196534	0.011770761	0.160814843	Y peak	5.153834867	0.206793939
309	LLK11369	LLK11369-017	8.527303315080720	0.60404817	0.7855694	0.013283435	0.205996806	Z spikes	7.75312691	0.551871928
310	LLK11369	LLK11369-018	10.501914309662600	0.751612231	0.79287157	0.016428609	0.028091331	Z peak	9.548467016	0.686622445
311	LLK11369	LLK11369-019	3.635412406082760	0.172299329	0.74545858	0.009319601	0.432448328	Z peak	3.305360758	0.15834912
312	LLK11369	LLK11369-020	2.956553294415930	0.248246508	0.73644412	0.009024994	0.164519624	zr inc	2.688133875	0.226488513
313	LLK11369	LLK11369-021	4.950867844189240	0.632278056	0.76103789	0.01031516	0.50588731	Y spikes	4.501388691	0.575734183
314	LLK11369	LLK11369-022	3.856414814629740	0.118638334	0.7422717	0.011779913	0.446430265		3.506298811	0.110613354
315	LLK11369	LLK11369-023	2.530107559270740	0.107087417	0.72649032	0.00892408	0.201874004	Z/P peaks Z	2.300404275	0.09868238
316	LLK11369	LLK11369-024	5.233691252956720	0.379085453	0.74324669	0.01098007	0.132956196	fluctuations	4.758535142	0.34626831
317	LLK11369	LLK11369-025	1.631012513352670	0.156874656	0.73135097	0.008141217	0.040446427	Y spike	1.482936227	0.143008021
318	LLK11369	LLK11369-026	1.932365636658530	0.214003049	0.73553716	0.007097415	0.079924444	Y peak	1.756930118	0.194960847
319	LLK11369	LLK11369-027	2.435023215069350	0.093269989	0.72935198	0.007868829	-0.156149028	Y/Zr peak	2.213952444	0.086200949
320	LLK11369	LLK11369-028	3.775197035574590	0.26810325	0.73821685	0.009202932	0.39410269	Z inc	3.432454628	0.244939155
321	LLK11369	LLK11369-029	2.199621462892730	0.156028556	0.73137036	0.006798044	0.133132958	Y spike	1.999922335	0.142549298
322	LLK11369	LLK11369-030	3.532602868313280	0.209752344	0.73608654	0.009130815	0.32929513	Y dip	3.211885088	0.192024677
323	LLK11369	LLK11369-031	2.000838098934330	0.137620911	0.73465693	0.006693404	0.329810597	Z inc	1.819186105	0.125770266
324	LLK11369	LLK11369-032	1.060871492832920	0.056496062	0.71948347	0.005349502	0.214390385	P spike	0.964557142	0.051806943
325	LLK11369	LLK11369-033	1.439710234604930	0.019522816	0.72745074	0.006954703	0.172987299	Zr spikes	1.309001891	0.019967269
327	LLK11369	LLK11369-035	2.441333724418680	0.293117613	0.73406068	0.007346383	0.312339762	Y spike	2.219690035	0.266956766
328	LLK11369	LLK11369-036	2.772972930888570	0.153121094	0.73449956	0.008832779	0.153560339	Ree spike Zr	2.521220397	0.140329158
329	LLK11369	LLK11369-037	0.605301001	0.034959117	0.72242492	0.008465528	0.042109161	fluctuation	0.550346963	0.032016908
330	LLK11369	LLK11369-038	3.380622142814290	0.188750886	0.73955598	0.007449451	0.30911915	Y peaks P peak/ Y peak	3.073702381	0.172952585
331	LLK11369	LLK11369-039	8.202997189128250	0.283875492	0.7768759	0.013787467	0.461256724		7.458263873	0.263308998
332	LLK11369	LLK11369-040	3.057202943609360	0.167476171	0.7344955	0.008462883	0.072749518	Zr inc	2.779645749	0.153504412

Matthew Robert Barnett  
Constraining the hidden Delamerian margin

335	LLK11369	LLK11369-041	8.460480403657390	0.689312128	0.7683352	0.009405852	0.311245663	Zr spikes	7.692370713	0.629030328	
336	LLK11369	LLK11369-042	2.282512416246430	0.445969413	0.723647	0.008093867	0.572345576	Z peak	2.075287788	0.405739838	
337	LLK11369	LLK11369-043	2.155046595082890	0.118998439	0.72673503	0.007855018	0.114417863	Y peak	1.959394328	0.109057173	
338	LLK11369	LLK11369-044	1.745592425436490	0.072125994	0.73091766	0.008254173	0.302602456	Zr fluctuation	1.587113664	0.06650843	
339	LLK11369	LLK11369-045	4.418988756764860	0.209373365	0.74811913	0.00800803	0.23769303	Z spike/ Y spike	4.017797817	0.192422697	
340	LLK11369	LLK11369-046	4.941922619071430	0.075175561	0.74757564	0.010210002	0.587940268	Ce spike	4.493255585	0.075213083	
341	LLK11369	LLK11369-047	1.361208214877030	0.078733454	0.72167073	0.006745552	0.093005012	Ree spike	1.237626909	0.07210559	
342	LLK11369	LLK11369-048	2.343600758797390	0.055187687	0.72909621	0.009338689	0.224852481	Y spike	2.130830045	0.052338607	
347	LLK11369	LLK11369-049	1.640645545396320	0.037735809	0.72171627	0.009879696	0.20901231	Zr inc	1.491694696	0.035857363	
349	LLK11369	LLK11369-051	2.098830514728920	0.04228496	0.73449407	0.007876349	0.039224359	Ree spike	1.90828199	0.040691484	
351	LLK11369	LLK11369-053	2.552004258446940	0.183678156	0.74208333	0.013394916	-0.049635768	Y spike	2.320313018	0.167787139	
352	LLK11369	LLK11369-054	3.909710012341370	0.244111228	0.73561925	0.008654321	0.38782115	P and Ree spike	3.554755447	0.223333685	
353	LLK11369	LLK11369-055	2.326050418711040	0.316729088	0.7362351	0.009352826	0.457831969	Mg drop	2.114873065	0.288352614	
354	LLK11369	LLK11369-056	3.577655568925430	0.19913981	0.74307115	0.006523367	0.132674156	Na fluctuation	3.252847546	0.182480621	
355	LLK11369	LLK11369-057	7.541483815922130	0.465685749	0.75679884	0.011072678	0.388270684	Y spike	6.856807944	0.426107823	
356	LLK11369	LLK11369-058	3.282723245169500	0.504242573	0.72899598	0.00779709	0.151005575	P spike	2.984691524	0.45893728	
357	LLK11369	LLK11369-059	6.953315248440570	0.419548009	0.76492221	0.009959301	0.488849814	Z spike	6.322037996	0.384006093	
358	LLK11369	LLK11369-060	8.139993399152730	0.301664895	0.76814218	0.011286887	0.329958801	Z/Y spike	7.400980068	0.279107492	
359	LLK11369	LLK11369-061	10.925541487891300	0.371855397	0.78852084	0.01273881	0.281324559	Y spike	9.93363395	0.345143182	
360	LLK11369	LLK11369-062	8.074584681588040	0.650101864	0.76984833	0.01264935	0.731688521	Z spike	7.341509674	0.593301133	
361	LLK11369	LLK11369-063	7.497943878031830	0.270259681	0.77182841	0.012594805	0.355715903	Zr/Y increase	6.817220908	0.250295552	
362	LLK11369	LLK11369-064	1.812191709631800	0.145170373	0.7168186	0.008151006	0.334422358	P increase	1.647666535	0.132491551	
363	LLK11369	LLK11369-065	3.970629970954340	0.258978588	0.7415251	0.012020409	0.393533679	Ree spike	3.610144607	0.236813113	
620	LLK12_186	LLK12_186-001	15.643990525349600	0.601250124	0.81590997	0.01809739	0.365652186	Ree drop	14.22370466	0.55562039	x
621	LLK12_186	LLK12_186-002	24.517640374873200	1.001948189308100	0.9026872	0.02214837	0.476378295	Ree spikes	22.29173401	0.924196841	
622	LLK12_186	LLK12_186-003	18.188389319623700	1.019251423891320	0.86183891	0.017249147	0.452533485	P spike	16.5371027	0.933888215	
627	LLK12_186	LLK12_186-004	28.657938834220000	0.862217565	0.97208409	0.026937259	0.599485933	Z spike	26.05614325	0.804792056	x
628	LLK12_186	LLK12_186-005	19.232832857046600	0.351081569	0.8816817	0.018114769	0.349147519	P peak	17.48672335	0.341782703	
629	LLK12_186	LLK12_186-006	15.773792278794000	0.671921218	0.83892577	0.013456221	0.545685189		14.34172198	0.61907917	
630	LLK12_186	LLK12_186-007	23.679777074337700	0.67834489	0.88882291	0.01676331	0.229627583	Ree spike	21.52993861	0.634832378	
631	LLK12_186	LLK12_186-008	19.475224192809600	1.226007576048770	0.85027634	0.021192131	0.502346576	Ree spike	17.70710847	1.121542878	x

Matthew Robert Barnett  
Constraining the hidden Delamerian margin

632	LLK12_186	LLK12_186-009	21.472006216032400	0.445961719	0.88297314	0.018943034	0.608930756	Ree spikes	19.52260674	0.427794021	
633	LLK12_186	LLK12_186-010	14.965073879925900	0.65906519	0.84444728	0.014623058	0.577160361	Ree spikes	13.60642547	0.606721469	
634	LLK12_186	LLK12_186-012	13.947081603161700	0.239244955	0.82541297	0.015553107	0.518876497	Ree spikes	12.68085463	0.234869942	
637	LLK12_186	LLK12_186-014	18.761665771618700	0.802521751	0.86415	0.019957535	0.704085449	Ree spikes	17.05833256	0.739328785	
638	LLK12_186	LLK12_186-015	24.929571053190700	0.958602224	0.96938861	0.021506639	0.280022959	P spike	22.66626635	0.885838444	x
639	LLK12_186	LLK12_186-016	15.758053180292500	0.664260578	0.82915825	0.020015534	0.514961041	Zr spike	14.3274118	0.61219052	
641	LLK12_186	LLK12_186-018	14.772583533029500	0.361612015	0.82066145	0.017230784	0.461275154	Zr inc	13.43141093	0.341907916	x
642	LLK12_186	LLK12_186-019	16.007067052607800	0.50363313	0.86948066	0.017684691	0.592416649	Ree spike	14.55381821	0.46905987	
643	LLK12_186	LLK12_186-020	18.104495464460400	0.870359057	0.8527263	0.018894809	0.759701903	Ree spike	16.4608254	0.799651746	
644	LLK12_186	LLK12_186-021	14.114263655710900	0.349784696	0.83436266	0.017171798	0.166654871	Ree drop	12.83285856	0.330421516	
645	LLK12_186	LLK12_186-022	25.545535951362700	0.590570428	1.012104462829100	0.027421957	0.512098244	Fe spike	23.22630906	0.560931667	
646	LLK12_186	LLK12_186-023	16.079385463869300	0.688819682	0.84513453	0.018348202	0.339194538	Zr inc	14.61957099	0.634555294	
647	LLK12_186	LLK12_186-024	17.731063269760400	0.732209753	0.86864238	0.01204221	0.532285526	Ree spike	16.12129635	0.675192014	x
648	LLK12_186	LLK12_186-025	14.431438631526600	0.514798933	0.83101666	0.019806911	0.367425631	P spike	13.12123787	0.476951763	
649	LLK12_186	LLK12_186-026	29.584374296122200	0.949558248	0.91224405	0.023822901	0.527311175	Ree spike	26.89846954	0.883561018	
650	LLK12_186	LLK12_186-027	24.374866461948600	0.655196706	0.89505573	0.01879325	0.53238365	Na spike	22.16192225	0.615500755	
651	LLK12_186	LLK12_186-028	12.218543790230000	0.436633536	0.81343496	0.013407463	0.492586058		11.10924722	0.404506527	
652	LLK12_186	LLK12_186-029	21.334683494663800	0.918452353	0.89866582	0.020418216	0.564275191	Ree spike	19.39775127	0.845990596	x
653	LLK12_186	LLK12_186-030	19.586956691929300	0.79216207	0.88417879	0.016159734	0.521919974	Y spike	17.808697	0.730908267	
654	LLK12_186	LLK12_186-031	17.644628294383900	0.966535345	0.83708602	0.017731919	0.457867409	Y spike	16.04270862	0.885902557	
656	LLK12_186	LLK12_186-033	21.822349064431400	0.848731543	0.88216764	0.013530355	0.603947725		19.84114268	0.784025465	
657	LLK12_186	LLK12_186-035	15.183650783601300	0.52395862	0.84614779	0.011760759	0.353946542		13.80515822	0.486052585	
658	LLK12_186	LLK12_186-036	16.273694701721800	0.634408345	0.84094875	0.016334	0.437990955	Zr spike	14.79623929	0.585999301	
659	LLK12_186	LLK12_186-037	15.129401161453300	0.53294096	0.83049845	0.012766691	0.58627521	Ree spike	13.75583381	0.493992591	
660	LLK12_186	LLK12_186-038	10.705115761629800	0.60459395	0.78582031	0.015644629	0.47753718	Na spike	9.733220224	0.553893106	
661	LLK12_186	LLK12_186-039	13.563834894250000	0.691796261	0.81423866	0.011603777	0.622368832		12.3324021	0.634861785	
662	LLK12_186	LLK12_186-040	7.943340025730070	0.365698144	0.7737786	0.012795565	0.225798858	Ree spike	7.222180451	0.33630298	
663	LLK12_186	LLK12_186-041	16.838502754824100	0.675352148	0.85687517	0.018373937	0.258105175	Zr spike	15.30976957	0.623282377	
664	LLK12_186	LLK12_186-043	19.116210089458300	0.777050963	0.8743511	0.019723953	0.385189143	Ree spike	17.38068852	0.716860902	
671	LLK12_186	LLK12_186-044	12.098334447456100	0.383111111	0.80592171	0.014620425	0.292370719	Zircon	10.99995144	0.356704144	
672	LLK12_186	LLK12_186-045	9.346044470761150	0.328534122	0.79126688	0.019442134	0.47205333	Ree spike	8.497536232	0.304548259	x
673	LLK12_186	LLK12_186-046	18.276545429973900	0.858800823	0.87401349	0.021008147	0.479393586	Ree spike	16.6172553	0.789413474	
674	LLK12_186	LLK12_186-047	13.737964003689700	1.607319069222030	0.8210016	0.022854448	0.788367806	ree spike	12.49072238	1.463996414	

Matthew Robert Barnett  
Constraining the hidden Delamerian margin

675	LLK12_186	LLK12_186-048	21.315319467086900	0.660297719	0.91034416	0.021130261	0.209935438	ree spike	19.38014526	0.615426024	
676	LLK12_186	LLK12_186-049	15.518442124441300	1.601478229940950	0.848537	0.022426212	0.686065252	Zr inc	14.10955454	1.45941543	
677	LLK12_186	LLK12_186-050	21.781074134593000	0.515443288	0.8941189	0.024824555	0.612182721	P spike	19.80361502	0.488639197	
678	LLK12_186	LLK12_186-051	14.156551983682800	0.347794732	0.83765242	0.014916144	0.350593984	Ree spike	12.87130762	0.328753802	x
679	LLK12_186	LLK12_186-052	21.373529659879900	1.118202583582270	0.86960857	0.022463284	0.445174785	Ree spike	19.43307067	1.025706291	
680	LLK12_186	LLK12_186-053	23.471476441359900	0.806197612	0.89054147	0.01701472	0.528161233	Ree spike	21.34054916	0.748010405	
681	LLK12_186	LLK12_186-054	13.873727667604500	0.725221618	0.84597105	0.018609777	0.695821149	ree spike	12.61416034	0.665242056	
682	LLK12_186	LLK12_186-055	15.779997934470600	0.410161302	0.84435562	0.016919811	0.460507724	Na spike	14.34736424	0.386156788	x
683	LLK12_186	LLK12_186-056	12.198334536812500	0.655867835	0.81253821	0.01706606	0.311573165	Ree spike	11.09087272	0.601334888	
684	LLK12_186	LLK12_186-057	12.374170999479600	0.456141546	0.8173007	0.013982263	0.410157429	P spike	11.25074535	0.422110611	
685	LLK12_186	LLK12_186-058	16.096655119462500	0.5217161	0.87695706	0.017194203	0.296286142	P spike	14.63527276	0.485242935	
686	LLK12_186	LLK12_186-059	22.609785335659600	0.637469676	0.90392372	0.025794301	0.686320935	Zr spike	20.55708923	0.597120187	
687	LLK12_186	LLK12_186-060	19.751859023085800	0.701061554	0.86883497	0.020446291	0.353951326	Ree spike	17.95862819	0.649641662	
749	LLK14_361	LLK14_361-001	13.534149354162400	1.160694340645090	0.80082797	0.022538927	0.665955643	Zr ree spikes	12.30541165	1.058812452	
750	LLK14_361	LLK14_361-003	24.122728889946000	0.401785816	0.88316433	0.013720268	0.639410755		21.93267573	0.396137012	
757	LLK14_361	LLK14_361-004	13.569136487004200	0.541823106	0.80330199	0.014691266	0.194812641		12.33722237	0.500113872	
758	LLK14_361	LLK14_361-005	13.622066821707600	0.577787078	0.81248165	0.011970782	0.46583977	Zr Ree spikes	12.38534727	0.53240792	
759	LLK14_361	LLK14_361-006	15.276955940385600	0.277470314	0.81384649	0.013733937	0.495780763	Ree spikes	13.8899924	0.270295567	
760	LLK14_361	LLK14_361-007	23.025152028456400	0.424933414	0.89131887	0.015959557	0.349980391	Ree spike	20.93474563	0.413105975	
761	LLK14_361	LLK14_361-008	14.570887525963200	0.631194092	0.81698994	0.014924401	0.485244288	Ree spikes	13.24802649	0.581303333	
762	LLK14_361	LLK14_361-009	17.634153813916800	0.528881207	0.83487066	0.015821289	0.333782618	P spike	16.0331851	0.493736412	
764	LLK14_361	LLK14_361-011	21.850969552881900	0.559046606	0.86685882	0.022552434	0.48594129	Ree spike	19.86716477	0.526898199	
765	LLK14_361	LLK14_361-012	18.082389002307500	1.060835887002580	0.84022977	0.020571385	0.541235713	Zr inc	16.44072593	0.97133835	x
766	LLK14_361	LLK14_361-013	17.652733938398400	1.112841344949300	0.81173886	0.01845376	0.441832645	P spike	16.05007837	1.018001841	
767	LLK14_361	LLK14_361-014	20.687859553288900	0.643453224	0.85220085	0.018519164	0.671989764	Ree spike	18.80965115	0.599609512	
768	LLK14_361	LLK14_361-015	24.038823587758500	1.036144579137930	0.88412256	0.0188769	0.541604803	Ree spike	21.85638802	0.954367211	x
769	LLK14_361	LLK14_361-016	18.886024583039000	0.419279457	0.8569015	0.010869448	0.31311703		17.17140109	0.39964071	
770	LLK14_361	LLK14_361-017	9.157705486036340	0.66689178	0.77660326	0.010021863	0.69473897		8.326296158	0.609129377	
771	LLK14_361	LLK14_361-018	17.089936806820900	0.417762382	0.83475412	0.015562472	0.528615199	Ree spike	15.53837644	0.395039652	
772	LLK14_361	LLK14_361-019	23.599220028558200	0.646488093	0.87406413	0.019040157	0.392509197	Ree spike	21.45669517	0.606604564	
774	LLK14_361	LLK14_361-021	17.702669899569500	0.661381412	0.84374983	0.015044573	0.598435664	Ree spike	16.09548075	0.611757246	
775	LLK14_361	LLK14_361-022	21.299927877221100	0.395414443	0.85196885	0.0115486	0.395940115		19.36615104	0.384126656	

Matthew Robert Barnett  
Constraining the hidden Delamerian margin

776	LLK14_361	LLK14_361-024	22.655698963886100	0.62973713	0.87993825	0.026402819	0.730425909	La Spike	20.59883445	0.590369436
777	LLK14_361	LLK14_361-025	16.685048573651300	0.328594155	0.82272447	0.014207284	0.419986214	Ree spike	15.17024718	0.316999913
778	LLK14_361	LLK14_361-026	26.068329359522800	0.896498727	0.87734449	0.021787797	0.471871894	Ree spike	23.70163912	0.83175337
779	LLK14_361	LLK14_361-027	17.667187488219500	0.50661169	0.82476238	0.020804486	0.440570448	Ree spike	16.06321972	0.474088406
780	LLK14_361	LLK14_361-028	15.811289732398400	0.894888561	0.82555115	0.011683706	0.58967836		14.37581512	0.819817428
781	LLK14_361	LLK14_361-029	21.579535987519200	0.519625882	0.85830845	0.02225625	0.436864827	Ree spikes	19.62037411	0.491929471
782	LLK14_361	LLK14_361-030	23.525051188871100	0.69698307	0.87586264	0.017475024	0.656447184	Ree spikes	21.38925997	0.651082145
783	LLK14_361	LLK14_361-031	21.418372656613400	0.681016988	0.85246124	0.017366171	0.385386397	ree spikes	19.47384246	0.633956452
786	LLK14_361	LLK14_361-032	20.565168985563300	0.454965196	0.86340496	0.018050418	0.275717461	Ree spikes	18.69809941	0.433791891
787	LLK14_361	LLK14_361-033	14.628093398899400	0.320362983	0.81326925	0.010699182	0.261895961	Zr inc	13.30003876	0.305736578
788	LLK14_361	LLK14_361-034	26.047711110623100	0.881876791	0.89998939	0.015420137	0.451165349	Ree spikes	23.68289276	0.818702796
789	LLK14_361	LLK14_361-035	23.075700654468200	0.953641748	0.85398469	0.021984311	0.298734145	Zr inc	20.98070505	0.879362374
790	LLK14_361	LLK14_361-036	14.907771151469200	0.576966716	0.80908837	0.012375719	0.231144928	Ree spike	13.55432514	0.53306172
791	LLK14_361	LLK14_361-037	22.969796376927100	0.548230004	0.85580522	0.015383647	0.380079532	Ree spike	20.8844156	0.51936854
792	LLK14_361	LLK14_361-038	20.444251272186400	0.579620259	0.85884082	0.011237436	0.554953022		18.58815957	0.542759159
793	LLK14_361	LLK14_361-040	18.479541295367700	0.439247975	0.82755685	0.011780472	0.433608436	Ree spike	16.80182158	0.416259493
794	LLK14_361	LLK14_361-041	2.075777440941850	0.047418826	0.72387888	0.0051582	-0.115162684	Zr inc	1.887321858	0.045084555
795	LLK14_361	LLK14_361-042	13.399671468817700	0.460240618	0.78999571	0.015407402	0.521580466	Ree spike	12.18314274	0.427023214
796	LLK14_361	LLK14_361-043	20.559326425346700	0.858196112	0.83875463	0.020211051	0.517610778	Ree spike	18.69278728	0.791133131
801	LLK14_361	LLK14_361-044	21.726161953554700	0.626516268	0.87564343	0.020065007	0.310958661	Ree spike	19.7536882	0.586111744
802	LLK14_361	LLK14_361-045	14.105532467444200	0.437202975	0.82547241	0.015102153	0.478417307	Ree spike	12.82492006	0.407480928
803	LLK14_361	LLK14_361-046	22.330173226231000	0.699027849	0.87186734	0.026876236	0.337313461	Zr inc	20.30286253	0.651196904
804	LLK14_361	LLK14_361-047	17.152103217433800	0.588930117	0.83241135	0.017505942	0.435875121	Zr inc	15.59489889	0.546431897
805	LLK14_361	LLK14_361-048	19.094039132685300	0.405857557	0.83946101	0.015615318	0.239644762	Zr inc	17.36053042	0.388427789
806	LLK14_361	LLK14_361-049	17.724305572838400	0.399616366	0.83925408	0.013019529	0.173360367	Ree spike	16.11515217	0.380376111
807	LLK14_361	LLK14_361-050	18.208499238283500	1.027470011220140	0.8341678	0.02406382	0.525095846	Ree spike	16.55538688	0.941319401
808	LLK14_361	LLK14_361-051	24.493909577062100	0.623056011	0.87885911	0.024180907	0.427935173	Zr inc	22.27015769	0.587463316
809	LLK14_361	LLK14_361-052	21.775726478397000	0.496097647	0.85865761	0.013493743	0.194680683	Ree spike	19.79875286	0.47178587
810	LLK14_361	LLK14_361-053	21.473412213448000	0.478474865	0.86337055	0.018393949	0.43760835	Ree spike	19.52388509	0.455913075
811	LLK14_361	LLK14_361-054	20.316175806206200	0.602628807	0.8540636	0.01091906	0.330154414		18.47171181	0.562906527
812	LLK14_361	LLK14_361-055	20.715737336397600	0.434872577	0.85445337	0.014389844	0.341553048	Ree spike	18.83499797	0.416708567
813	LLK14_361	LLK14_361-056	25.547270901720700	0.771225895	0.87437718	0.022982623	0.449290327	Ree spike	23.22788649	0.719736805
814	LLK14_361	LLK14_361-057	24.542953292245300	0.57530721	0.89406923	0.018337154	0.36310068	Ree spike	22.31474882	0.545809461



815	LLK14_361	LLK14_361-058	23.138631378966000	0.428660215	0.87235235	0.015429795	0.195786336	Zr inc	21.03792242	0.416530484
816	LLK14_361	LLK14_361-059	21.662938122208800	0.801592566	0.86348542	0.014950607	0.514316485	Ree spike	19.69620433	0.741691381
688	LLK14_379	LLK14_379-001	14.976140198689100	0.451768089	0.81266343	0.012454871	0.43652662	Ree spike	13.6164871	0.421622722
689	LLK14_379	LLK14_379-002	15.920548698081800	0.775743734	0.81902442	0.016282545	0.499226286		14.47515468	0.712527064
690	LLK14_379	LLK14_379-003	14.306070952004300	0.42651601	0.82067658	0.009532477	0.329116184		13.00725207	0.398296341
691	LLK14_379	LLK14_379-004	14.436943855676300	0.284855037	0.8094324	0.017696437	0.547855672	Zr spike	13.12624329	0.274746482
692	LLK14_379	LLK14_379-005	18.841454727316200	0.30647621	0.84999834	0.015656961	0.585210876	Ree spike	17.13087764	0.303261705
693	LLK14_379	LLK14_379-006	8.025064561381060	0.216513751	0.77398562	0.018257927	0.668329366	Zr inc	7.296485384	0.203348523
694	LLK14_379	LLK14_379-007	16.333008017149300	0.305351146	0.83693037	0.014993694	0.364363304	Ree spike	14.85016767	0.296376921
695	LLK14_379	LLK14_379-008	17.420584139790200	0.8176655	0.83120145	0.014825361	0.450275007	Ree spike	15.83900498	0.751619889
696	LLK14_379	LLK14_379-009	13.762677298974300	0.350381603	0.80036566	0.011849532	0.448251625	Zr spike	12.51319201	0.330346015
699	LLK14_379	LLK14_379-011	16.168584363942400	0.408968893	0.8231191	0.011487483	0.497879173		14.7006717	0.385759567
700	LLK14_379	LLK14_379-012	16.518588542382100	0.679825032	0.82869958	0.01216209	0.445259605	Ree spike	15.01889972	0.626946023
701	LLK14_379	LLK14_379-013	19.751911713802800	1.228139697011630	0.87352037	0.025713287	0.425261709	Ree spike	17.9586761	1.123664465
702	LLK14_379	LLK14_379-014	18.530090674061100	0.411411045	0.84629856	0.022594709	0.543592204	Ree spike	16.84778169	0.392137972
703	LLK14_379	LLK14_379-016	10.822354604656200	0.398622185	0.7986261	0.01345576	0.159390464	Ree spike	9.839815192	0.368892676
704	LLK14_379	LLK14_379-017	15.199363346017300	0.483091343	0.82123733	0.013540299	0.157405682	Zr spike	13.81944427	0.449716122
705	LLK14_379	LLK14_379-018	11.111436616761500	0.33952192	0.79710858	0.012539021	0.318010887	Zr inc	10.10265204	0.316661752
706	LLK14_379	LLK14_379-019	16.202327836301900	0.387012131	0.82096969	0.015863958	0.56668698	Ree spike	14.73135167	0.36661522
707	LLK14_379	LLK14_379-020	15.920080249773100	0.521074759	0.82082412	0.013962517	0.327467364	Ree spike	14.47472877	0.484437599
708	LLK14_379	LLK14_379-022	16.270165135961900	0.432322241	0.83310097	0.01091509	0.492096586		14.79303016	0.406429403
709	LLK14_379	LLK14_379-023	12.039394778680600	0.283778922	0.79093613	0.013862748	0.245177679	Zr inc	10.94636278	0.269107876
714	LLK14_379	LLK14_379-024	20.201592181884000	0.834236167	0.86085522	0.016808078	0.535089581	Ree spike	18.367531	0.769273421
715	LLK14_379	LLK14_379-025	13.715556173537500	0.724488592	0.80955149	0.017749165	0.485205975	Zr inc	12.47034892	0.664449002
717	LLK14_379	LLK14_379-027	11.382858383327900	0.517736528	0.78892066	0.009372816	0.292072771		10.34943198	0.476251773
718	LLK14_379	LLK14_379-028	18.960878151971700	0.743280577	0.84568149	0.01676897	0.590598219	Ree spikes	17.23945885	0.686445985
719	LLK14_379	LLK14_379-029	13.564035428868200	0.241104563	0.80734396	0.012059102	0.47031144	Ree spikes	12.33258443	0.235536012
720	LLK14_379	LLK14_379-030	20.100864980157400	1.026559554438890	0.85789069	0.01991711	0.656952545	Zr Ree spikes	18.27594861	0.942051347
721	LLK14_379	LLK14_379-031	17.363297061612200	0.345018642	0.83830915	0.017507928	0.243539927	Zr spike	15.78691888	0.332515503
722	LLK14_379	LLK14_379-032	16.884232225405900	1.294219799308000	0.84374671	0.022431638	0.670141869	Ree P spike	15.35134736	1.18159663
723	LLK14_379	LLK14_379-033	17.671360638739600	0.349636484	0.82644966	0.020883367	0.394520567	Zr Ree spikes	16.06701399	0.337125696
724	LLK14_379	LLK14_379-034	15.880174262716000	0.578203301	0.82934588	0.013698395	0.333527594	Zr spike	14.43844576	0.535297469

725	LLK14_379	LLK14_379-035	12.339398266261400	0.431966262	0.80116768	0.013359899	0.465494428	P spike	11.21912957	0.400492143
728	LLK14_379	LLK14_379-036	20.184495429606700	0.643261941	0.86255967	0.013263362	0.632407022	Ree spikes	18.35198642	0.598747154
729	LLK14_379	LLK14_379-037	16.161845346249500	0.479257016	0.83282159	0.011740043	0.509626168	Ree spike	14.6945445	0.447673853
730	LLK14_379	LLK14_379-038	16.074921257447800	0.467698384	0.81829379	0.01523937	0.411367139	P spike Zr Ree	14.61551208	0.437322024
731	LLK14_379	LLK14_379-040	14.132515262144100	0.647866719	0.80548456	0.01569494	0.528727021	spikes	12.84945314	0.59584804
732	LLK14_379	LLK14_379-041	11.703465388786900	0.194561131	0.79860882	0.011090442	0.210835298	Ree spikes	10.64093173	0.191880459
733	LLK14_379	LLK14_379-042	20.250454213610900	0.645169448	0.85753378	0.018803322	0.648475582	Ree spikes	18.41195695	0.60053096
734	LLK14_379	LLK14_379-043	20.248177759307200	0.901809795	0.86232844	0.015468471	0.580409033	Zr inc	18.40988717	0.829960619
735	LLK14_379	LLK14_379-044	12.849589133594200	0.531397597	0.80494419	0.011458054	0.363903799	Ree spikes	11.68300125	0.489997521
736	LLK14_379	LLK14_379-045	11.683450085726100	0.667792125	0.78524991	0.013125272	0.399006328	Ree spike Zr Ree	10.62273358	0.611682492
737	LLK14_379	LLK14_379-048	17.123612182687500	0.431206158	0.82437697	0.017868382	0.548139871	spikes	15.5689945	0.406863408
738	LLK14_379	LLK14_379-050	15.335601617123100	0.959718449	0.82806477	0.022640483	0.59933425	Ree spike	13.94331375	0.878007018
739	LLK14_379	LLK14_379-051	19.521164028985600	0.796780735	0.84408004	0.023073257	0.247354449	Zr inc	17.74887752	0.734976078
740	LLK14_379	LLK14_379-052	12.804244310405900	0.862479699	0.80231329	0.01582928	0.710129545	Zr inc	11.64177319	0.788382642
741	LLK14_379	LLK14_379-053	13.667829357511800	0.645568861	0.79820064	0.016253789	0.331200163	Ree spike	12.42695512	0.59334374
742	LLK14_379	LLK14_379-054	16.918563162642500	0.50570038	0.8290317	0.01089278	0.385065505	Ree spike	15.38256146	0.472178688
743	LLK14_379	LLK14_379-055	18.340862901250200	1.001831742233110	0.85331052	0.017942023	0.207711456	P spike	16.67573352	0.918296109
744	LLK14_379	LLK14_379-056	12.008918602113400	0.398797732	0.79435926	0.013906281	0.494953923	Zr inc	10.91865347	0.370527158
745	LLK14_379	LLK14_379-057	19.503698759204500	0.852271923	0.84828497	0.019592861	0.390365328	Ree spike	17.73299789	0.784734893
746	LLK14_379	LLK14_379-058	15.016836784484200	0.592908777	0.8427005	0.019702959	0.402785452	Ree spike	13.65348892	0.547452259
747	LLK14_379	LLK14_379-059	15.782675067058100	0.65388468	0.82216724	0.018609931	0.441400755	Ree spike	14.34979832	0.602911512
748	LLK14_379	LLK14_379-060	18.416222714912500	0.364621377	0.85045975	0.014637107	0.430602105	Ree spike	16.74425157	0.35154796
393	MP02556_b	MP02556_b-002	1.884311923255930	0.17195688	0.71315144	0.075861997	0.379278364	Rb low	1.702323374	0.156242287
394	MP02556_b	MP02556_b-003	7.463028287474070	0.513912436	0.76494964	0.026795195	0.301548856	zr spike	6.74224227	0.46895617
395	MP02556_b	MP02556_b-004	7.614413213805570	0.267497248	0.7542477	0.013314817	0.181447728		6.879006303	0.250888475
396	MP02556_b	MP02556_b-005	2.231621096319730	0.202532087	0.71624666	0.01852509	0.354077682	Zr spike	2.016089114	0.184034948
397	MP02556_b	MP02556_b-008	0.274698785	0.012593924	0.70807758	0.011801514	0.229162767	Fe spike	0.248168128	0.01163461
398	MP02556_b	MP02556_b-009	2.997055686027080	0.191975254	0.72477984	0.011388534	-0.127232154	Zr spike	2.707597339	0.175452077
399	MP02556_b	MP02556_b-010	6.979809814022870	0.197082794	0.75912431	0.017158501	0.10753105	Zr drop	6.305693473	0.188466813
400	MP02556_b	MP02556_b-012	0.216470544	0.015545784	0.726127	0.007780539	0.101130815	Zr spike	0.195563623	0.014174514
401	MP02556_b	MP02556_b-013	0.417578498	0.021105581	0.71850469	0.009079703	0.072813266	Zr spike	0.377248389	0.019422279
402	MP02556_b	MP02556_b-014	7.211375783430220	0.228419031	0.77386073	0.01592181	0.426696469	Ree spike	6.514894592	0.216008718

403	MP02556_b	MP02556_b-016	0.35501408	0.019460463	0.71959163	0.008350089	0.165087023	Ree spike	0.320726499	0.017859693
404	MP02556_b	MP02556_b-017	0.557528003	0.021453363	0.7173047	0.006955673	0.067754475		0.503681445	0.020000035
407	MP02556_b	MP02556_b-020	0.55743568	0.054363782	0.70998404	0.020056492	-0.148463431	Ree spike	0.503598038	0.049360609
408	MP02556_b	MP02556_b-022	0.818473987	0.049439817	0.7171958	0.009728871	0.106330074	Zr spike	0.739425029	0.045248847
409	MP02556_b	MP02556_b-023	2.006560274140080	0.048884259	0.72389381	0.011109832	0.465539575	Y spike	1.812764869	0.047602
414	MP02556_b	MP02556_b-024	0.779491433	0.071053609	0.71900308	0.009629529	-0.07040081	Y spike	0.704207446	0.06456108
415	MP02556_b	MP02556_b-026	0.487147119	0.02582551	0.71494888	0.011519085	-0.098830631	Zr spike	0.44009801	0.023726531
416	MP02556_b	MP02556_b-027	1.139192302853800	0.039091277	0.71849162	0.007723148	0.113381056		1.029168081	0.036727717
417	MP02556_b	MP02556_b-028	1.170574773121830	0.074843122	0.72192416	0.015477039	-0.052279546	Zr spike	1.057519603	0.068404305
418	MP02556_b	MP02556_b-030	5.460749622050930	0.274546277	0.76456	0.012614949	0.174438515	Zr spike	4.933345488	0.252698128
419	MP02556_b	MP02556_b-031	0.504100123	0.031298844	0.71738114	0.011310758	0.144898285	Zr spike	0.455413678	0.02862601
420	MP02556_b	MP02556_b-034	6.411234816582910	0.287328359	0.76158836	0.013703751	-0.038970348	Zr spike	5.792031963	0.265711209
422	MP02556_b	MP02556_b-036	3.797674088071120	0.31002488	0.72243476	0.010829389	0.270966645	Mg spike	3.430891292	0.282093209
423	MP02556_b	MP02556_b-038	1.441486869704960	0.069898274	0.73432028	0.017786693	0.023978	La spike	1.302266765	0.064424097
424	MP02556_b	MP02556_b-039	1.128429470995990	0.115202034	0.71982478	0.014389626	-0.0193671	Mg spike	1.019444733	0.104554105
364	MP02556_w	MP02556_w-001	1.704114473277280	0.077097016	0.72325819	0.008762702	-0.146170957	Zr inc	1.539529557	0.071266175
367	MP02556_w	MP02556_w-002	3.471952741711780	0.198896486	0.73186306	0.012772003	-0.120754582	Zr spike	3.136628408	0.182297039
368	MP02556_w	MP02556_w-003	1.002688898491540	0.018794454	0.71868808	0.009069847	0.368227326	Zr spike	0.905848298	0.019159806
369	MP02556_w	MP02556_w-004	3.245432390340770	0.878202309	0.72269065	0.021285309	0.395438048	3 Zr peaks	2.931985597	0.793904849
370	MP02556_w	MP02556_w-005	6.905905752494450	0.145398525	0.75931656	0.008466953	0.212591213		6.238927133	0.144887658
371	MP02556_w	MP02556_w-007	3.083190310959240	0.392115125	0.7266137	0.011071582	0.065114055	Zr increasing	2.785413004	0.355294396
372	MP02556_w	MP02556_w-008	8.997605729642450	0.813847444	0.76891374	0.015207822	0.315757536	Zr drop	8.128608835	0.739547921
373	MP02556_w	MP02556_w-009	1.367283433441150	0.127782388	0.71439336	0.010102642	0.124307962		1.235229964	0.116073965
374	MP02556_w	MP02556_w-011	5.033127062514770	0.20597565	0.74123741	0.009872052	0.194771448		4.547023101	0.191343145
375	MP02556_w	MP02556_w-015	3.139445663713590	0.141709012	0.7232969	0.009513016	0.196694146	Y spike	2.836235164	0.131005041
376	MP02556_w	MP02556_w-019	3.746311302617120	0.233272666	0.73378488	0.013184089	0.258415572	Zr spike	3.384489171	0.21333697
377	MP02556_w	MP02556_w-020	6.372082040494570	0.150354669	0.74073699	0.016417273	-0.122880274	Mg spike	5.756660597	0.147082279
378	MP02556_w	MP02556_w-022	11.127187144037900	0.437265167	0.77167567	0.0151722	0.460111367	Zr spike	10.05251335	0.407131737
379	MP02556_w	MP02556_w-023	4.073222844246640	0.114447238	0.73831015	0.018192908	0.09189416	Mg spike	3.6798273	0.109502074
384	MP02556_w	MP02556_w-025	0.951262544	0.081700004	0.71034622	0.013283949	0.211266368	Mg spike	0.859388748	0.074288261
385	MP02556_w	MP02556_w-026	9.525452116306030	0.750111393	0.76006879	0.017395626	0.09010869	Mg spike	8.605475341	0.682892076
388	MP02556_w	MP02556_w-028	2.885722000191490	0.062919305	0.72786062	0.022285955	0.47400062	Ree spikes	2.607016361	0.062319941

389	MP02556_w	MP02556_w-029	6.262447224043890	0.481302224	0.75203704	0.017625715	0.052209181	Mg spike	5.65761441	0.438338121
390	MP02556_w	MP02556_w-030	1.208982972472530	0.080258071	0.73490643	0.013487406	0.161757533	Zr drop	1.092218304	0.073292441
391	MP02556_w	MP02556_w-035	8.944654124658380	0.409890786	0.77454	0.015834147	-0.099505535	K spikes	8.080771344	0.378675862
392	MP02556_w	MP02556_w-038	2.901049075854870	0.135191034	0.73162237	0.018582635	0.195935169	Mg spike	2.620863134	0.124805491
425	MP02628	MP02628-001	0.081222347	0.004231057	0.71388827	0.005869916	0.317011329	Mg spike	0.073377819	0.003889467
426	MP02628	MP02628-002	0.147595825	0.005492118	0.71693874	0.005347669	0.059643977	Mg spike	0.133340887	0.005130866
427	MP02628	MP02628-003	1.699620090423890	0.054107305	0.72737815	0.005336262	0.048560409	Y spike	1.535469246	0.051145151
430	MP02628	MP02628-005	0.273371157	0.017251232	0.71951419	0.005594031	0.084549712	Zr spike	0.246968723	0.015771894
431	MP02628	MP02628-007	0.438279004	0.034443441	0.717039	0.006575042	-0.008379588	La Spike	0.395949621	0.031357856
432	MP02628	MP02628-008	0.67537424	0.016204437	0.72451688	0.009557675	0.171089444	Zr spike	0.610145985	0.015813403
433	MP02628	MP02628-009	0.568137348	0.025197807	0.72240909	0.004793772	-0.007328846		0.51326613	0.023313249
434	MP02628	MP02628-010	0.587076949	0.021456534	0.72240771	0.009816348	0.104912642		0.530376526	0.020068967
435	MP02628	MP02628-011	0.244189112	0.017695438	0.71317675	0.007897022	-0.004655766	Zr spike	0.220605106	0.016131912
436	MP02628	MP02628-012	0.446222699	0.007839375	0.7198003	0.007848881	0.07742421	La spike	0.403126107	0.008109553
437	MP02628	MP02628-013	0.133231722	0.00647398	0.71566649	0.004920477	0.052373185		0.120364082	0.005966473
438	MP02628	MP02628-014	0.282604378	0.012339098	0.71990269	0.004819212	-0.103296142		0.255310192	0.011424705
439	MP02628	MP02628-016	0.461528338	0.018140205	0.71889822	0.006971953	0.052363331	Zr spike	0.416953514	0.01688991
440	MP02628	MP02628-017	1.101685790742010	0.047143208	0.70533484	0.020716036	0.377926613	La spike	0.995283981	0.043692628
441	MP02628	MP02628-018	0.153606414	0.007467081	0.71748437	0.005986684	0.003579052	La spike	0.138770967	0.006881613
442	MP02628	MP02628-019	0.281462423	0.022537044	0.72411847	0.009381727	-0.071874288	Ree spike	0.254278527	0.020512316
443	MP02628	MP02628-020	0.204163479	0.010476903	0.71573758	0.004632113	0.050366276		0.184445185	0.009636077
444	MP02628	MP02628-021	0.407569124	0.017995331	0.71955809	0.004801032	0.073439705		0.36820573	0.016652947
445	MP02628	MP02628-022	0.512273938	0.020027994	0.71816016	0.005008307	0.118860872		0.462798058	0.018653417
446	MP02628	MP02628-023	0.460771166	0.01307172	0.71548466	0.005566571	0.226382295	Mg spike	0.41626947	0.012493965
451	MP02628	MP02628-024	1.086469587810010	0.056916088	0.72062585	0.006022385	-0.223318225	K spikes	0.981537373	0.052311026
452	MP02628	MP02628-025	0.600956296	0.030345614	0.7198546	0.005559233	0.077198581		0.542915394	0.027926308
453	MP02628	MP02628-026	0.870740913	0.019448605	0.72100957	0.005442399	-0.118350527		0.786643969	0.019186992
454	MP02628	MP02628-027	0.474889063	0.007009396	0.71526474	0.004828868	0.18241582		0.429023848	0.007601047
455	MP02628	MP02628-028	1.633273291717300	0.104049541	0.73350435	0.011082391	-0.015446154	La spike	1.475530281	0.095105997
456	MP02628	MP02628-029	0.159072461	0.00679868	0.72077114	0.007331425	0.27838582	Ree spike	0.143709099	0.006301445
459	MP02628	MP02628-031	0.285554737	0.012375652	0.71532204	0.004910914	0.076757094		0.257975602	0.011462662
460	MP02628	MP02628-032	0.802409391	0.037396008	0.72005105	0.005748074	-0.064958285	La spike	0.724911967	0.034523077
461	MP02628	MP02628-033	0.173260627	0.012231655	0.71565699	0.006753808	-0.243154379	Zr spike	0.156526959	0.011156267

462	MP02628	MP02628-034	0.484389965	0.063886915	0.71140052	0.01393312	0.132124205	Mg spike	0.437607145	0.057875758
463	MP02628	MP02628-035	0.414780313	0.036135863	0.71841437	0.007315334	-0.044374041	Mg spike	0.374720455	0.032851711
464	MP02628	MP02628-036	0.465892236	0.023091185	0.71602323	0.006450054	0.078983636	Mg spike	0.420895943	0.021264877
465	MP02628	MP02628-037	0.109881402	0.004195975	0.71816762	0.005861128	-0.00088669	Mg spike	0.099268957	0.003913559
466	MP02628	MP02628-038	0.454257734	0.020389289	0.71932785	0.009783489	0.138435832	Ree spike	0.410385112	0.018853989
467	MP02628	MP02628-039	0.246475206	0.016595043	0.71327949	0.007419413	0.083441014	Mg spike	0.222670408	0.015150249
468	MP02628	MP02628-040	0.569099089	0.03768516	0.71793164	0.006713886	-0.013016003		0.514134985	0.034416289
469	MP02628	MP02628-041	0.486412874	0.066964116	0.71520102	0.008518014	0.115109359	Zr spike	0.439434679	0.060649737
470	MP02628	MP02628-043	0.895346186	0.030172209	0.71556132	0.005792215	0.050852454	Ree spike	0.808872842	0.028387322
471	MP02628	MP02628-044	0.403435542	0.014508188	0.71854604	0.008608968	0.124131817	Ree spike	0.364471373	0.013584918
472	MP02628	MP02628-045	0.32771948	0.023584679	0.72027214	0.006114195	0.014808098	Ree spike	0.296068036	0.021503486
473	MP02628	MP02628-046	0.391577986	0.022245992	0.71151645	0.007577547	0.075958074	Zr spike	0.35375903	0.020394264
474	MP02628	MP02628-049	1.915331690693530	0.063125622	0.72491678	0.00610348	-0.069336058		1.730347225	0.059496496
475	MP02628	MP02628-050	2.523364580465110	0.062080836	0.72509381	0.013005383	0.014513299	Mg spike	2.279655748	0.060370574
476	MP02628	MP02628-052	4.399100641994370	0.110336998	0.74051098	0.007758717	0.319831677		3.974231526	0.107018869
478	MP02628	MP02628-058	0.154801062	0.006882362	0.71171468	0.005762882	0.14628781	Ree spike	0.139850235	0.006366909
479	MP02628	MP02628-059	1.947909726079450	0.036976752	0.72300151	0.005701982	-0.116313173	Ree spike	1.759778844	0.037594294
482	MP02628	MP02628-060	4.353649935716370	0.142795033	0.72786846	0.011456959	0.234258152	Zr spike	3.93317049	0.134638831
483	MP03_493mic	MP03_493mic-001	0.314684758	0.02126716	0.71525477	0.023524856	0.11313429		0.284292219	0.019414098
484	MP03_493mic	MP03_493mic-002	0.35691409	0.045060521	0.72303952	0.024323691	0.044676819		0.322443004	0.040830987
485	MP03_493mic	MP03_493mic-003	0.246207604	0.019202639	0.70196334	0.021605815	0.255185258		0.222428651	0.017484435
490	MP03_493mic	MP03_493mic-004	0.290805168	0.019086727	0.70724197	0.023922217	0.192283423		0.262718942	0.017434458
491	MP03_493mic	MP03_493mic-005	0.300117178	0.018878723	0.71628979	0.020766109	-0.008473129		0.271131589	0.017261123
492	MP03_493mic	MP03_493mic-006	0.204359115	0.021372934	0.70399231	0.017836955	0.373723274		0.184621927	0.019393296
493	MP03_493mic	MP03_493mic-007	0.261406198	0.016503904	0.71579638	0.02030222	0.101236614		0.236159351	0.015088485
494	MP03_493mic	MP03_493mic-009	1.334317015615630	0.142651356	0.76262187	0.048971135	0.175600721	P spike	1.205447472	0.129414243
495	MP03_493mic	MP03_493mic-010	0.123506143	0.017872019	0.7118732	0.014215283	0.103902366	Ree spike	0.111577808	0.016182906
496	MP03_493mic	MP03_493mic-011	1.653807750277510	0.11702247	0.68499401	0.040792238	0.501032362		1.494081503	0.106729405
497	MP03_493mic	MP03_493mic-012	7.231550532804740	0.462205922	0.74499155	0.043429479	0.473332623		6.533120846	0.422445276
498	MP03_493mic	MP03_493mic-013	12.772881755872000	1.125920888583980	0.84482682	0.083064588	0.360166536	P spike	11.53926529	1.023444901
499	MP03_493mic	MP03_493mic-014	3.364216081791110	0.146747776	0.70023825	0.030756489	0.21168101		3.039297052	0.135879244
500	MP03_493mic	MP03_493mic-015	31.111524788954100	2.704419667310430	0.83205792	0.081464671	0.37669674		28.1067456	2.458701269
501	MP03_493mic	MP03_493mic-016	10.453041244702100	0.998349953	0.70886815	0.066135933	0.510400293	Zr spike	9.443477073	0.906663769



502	MP03_493mic	MP03_493mic-017	13.631393670471800	0.945769592	0.78111328	0.060536199	0.511718624		12.31486135	0.862907054
503	MP03_493mic	MP03_493mic-018	18.176660953502600	1.181671973857110	0.82252256	0.069827991	0.539052679		16.42114261	1.079605759
504	MP03_493mic	MP03_493mic-019	12.162438421922300	1.443428353265670	0.79640126	0.096334334	0.461981874	P spike	10.98777913	1.308458832
505	MP03_493mic	MP03_493mic-020	8.301537474546450	0.513536048	0.74145452	0.040119531	0.36103235		7.499767481	0.469723699
506	MP03_493mic	MP03_493mic-021	0.180193415	0.009273382	0.71674114	0.005189797	0.074936337		0.162790172	0.008528288
507	MP03_493mic	MP03_493mic-022	0.282532535	0.065134961	0.7127554	0.01006187	0.296202475		0.255245287	0.058897307
508	MP03_493mic	MP03_493mic-023	1.149075653695400	0.04515903	0.72366193	0.020566426	0.268835756		1.038096888	0.042046761
509	MP03_493mic	MP03_493mic-024	0.120254573	0.009965822	0.71450836	0.005558233	-0.212915758		0.108640278	0.009066043
510	MP03_493mic	MP03_493mic-025	0.751504507	0.028851501	0.71407114	0.021223087	0.313992562		0.678923523	0.026900746
513	MP03_493mic	MP03_493mic-026	3.183624741557170	0.503638062	0.73574052	0.027715146	0.335983363		2.876147386	0.455868406
514	MP03_493mic	MP03_493mic-027	2.748242724873800	0.202659868	0.70707528	0.038649239	0.166949663		2.482814958	0.184696425
515	MP03_493mic	MP03_493mic-028	2.284926327496200	0.111300431	0.72864157	0.029810433	0.300353371	P spike	2.064246077	0.10256562
516	MP03_493mic	MP03_493mic-029	9.643754006297370	0.73303811	0.75144844	0.03751181	0.455149149		8.712351527	0.667721641
517	MP03_493mic	MP03_493mic-030	57.569965104203600	3.920727589330860	1.006702398022580	0.098365128	0.637382989	P spike	52.00980584	3.578542558
518	MP03_493mic	MP03_493mic-031	66.228211966520900	4.715867757658020	1.103208699769150	0.083755425	0.767481772		59.83183139	4.300562908
519	MP03_493mic	MP03_493mic-032	0.808103729	0.0733181	0.71873874	0.011602682	-0.07294888		0.73005634	0.066622229
520	MP03_493mic	MP03_493mic-033	19.403989675334100	0.701689864	0.8207011	0.028987999	0.512625682		17.52993481	0.656784603
521	MP03_493mic	MP03_493mic-034	12.041218504406400	0.579424436	0.79443825	0.013917326	0.319863047		10.87826674	0.5342079
522	MP03_493mic	MP03_493mic-035	34.965260481436800	0.854327268	0.92471718	0.027325937	0.669475976	Ree spike	31.58828402	0.831579746
523	MP03_493mic	MP03_493mic-036	3.952598082157540	0.140400108	0.71457824	0.030570044	0.254368576	Ree spike	3.570852587	0.131578729
524	MP03_493mic	MP03_493mic-037	68.741713733903500	1.598667213466700	1.136098965156880	0.025486698	0.688587605		62.10257689	1.567254517
525	MP03_493mic	MP03_493mic-038	9.293142192010520	0.880714028	0.74130465	0.024924907	0.108745441	P spike	8.395602119	0.799896379
526	MP03_493mic	MP03_493mic-039	57.963600769782000	2.826786254959850	1.085793880626550	0.033477329	0.711220177		52.36542381	2.604821697
527	MP03_493mic	MP03_493mic-040	13.605177590757300	1.042568196903720	0.81209881	0.075194137	0.064317227	Mg spike	12.29117724	0.949546592
528	MP03_493mic	MP03_493mic-041	5.913113856709920	0.362817805	0.74246276	0.023796291	0.307488052		5.342019976	0.331930751
529	MP03_493mic	MP03_493mic-042	7.786569620236700	0.140252271	0.76563258	0.015829469	0.309481398	Zr spike	7.034535688	0.144245691
530	MP03_493mic	MP03_493mic-043	4.568898879133490	0.338214599	0.7381496	0.024457027	0.347666565		4.127630496	0.308215337
535	MP03_493mic	MP03_493mic-044	1.308261799483180	0.076939889	0.71915738	0.007286916	0.16857446		1.181908692	0.070467356
536	MP03_493mic	MP03_493mic-045	0.544365332	0.020092243	0.70947317	0.010371382	-0.144766421		0.491790036	0.018780617
537	MP03_493mic	MP03_493mic-046	0.234873403	0.020325587	0.7137566	0.011961144	0.019126046	P spike	0.212189117	0.018479885
538	MP03_493mic	MP03_493mic-047	0.178330586	0.008386879	0.70231445	0.010227282	0.043151923	P spike	0.161107257	0.007739609
539	MP03_493mic	MP03_493mic-048	4.917145288433680	0.166189084	0.74601971	0.02108065	0.599425069	Rb spike	4.442242952	0.156322249
540	MP03_493mic	MP03_493mic-050	6.742808006365490	0.184251791	0.75543709	0.012291188	0.212409493		6.091581514	0.176837215

544	MP03_493mic	MP03_493mic-052		0.263655559	0.009813806	0.71577529	0.009800012	0.119907336		0.238191467	0.009168106
545	MP03_493mic	MP03_493mic-053		0.14204194	0.004998316	0.71991442	0.008814077	-0.047295403	P drop	0.128323401	0.004687409
546	MP03_493mic	MP03_493mic-054	1.390140059910350		0.127374358	0.71874971	0.014441269	0.256961915	Rb drop	1.255879076	0.115728705
547	MP03_493mic	MP03_493mic-055		0.151648137	0.005885536	0.70947307	0.009372486	0.047578324		0.137001822	0.00548399
548	MP03_493mic	MP03_493mic-056		0.349971807	0.010334327	0.72070685	0.008589809	0.108460063		0.316171213	0.009836931
549	MP03_493mic	MP03_493mic-057		0.321368733	0.026581083	0.71955298	0.011850523	0.033438589	Ree spike	0.29033065	0.024181818
550	MP03_493mic	MP03_493mic-058		0.344220451	0.023459919	0.71494523	0.011933452	-0.042966507	P spike	0.310975329	0.021412114
551	MP03_493mic	MP03_493mic-059		0.320699666	0.014924273	0.71226117	0.015201232	0.273922133	Rb spike	0.289726203	0.013778577
552	MP03_493mic	MP03_493mic-060		0.29974239	0.011685196	0.72305763	0.009968206	0.313590264	P spike	0.270792999	0.010885061
553	MP03_548mic	MP03_548mic-001		0.287760382	0.010056472	0.70978624	0.014645375	0.192813498	P spike	0.259968224	0.009435645
554	MP03_548mic	MP03_548mic-002		0.190267089	0.009429214	0.71714581	0.0080665	0.10916541		0.171890921	0.008683483
555	MP03_548mic	MP03_548mic-003	3.683575576569360		0.092093719	0.73222916	0.005964715	0.008726961	P spike	3.327812518	0.089362378
556	MP03_548mic	MP03_548mic-004		0.707665232	0.039845352	0.69274951	0.014621909	0.16869841	Mg spike	0.639318284	0.036538198
557	MP03_548mic	MP03_548mic-005	2.516172091240620		0.094881037	0.7255331	0.005698094	0.191118542		2.273157916	0.08856466
558	MP03_548mic	MP03_548mic-006		0.156448362	0.008531856	0.70938956	0.008712002	0.098179043	Rb drop	0.141338438	0.007831301
559	MP03_548mic	MP03_548mic-007	3.146478959983100		0.126660334	0.72808637	0.013572891	0.19281038	P spike	2.842589178	0.117769327
560	MP03_548mic	MP03_548mic-008		0.201058088	0.018242995	0.715297	0.011991388	0.09170748	P spike	0.181639717	0.016576916
561	MP03_548mic	MP03_548mic-009		0.136322243	0.004150851	0.71380179	0.007734361	0.197589944		0.123156117	0.003939389
562	MP03_548mic	MP03_548mic-010	73.744297888817600	9.057540256548820	1.167667577092510	0.072485242		0.923378916	Ree spike	66.62200694	8.208759172
563	MP03_548mic	MP03_548mic-011	3.230088074743360		0.470817338	0.70005024	0.044011278	0.49773663	P spike	2.918123249	0.426305604
564	MP03_548mic	MP03_548mic-012	177.185854675196000	5.957397156451810	1.824746935089180	0.054807015		0.839868466		160.0730847	5.605974482
565	MP03_548mic	MP03_548mic-013	147.106171207396000	2.659408233570760	1.708298461188590	0.040236931		0.762919997		132.8985242	2.732849633
566	MP03_548mic	MP03_548mic-014	146.221697196942000	3.451604534123110	1.645693220657020	0.04826595		0.58579113	Ree spike	132.0994735	3.376283646
567	MP03_548mic	MP03_548mic-015	140.636780835856000	2.840706792032950	1.647597677338690	0.04135384		0.728684981	Ree spike	127.0539534	2.852439425
568	MP03_548mic	MP03_548mic-016	196.796915963295000	3.985111491238960	2.003028909609350	0.049275699		0.788497251		177.7900919	3.999653281
569	MP03_548mic	MP03_548mic-017	93.016323962222800	3.404598710173820	1.280090357314210	0.057313316		0.674644716	Ree spike	84.03272332	3.184112185
570	MP03_548mic	MP03_548mic-018	61.394046682128600	1.881395348130620	1.079399991830630	0.041730542		0.452251346	Ree spike	55.46455416	1.784481716
571	MP03_548mic	MP03_548mic-019	70.620783673871100	3.146796002886870	1.114835093782870	0.043066613		0.582449238	Zr spike	63.80016455	2.910815755
572	MP03_548mic	MP03_548mic-021	20.217117285394900		0.477540088	0.84930481	0.025769771	0.160612715	Zr spike	18.26452982	0.467074744
575	MP03_548mic	MP03_548mic-022	77.167447657201000	2.283222335136420	1.144356598423430	0.045621892		0.550390448	Na spike	69.71454581	2.172901316
576	MP03_548mic	MP03_548mic-023	86.969427283701900	3.109865582517020	1.180368230961400	0.057194845		0.730494663	Ree spike	78.56984138	2.91310874
581	MP03_548mic	MP03_548mic-024	129.875442787789000	3.322705460549760	1.504990958492140	0.046950888		0.606198459	Ree spike	117.3319551	3.214478172

Matthew Robert Barnett  
Constraining the hidden Delamerian margin

582	MP03_548mic	MP03_548mic-025	438.934997286863000	37.898609858801200	3.466369876677160	0.26133405	0.974639933		396.5422585	34.45815128
583	MP03_548mic	MP03_548mic-026	21.795298833958600	0.866707773	0.85079381	0.012811488	0.340950061		19.69028917	0.806426089
584	MP03_548mic	MP03_548mic-027	19.744854425152800	0.446690592	0.82889071	0.014723796	0.365321382		17.83787854	0.439782909
585	MP03_548mic	MP03_548mic-028	17.478599807871400	0.650934047	0.81066615	0.018579699	0.256162145	Rb peak	15.79050084	0.608084919
586	MP03_548mic	MP03_548mic-029	65.780589103869100	1.821433917210650	1.109824960503650	0.025754154	0.590345171	P peak	59.42744035	1.745534086
587	MP03_548mic	MP03_548mic-030	59.920209285142300	3.380758987594810	1.082748738825220	0.040144472	0.694723792	P peak	54.13306131	3.099970226
588	MP03_548mic	MP03_548mic-031	93.442050126822600	2.369237919343920	1.285454715859880	0.031470739	0.682696163		84.41733246	2.29472182
589	MP03_548mic	MP03_548mic-032	6.888119007915510	0.735715247	0.75539369	0.00820836	0.722391125		6.222858248	0.667450906
590	MP03_548mic	MP03_548mic-033	68.738980812331900	1.515785582001060	1.153552167854040	0.02234369	0.646355094		62.10010791	1.498525798
591	MP03_548mic	MP03_548mic-034	33.479517339927400	2.937459440980180	0.9033972	0.039768685	0.739349837	Ree spike	30.24603529	2.670258592
592	MP03_548mic	MP03_548mic-035	33.533420817379300	0.831218041	0.90219772	0.026146676	0.439772295	Zr spike	30.29473272	0.807493882
593	MP03_548mic	MP03_548mic-036	1.132864258928080	0.036406675	0.71751942	0.005556936	-0.000191172	P spike	1.023451205	0.034385697
594	MP03_548mic	MP03_548mic-037	68.868198822787600	1.760590282806250	1.144812507298320	0.033194464	0.739294987	Ree spike	62.21684593	1.703407584
595	MP03_548mic	MP03_548mic-038	17.379323269988400	0.250393824	0.81859138	0.009427975	0.296206473		15.70081252	0.273578751
596	MP03_548mic	MP03_548mic-039	18.611531743367900	0.60411346	0.84309189	0.016157354	0.523529401	Ree spike	16.81401318	0.570098644
597	MP03_548mic	MP03_548mic-040	52.110442258994400	1.693744706561510	1.043473959848040	0.025918109	0.611168264	P spike	47.07756864	1.598197655
598	MP03_548mic	MP03_548mic-041	86.678886851769800	4.418989026747900	1.268432666051020	0.059558042	0.691966713		78.30736161	4.065285243
599	MP03_548mic	MP03_548mic-042	114.829778501455000	4.061801403252990	1.460140582523910	0.051983974	0.733013828		103.7394147	3.807730512
600	MP03_548mic	MP03_548mic-043	136.035004803786000	4.577917760101210	1.648091732426430	0.048484668	0.814168172		122.8966211	4.307567115
601	MP03_548mic	MP03_548mic-044	104.069495876328000	2.967921719851210	1.429115279899080	0.040867716	0.679100239		94.0183699	2.835162086
602	MP03_548mic	MP03_548mic-045	66.458034739422500	2.911335151392050	1.131510426591810	0.026784929	0.803098764		60.03945767	2.695162371
603	MP03_548mic	MP03_548mic-046	103.804269954978000	3.668718935043670	1.417251351313900	0.044780862	0.711008738	Ree drops	93.77875973	3.439442029
604	MP03_548mic	MP03_548mic-047	144.982334421800000	3.621179498408740	1.654802947804480	0.046395887	0.709576414	Ree spike	130.9798095	3.514240441
607	MP03_548mic	MP03_548mic-048	205.314002408856000	8.256988978149910	2.102789722656110	0.077007691	0.838643596	Na spike	185.4845905	7.67779267
608	MP03_548mic	MP03_548mic-049	162.756156405256000	3.227446697066380	1.793531622244890	0.036025574	0.683073754		147.0370197	3.252351083
609	MP03_548mic	MP03_548mic-050	157.782076708090000	3.970684404293040	1.771188304274500	0.042474745	0.637643249	P spike	142.5433411	3.849577146
610	MP03_548mic	MP03_548mic-051	12.899865352115000	0.392642318	0.80203595	0.020124237	0.37898057	P spike	11.6539847	0.372652261
611	MP03_548mic	MP03_548mic-052	9.947848185176520	0.327355152	0.77713284	0.005895596	0.423901143		8.987076016	0.308574146
612	MP03_548mic	MP03_548mic-053	44.608654509456200	1.129242487052000	0.99436828	0.020775843	0.600505755	Ree drops	40.30031033	1.093954991
613	MP03_548mic	MP03_548mic-054	242.855881787532000	5.782424153415060	2.325081965567430	0.058523273	0.796302013		219.4006412	5.649113253
614	MP03_548mic	MP03_548mic-055	177.898556604853000	5.888111209865350	1.845630911694000	0.068469322	0.737025121	Ree spike	160.7169532	5.547696447
615	MP03_548mic	MP03_548mic-056	266.122533902005000	19.745398711972700	2.301464584544030	0.158742545	0.94333284	Ree spike	240.420179	17.99328916
616	MP03_548mic	MP03_548mic-057	214.482965087693000	6.690025573459470	2.051357860176700	0.06023568	0.797740996		193.7680064	6.335173462

617	MP03_548mic	MP03_548mic-058	149.266463286876000	6.250157537904780	1.682680940062380	0.054823862	0.796953614	Ree spike	134.8501733	5.799090359
618	MP03_548mic	MP03_548mic-059	145.745594752145000	2.947627496212430	1.643535396486430	0.034419368	0.656102997		131.6693535	2.959088787
619	MP03_548mic	MP03_548mic-060	179.383371540893000	6.791836800295290	1.857279987814690	0.0729959	0.695573345	Zr spike	162.0583634	6.338069215

## APPENDIX 16: SOLUTION ICP-MS METHOD

Samples were pulverised using a tungsten carbide ring mill. Sample contamination was prevented with a quartz wash between each sample crush. Samples were prepared first by dissolving all mineral phases in bombs with 28 molar hydrofluoric acid and a dilution using 7 molar nitric acid. The solution was then placed in 15 ml Teflon vials, using 7 molar nitric acid, 6 molar hydrochloric acid and 28 molar hydrofluoric acid. Each sample was then diluted using 2% HNO<sub>3</sub> into two vials for analysis. A 1:1000 dilution was used for analysis of REE and a 1:100000 for major elements. These were analysed at Adelaide Microscopy using the solution ICP-MS Agilent 8900x QQQ-ICP-MS. Standards were prepped alongside international standard USGS G-2 (granite powder) (Flanagan, 1976). Adelaide Microscopy prepared BHVO-1 (basalt powder) standard (Flanagan, 1976) was also included in the run. Due to the use of HF in the dissolution phase of samples, silica concentrations were not able to be obtained for analysis.

## APPENDIX 17: METHOD FOR WHOLE-ROCK DIGESTION USED IN TIMS PREPARATION

Using hydrochloric acid, nitric acid and hydrofluoric acid. Samples were spiked with .4gm <sup>150</sup>Nd/<sup>147</sup>Sm solution and dissolution was carried out in high-pressure Teflon vessels, in a hydrofluoric (4mL of 28M) and nitric (2mL of 15M) mixture, over a several day period at 190°C. This ensured all mineral phases were in solution. Samples were evaporated until dry, 6mL of 6M HCL were added and these were placed back into the ‘bombs’ overnight.

Samples were dried down at 140°C. 1.5mL of 2M HCL were added and sample and then centrifuged. Using column chromatography following Foden et al. (1995), isotope ratios were measured using the Isotopx Phoenix Thermal Ionisation Mass Spectrometer. The international Nd standard JNdi-1 yielded <sup>143</sup>Nd/<sup>144</sup>Nd values of  $0.512107 \pm 0.000003$  (2 s.d.) within uncertainty of published values ( $0.512115 \pm 0.000007$ ) (Tanaka et al., 2000). Blanks showed negligible Nd and Sm.